POLITECNICO DI TORINO

Master's Degree in Electrical Engineering

Master's Degree Thesis

High-speed IPM motors for traction application

Supervisors

Prof. Gianmario PELLEGRINO

Prof. Simone FERRARI

Candidate

Roberto ACQUAVIVA

November 2023

Abstract

Wrapped interior permanent magnet (IPM) synchronous motors represent a recent breakthrough in the domain of high-speed IPM machines. This innovative rotor design, pioneered by Tesla, Inc. in the Model S Plaid electric vehicle, introduces buried permanent magnets (PMs) and a carbon-fiber (CF) sleeve to secure the magnets against centrifugal forces, obviating the need for traditional iron bridges typical in conventional IPM rotor configurations. Inspired by surface-mounted PM (SPM) rotors, this wrapping technique has the potential to transcend existing speed limitations, as Tesla attests to achieving speeds surpassing 20,000 RPM with this cutting-edge motor. Nevertheless, the design and analysis of retaining sleeves are essential for enabling safe and efficient high-speed operation.

This thesis embarks on a multifaceted exploration. Firstly, it delves into a comprehensive analysis of the advantages associated with employing high-speed electric motors in powertrains, endeavoring to substantiate the pursuit of elevated rotational speeds. Following an overview of conventional technologies, the thesis scrutinizes the benefits of the wrapped rotor design, unveiling its practical advantages. Secondly, the thesis meticulously formalizes and parametrizes the rotor design. Employing an analytical model for the retaining sleeve, already validated in the literature through finite element analysis (FEA), the thesis introduces a pre-design tool for forecasting the dimensions and characteristics requisite for the carbon sleeve to facilitate motor operation at specific speeds. A comparative analysis is then conducted with the Model 3 IPM motor, which employs iron ribs for rotor retention, to investigate disparities in performance and efficiency. Finally, an attempt is made to establish a scaling law for sleeves and ribs.

The fruits of this research effort are envisioned to be seamlessly integrated into the open-source motor design and simulation tool, SyR-e. Within this thesis, SyR-e serves as an essential platform for executing comparative performance analysis between the wrapped IPM motor and traditional designs, offering invaluable insights into the real-world potential of this high-speed motor in various applications. This work has the the aim of helping the continuous evolution of advanced electric motor technology, particularly within the sphere of high-speed traction applications.

Table of Contents

List of Tables

List of Figures

Acronyms

2D

Two-Dimensional

AC

Alternating Current

BC

Boundary Condition

CAD

Computer-Aided Design

CF

Carbon-Fiber

DC

Direct Current

DENERG

Dipartimento Energia

D.IMEAS

Distretto del Dipartimento di Ingegneria Meccanica e Aerospaziale

FE

Finite Element

FEA

Finite Element Analysis

FEMM
Finite Element Method Magnetics

GUI
Graphical User Interface

IPM
Interior Permanent Magnet

MMM
Magnetic Model Manipulation

MODE
Multi-Objective Differential Evolution

NdFeB
Neodymium Iron Boron

PDE
Partial Differential Equation

PM
Permanent Magnet

pp
pole piece

p.u.
per unit

SmCo
Samarium Cobalt

SPM
Surface Permanent Magnet

SyR
Synchronous Reluctance

SyR-e
Synchronous Reluctance-evolution

Chapter 1

Introduction

The electric automotive industry has witnessed a remarkable growth trajectory in recent years, driven by the increasing demand for efficient and sustainable energy solutions. In the last decade, several pioneers of the engine vehicles manufacturing industry invested a huge amount of resources in the electric or hybrid powertrain development, producing new car models to compete in the e-Mobility market.

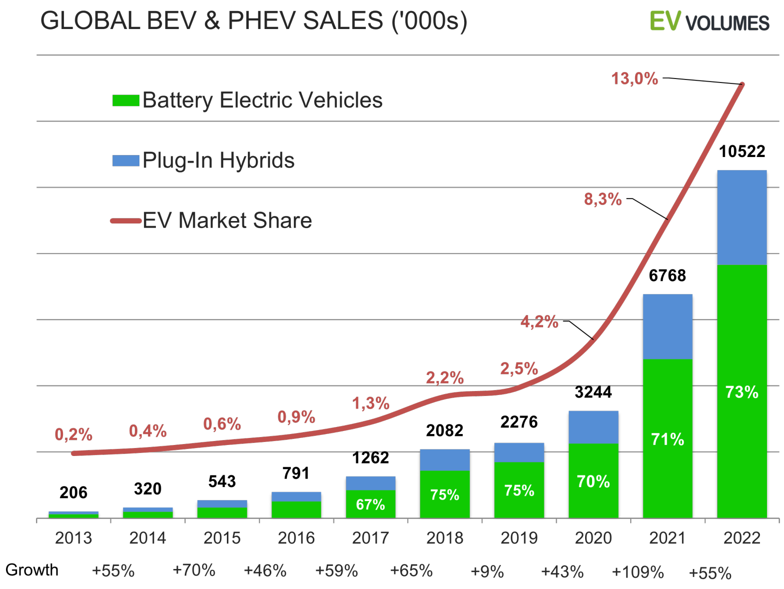

Figure 1.1: Global *BHEVs* and *PHEVs* sales 2021-2022 [1]

Other companies have made the electric axle their strong point several years earlier. Among these, *Tesla, Inc.* stands out as one of the carriers of the transition to sustainable energy, a mission that the company has been pursuing since 2003.

At the end of 2022, *Tesla*'s annual production counts more than 1.3 million cars, covering the 17% of the electric car's market.

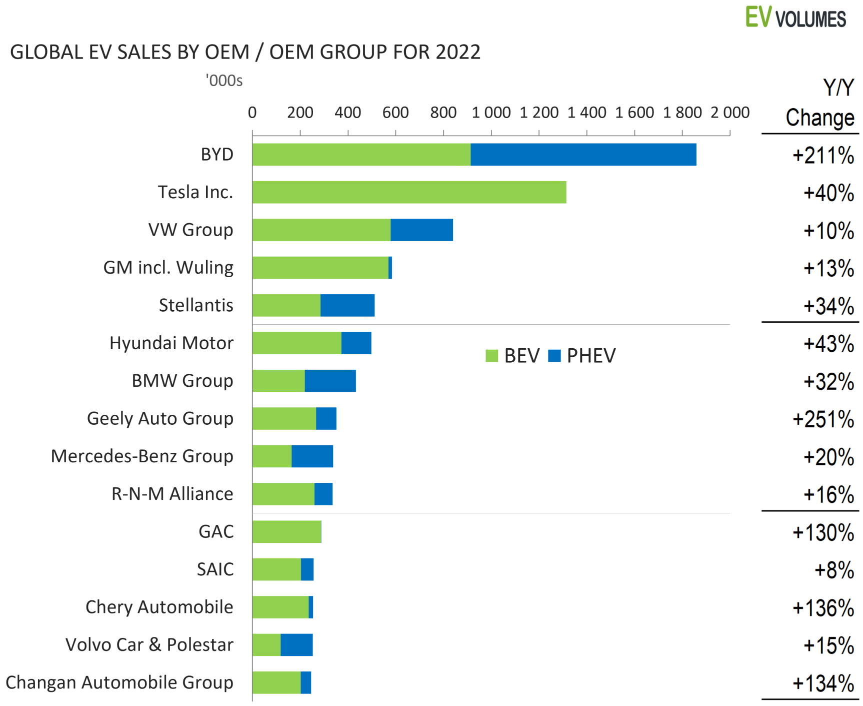

Figure 1.2: Electric cars production by brand (*BHEVs* and *PHEVs*) - Top 15 [1]

The american company leads the competition to the green mobility thanks to its advanced technology in the car components design. In 2021, *Tesla* launched a new version of its five-passenger electric luxury sedan, the Tesla Model S Plaid, capable of the quickest acceleration of any vehicle in production.

Figure 1.3: Tesla Model S Plaid

This high-performance car has a 0-60 mph (0-96.6 km/h) acceleration time of

1.99 seconds, an electric range (EPA est.) of 396 miles (637,3 km) and a power of 1020 hp (761 kW), reaching the top speed of 200 mph (322 km/h). The amazing capabilities of the Model S Plaid powertrain can be attributed to its Tri-motor configuration, one for the front axle and two in the rear for the rear wheels with torque vectoring system.

The three identical electric motors are PM V-Type synchronous motors with carbon wrapped rotor. The carbon sleeve is a retaining feature that allows the rotor to reach high speed. Indeed, increasing the speed of an electrical machine is by far the most effective way of improving its power density without compromising its efficiency. High-speed electric motors must withstand mechanical stresses and optimize energy conversion to meet the demands of modern electric vehicles.

The primary objective of this research is to unravel the problematics of high-speed electric motor designs, with a specific focus on the technological innovations introduced by Tesla in its motors. By digging in the design philosophies and structural considerations of the IPM V-Shape motors utilized in the Tesla Model 3 and Model S Plaid, this research seeks to contribute in the understanding of the advanced motor technologies utilized in the automotive industry.

1.1 Problem Definition

Electric motors play a pivotal role in the automotive industry's transition towards sustainable and high-performance vehicles. However, optimizing their design for superior efficiency and performance remains a complex challenge. This thesis addresses the need for a comprehensive exploration of electric motor designs, focusing on two distinct technologies: sleeve and ribs motors.

The criticism to face will be finding a systematic approach to compare and optimize these motor designs for specific automotive applications. The traditional ribs motors, widely used, are contrasted with the innovative sleeve motors, known for their potential performance benefits. The primary challenge lies in developing a robust methodology to analyze, compare, and optimize these motors, considering critical factors such as power, torque, efficiency, and structural integrity.

In the investigation process, the thesis adopts a multifaceted approach, combining theoretical analyses, analytical modeling, and the multiple tools of the software SyR-e. The goal is to provide valuable insights into the performance disparities and design considerations between sleeve and ribs motors, ultimately contributing to the advancement in the understanding of the pros and cons of this two technologies.

1.2 Manuscript Content and Organization

The thesis initiates with an introduction in Chapter 1, defining the problem and outlining the manuscript's structure. In Chapter 2 it then delves into SyR-e design, covering background, design approaches, simulation, and software interactions. Following this, in Chapter 3 the high-speed motor design concepts are explored, particularly focusing on the wrapped rotor solution.

Chapter 4 proceeds to the sleeve design analytical model, covering conditions, equivalent rotor geometry and stress/displacement analysis, presenting system equations. Sub-sequentially, in Chapter 5 the creation of the new Sleeve Designer tool is thoroughly explained. Making use of the tool, in Chapter 6 the sleeve motor design is approached following a structured methodology, analyzing designs at different speeds. Simultaneously, in Chapter 7 the ribs motor design is investigated, conducting structural analyses and designing candidates at varying speeds.

The thesis reaches a climax in Chapter 8 with a comprehensive comparison between sleeve and ribs motors. It considers geometrical and system parameters, performance, efficiency, and scaling trends across different speeds.

Chapter 9 is conclusive section, which summarizes research outcomes, underscoring achievements and suggesting future development areas.

Chapter 2

***SyR-e* Design**

This chapter aims to give an overview of the capabilities of the software SyR-e, adopted for every study presented on this thesis. Moreover, as will be presented in Chapter 5, a small contribution to the extension of the code will come up as a result of this master thesis work. Therefore, it is essential to report the workflow of the tool that allows to perform the design and analyze electric motors.

2.1 Background

Figure 2.1: SyR-e: Synchronous Reluctance - evolution [2]

SyR-e stands for Synchronous Reluctance - evolution and is an open-source code developed in Matlab/Octave.

Born in 2009, from a collaboration between Politecnico di Torino and Politecnico di Bari, SyR-e development passed trough the contribution of many professors, researchers and students. With the purpose of providing an automatic designing tool for non-expert designers and investigate SyR rotor geometries, this non commercial software now allows to design several machine types, making use of finite element analysis and multi-objective optimization algorithms.

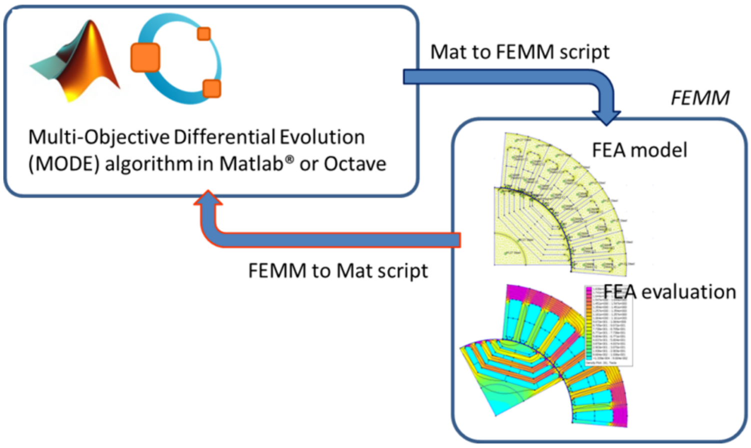

Figure 2.2: SyR-e workflow to evaluate machines performance [3]

Depicted in Figure 2.2, the data flow shows the operating principle of the design platform: a drawing of a machine, generated as a .fem file by a MATLAB script, is analyzed by FEMM. The result is then fed back to MATLAB for performance evaluation. The latest versions of SyR-e embed an open-source version of a MODE (Multi Objective Differential Evolution) algorithm, that guarantee really good performances in terms computational requirements and quality of the results compare to other similar algorithms. An additional noteworthy feature that enhances SyR-e's capabilities is its implementation of analysis procedures that minimize the reliance on FEA while still yielding valuable results.

As reported in the SyR-e user manual [3], the interface with Matlab opens the door to many capabilities if the following packages are installed:

- Simulink: dynamic model simulations (syreDrive)
- Simscape and Simscape Electrical: dynamic model simulations (syreDrive)
- Curve Fitting Toolbox: used for some post-processing
- Parallel Computing Toolbox: for the parallel computing of FEA simulations
- PDE Toolbox: structural analysis and mass computation

Particularly, the last two features above reported have been mainly used for the analysis that will be presented.

Other implemented capabilities, that were frequently used on this thesis work, for extracting essential parameters and maps or to interface with external software are:

- Export of the motor model to dxf file or other commercial FEA softwares.
- Link to the MMM GUI.

Although SyR-e is supported both in MATLAB and Octave, from this point on every application of the software will be referred to the MATLAB interface.

2.2 Design eMotors with *SyR-e*

The main interaction with SyR-e makes use of a GUI (Graphical User Interface), called from Matlab typing the command GUI_SyRe.m.

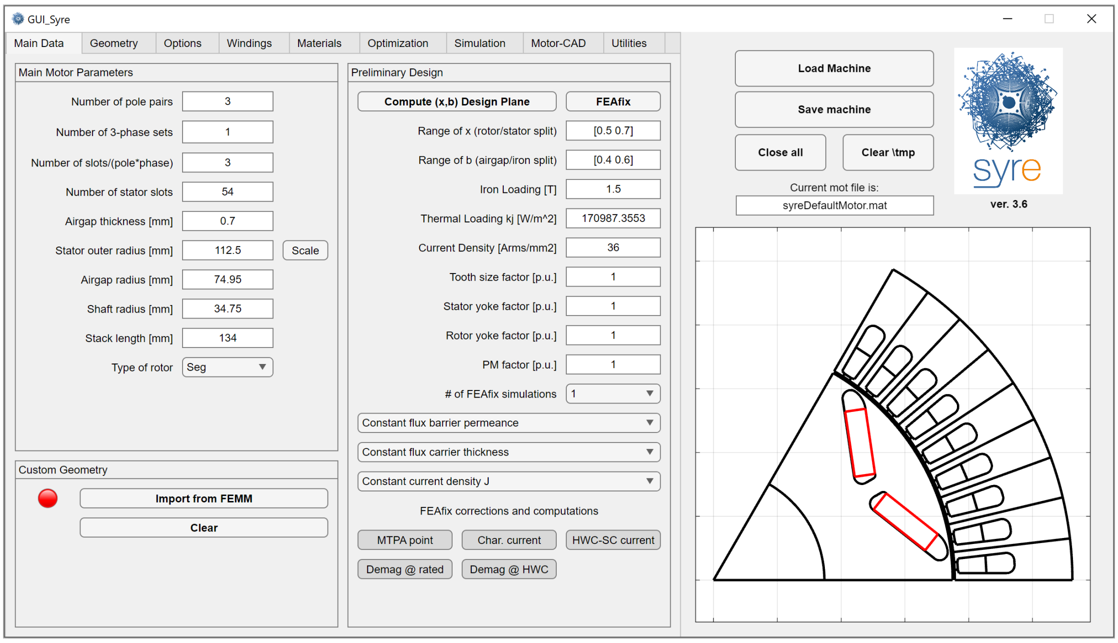

Main Motor Parameters	
Number of pole pairs	3
Number of 3-phase sets	1
Number of slots/(pole*phase)	3
Number of stator slots	54
Airgap thickness [mm]	0.7
Stator outer radius [mm]	112.5
Airgap radius [mm]	74.95
Shaft radius [mm]	34.75
Stack length [mm]	134
Type of rotor	Seg

Preliminary Design	
Range of x (rotor/stator split)	[0.5 0.7]
Range of b (airgap/iron split)	[0.4 0.6]
Iron Loading [T]	1.5
Thermal Loading kj [W/m^2]	170987.3553
Current Density [Arms/mm2]	36
Tooth size factor [p.u.]	1
Stator yoke factor [p.u.]	1
Rotor yoke factor [p.u.]	1
PM factor [p.u.]	1
# of FEAfix simulations	1

Constant flux barrier permeance
Constant flux carrier thickness
Constant current density J

Current mot file is: syreDefaultMotor.mat

Figure 2.3: SyR-e GUI main tab [2] with default geometry.

The Main Data tab, visible in Figure 2.4, is the starting point of interaction. A default machine is automatically loaded as a starting template. Other templates are available to be loaded in the motorExample folder in the SyR-e repo.

When a machine is saved in a folder, two types of essential file are created in order to use the functionalities of the app:

- .mat: a MATLAB file containing all the variables related to the machine parameters and more. This is the file that will be loaded in the SyR-e GUI.
- .fem: a FEMM file that allows to analyze, simulate and customize the geometry in the external software.

Trough FEMM, the geometry can be customized and imported to the SyR-e GUI, in order add features that the parametrization wouldn't allow to create.

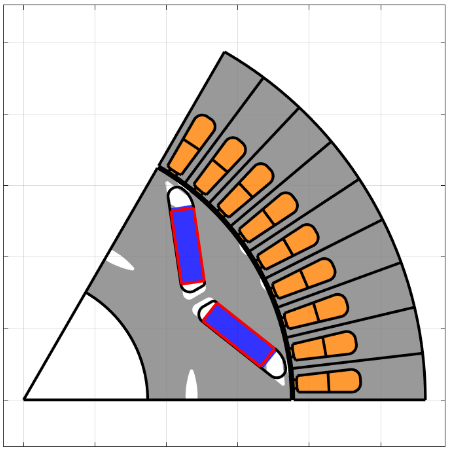

Figure 2.4: TeslaModel3 motor from the motorExamples with custom FEMM geometry.

2.2.1 Manual Design Approach

In the *Main Data* tab (Figure 2.4), the Main Motor Parameters section allows to change the number of poles and slots, the sizing parameters and the rotor geometry.

Several types of rotor configurations are available in the 'Type of rotor' drop down menu. Labeled in Figure 2.5: (a) Circular geometry, (b) Fluid geometry, (c) Seg geometry, (d) SPM rotor, (e) V-type IPM rotor, (f) induction machine.

The second tab is the *Geometry* tab, where the Stator Parameters and the Rotor Parameters can be modified. For the Stator, teeth and slots dimensions are the characteristic of interest of this manual design approach. For Rotor parameters, there are two different sections: the first allows to modify rotor barriers for synchronous machines, that may contain permanent magnets. The second second can be used for IM rotor designing.

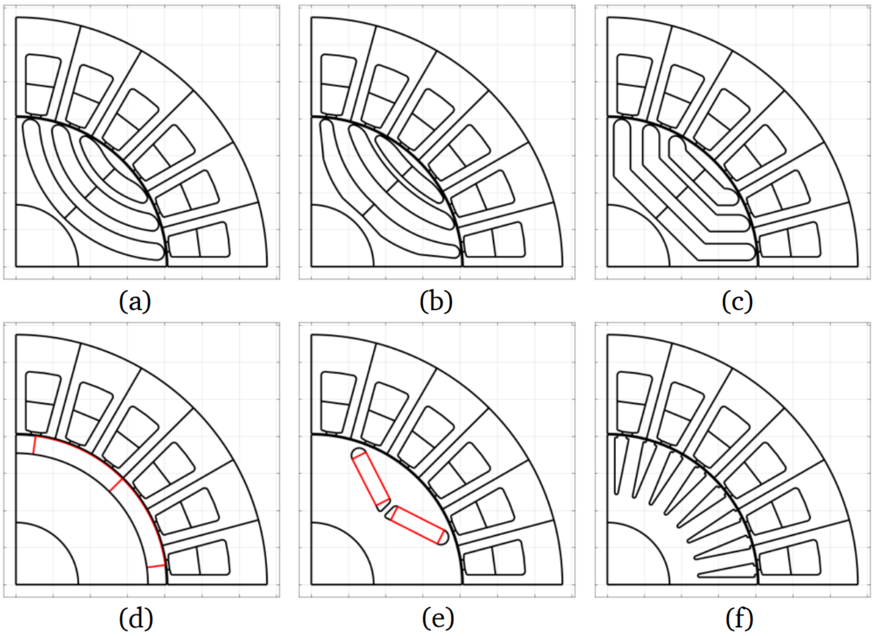

Figure 2.5: Available basic rotor geometries in SyR-e. PMs are colored red. The stators are taken from the mot_01 available in the motorExamples.

In the *Options* tab it is possible to define Thermal and Structural parameters (this is where a Sleeve Thickness can be defined). Moreover, in the Ribs Design section radial and tangential ribs can be customized if the rotor presents this features.

The *Windings* tab allows to assign the parameters related to the winding configuration, the conductors number and dimensions and finally it gives the possibility to draw and evaluate the slot model.

One last tab to assign motor parameters is the *Materials* tab. Every material of the machine is defined in there. The parameters related to the permanent magnets (if present) are also in this tab in a dedicated section.

2.2.2 Tools for Preliminary Design and Optimization

(x,b) Design Plane feature facilitate the initial design process using analytical equations originally developed for SyR machines. A design plane is constructed, illustrating torque and power factor in relation to the rotor-to-stator outer diameters ratio and the air gap-to-iron flux density ratio. Each point on the plane represents a motor, allowing users to select their desired design.

An enhancement to this preliminary design is provided by the `FEAfix` function, which refines the analytical equations through a few selected Finite Element Analysis (FEA) simulations. The latest version of SyR-e is capable of designing SyR, PM-assisted SyR, and IPM motors using this approach.

A third tool, named `PM Design`, facilitates the preliminary design of the permanent magnets used in V-type IPM and PM-assisted SyR machines.

Motor design optimization in SyR-e is made possible by the `MODE` algorithm, accessible in the Optimization tab. In addition to specifying parameters for the optimization process (e.g., the number of generations), users can choose from various optimization variables and set boundaries, such as the air gap length or various stator tooth dimensions. Optimization objectives may include torque T or power factor $\cos\phi$.

2.3 Simulation

In its primary graphical user interface (GUI), SyR-e provides various possibilities for finite element analysis (FEA) simulations. All electromagnetic FEA simulations are conducted using FEMM. The software receives the motor model and the user-controlled mesh size, available in the Options tab. FEMM then performs the simulation with a static magnetic solver, emulating rotor movement through multiple evaluations at different rotor positions. Users can choose the number of points and the total angular excursion. Typically, the electrical degrees of a pole are sufficient, leveraging symmetry in standard three-phase distributed winding motors.

Depending on the selected simulation type in the Simulation tab, parameters such as the per-unit (p. u.) current load, PM temperature θ_{PM}, or the rotor speed n (e.g., for structural FEA) must be set initially. The most relevant FEA evaluations available in SyR-e include:

- **Single Operating Point Simulation:** Evaluates a single (i_d, i_q) point, with resulting phase flux linkages, torque, and power factor plotted against rotor position (electrical degrees).
- **Flux Map:** Computes flux linkages λ_d, λ_q, and torque T over the dq current domain. The number of current quadrants can be 1, 2, or 4.
- **Iron Loss Evaluation:** Computes hysteresis and eddy-current losses of stator, rotor, and PMs for a given rotor speed, either for a single operating point or a flux map.
- **PM Motor Analysis:** Three selectable options: calculation of characteristic current, demagnetizing current, and demagnetized PM area (for a given demagnetizing current) as functions of θ_{PM}.

- **Short-Circuit Analysis:** Estimates peak short-circuit current in case of a three-phase symmetric short-circuit event.
- **Structural Analysis:** Uses the Partial Differential Equation (PDE) Toolbox of MATLAB to compute mechanical stresses in the rotor and its displacement.

2.4 Postprocessing

A secondary GUI, named MMM (Magnetic Model Manipulation), manages the postprocessing of flux maps resulting from corresponding FEA simulation options.

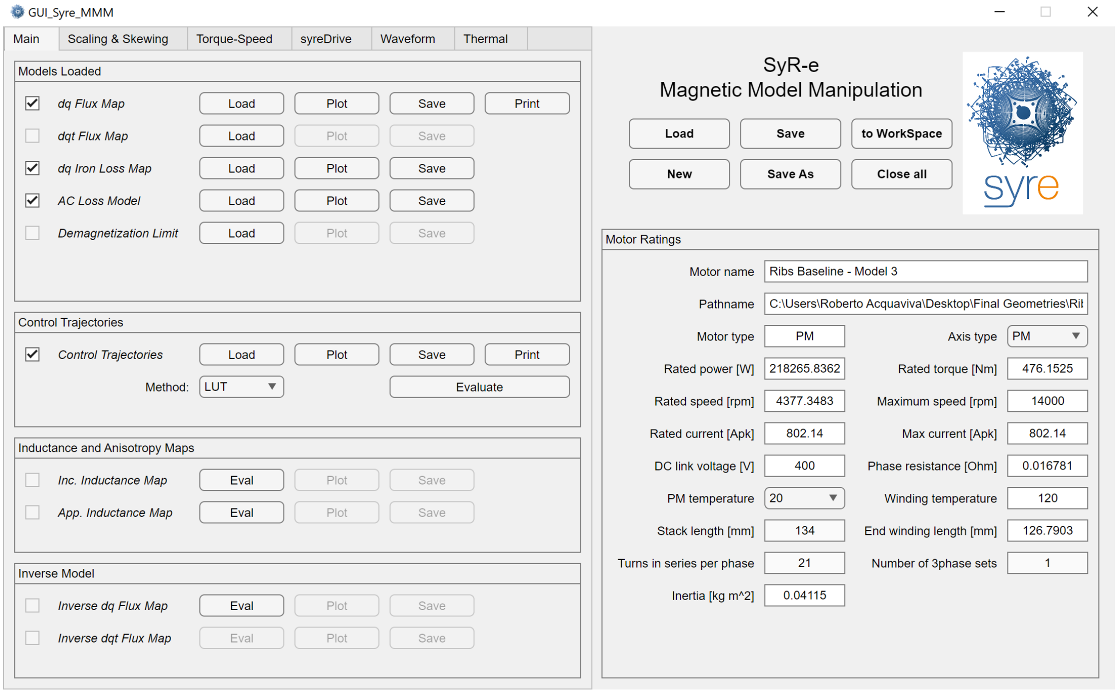

Models Loaded

☑ *dq Flux Map*

☐ *dqt Flux Map*

☑ *dq Iron Loss Map*

☑ *AC Loss Model*

☐ *Demagnetization Limit*

Control Trajectories

☑ *Control Trajectories*

Method: LUT

Inductance and Anisotropy Maps

☐ *Inc. Inductance Map*

☐ *App. Inductance Map*

Inverse Model

☐ *Inverse dq Flux Map*

☐ *Inverse dqt Flux Map*

Motor Ratings

Motor name: Ribs Baseline - Model 3
Pathname: C:\Users\Roberto Acquaviva\Desktop\Final Geometries\Ril
Motor type: PM
Axis type: PM
Rated power [W]: 218265.8362
Rated torque [Nm]: 476.1525
Rated speed [rpm]: 4377.3483
Maximum speed [rpm]: 14000
Rated current [Apk]: 802.14
Max current [Apk]: 802.14
DC link voltage [V]: 400
Phase resistance [Ohm]: 0.016781
PM temperature: 20
Winding temperature: 120
Stack length [mm]: 134
End winding length [mm]: 126.7903
Turns in series per phase: 21
Number of 3phase sets: 1
Inertia [kg m^2]: 0.04115

Figure 2.6: MMM GUI main tab in SyR-e

The MMM GUI in SyR-e, as depicted in Figure 2.6, offers various postprocessing options for electromagnetic FEA results, as explained in preceding sections. In the Main tab, four different model types for postprocessing can be loaded:

- **dq Flux Map:** The fundamental flux map in the *dq* current domain,
- **dqt Flux Map:** The dq Flux Map extended by rotor position dependency,
- **dq Iron Loss Map:** The results of the iron loss evaluation plotted in the *dq* current domain,

- **AC Loss Model:** The AC loss factor (see Section 2.2.1) as a function of frequency and temperature.

Depending on the chosen loaded model, several map manipulations are directly available in the Main tab:

- **Control Trajectories:** Computes the MTPA (Maximum Torque per Ampere) and MTPV (Maximum Torque per Voltage) curves of the machine.
- **Inductance and Anisotropy Maps:** The flux linkage gradients divided by the current gradients, plotted in the dq current plane. A fifth map represents the incremental anisotropy.
- **Inverse Model:** The dq and dqt Flux Maps can be inverted, showing currents and torque as functions in the dq flux linkage domain.
- **Current Angle Curves:** Parameters like torque, torque ripple, or power factor are plotted as functions of the current angle γ (counted from positive d axis to qs) at a fixed current amplitude $\hat{I}$.
- **Steady-State Short-Circuit:** Computed from the dq or dqt Flux Maps and based on the rated phase resistance, short-circuit torque and currents are presented as functions of rotor speed.

In the identically named tab, MMM can quickly apply motor scaling or skewing to already generated flux maps without rerunning FEA simulations. The newly created similar motors can be directly saved.

The Torque-Speed tab contains two important procedures:

1. **Operating Limits:** Outputs the operative limits of the evaluated machine for given voltage and current limitations, neglecting all losses except for the phase resistance. Plots of torque, power, current, voltage, and flux linkage over motor speed are the result.
2. **Efficiency Map:** Visualizes quantities such as efficiency η, output power, power factor, or total losses over a (T, n)-plane.

In the SyR-e Drive tab, it is possible to create an electric drive model that makes use of the simulated motor. It is possible to select a control strategy and define the converter main parameters. Finally, the model can be generated automatically in Simulink or Plecs to make use of it on the two simulation environments.
The are are two other useful tabs to describe: the Waveform tab, that allows to generate the waveform of of the motor for specific current levels and for short-circuit conditions, and the Thermal tab, that allows to generate the temperature map in a torque-speed plane.

2.5 Interaction with other Software

SyR-e gives the possibility to interact with external software to further investigate in the motor model generated with its application. This is necessary because, being SyR-e a pre-design tool, it has some limitations compared to other non-open source commercial software. Nevertheless, it is clear that an incredible amount of information can be generated with the use of SyR-e, that can save a lot of computational effort if used properly.

Therefore, after a preliminary study with SyR-e, it is possible to export the motor model in Motor-CAD (developed by Motor Design Ltd., now owned by Ansys) [4], Ansys Maxwell [5] and Simcenter MagNet (developed by Siemens) [6]. This software will allow to increase the simulation detail level, thanks to transient simulations or 3D model implementations. As already described in the previous section, the MMM GUI allows the interface with PLECS [7], allowing to create a circuit based models regarding electrical, magnetic and thermal domains.

Chapter 3

High-speed Motor Design for Traction Applications

3.1 The high-speed concept

High-speed electrical machines have been developed and used for a long time. The vast amount of their engineering applications is the proof of how mature and reliable this technology has become during the last decades. Based on the literature, the general definition of high-speed, when related to electric motors, can be to speeds that exceed 10000 rpm. In the automotive industry, several company adapted high speed motors for their EV and BEV power-train development since many years. For example, in 2007, Toyota was already using a 14000 rpm motor on the Toyota Camry Hybrid Sedan, supplying an additional power of 70 kW to support the 108 kW thermal engine (3.3).

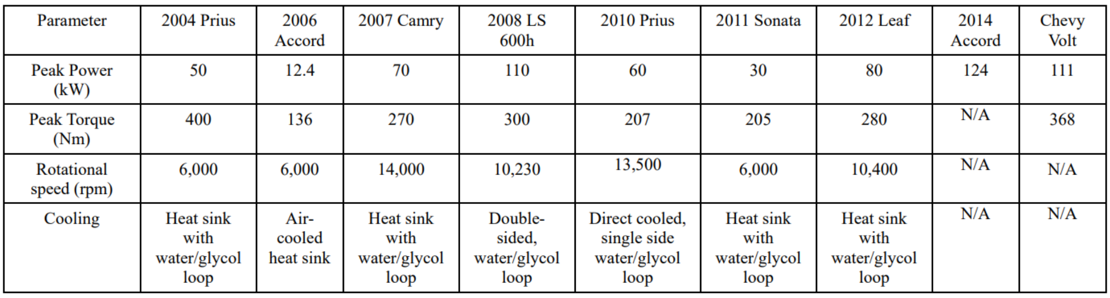

Parameter	2004 Prius	2006 Accord	2007 Camry	2008 LS 600h	2010 Prius	2011 Sonata	2012 Leaf	2014 Accord	Chevy Volt
Peak Power (kW)	50	12.4	70	110	60	30	80	124	111
Peak Torque (Nm)	400	136	270	300	207	205	280	N/A	368
Rotational speed (rpm)	6,000	6,000	14,000	10,230	13,500	6,000	10,400	N/A	N/A
Cooling	Heat sink with water/glycol loop	Air-cooled heat sink	Heat sink with water/glycol loop	Double-sided, water/glycol loop	Direct cooled, single side water/glycol loop	Heat sink with water/glycol loop	Heat sink with water/glycol loop	N/A	N/A

Figure 3.1: Benchmarking of old EV and BEV electric motors devoloped by companies [8]

In 2012, Nissan designed launched Nissan Leaf, a full electric vehicle with 160km of autonomy, adopting a 10400 rpm motor able to deliver a power of 80 kW.

In recent years, the demand for higher power and autonomy in electric cars has seen a significant surge. This surge has compelled companies in the automotive industry to devise electric motors that are not only more powerful but also compact and highly efficient. In response to these demands, the integration of high-speed motors in Electric Vehicles (EVs) has gained traction.

One perceived advantage of high-speed electric machines is their ability to reduce system weight for a given level of power conversion. [9] This reduction in weight is particularly crucial in mobile applications where lighter components translate to a lower overall load and higher vehicle efficiency. However, in the automotive context, space is often even more critical than weight. To meet customer expectations for comfort, increased battery capacity for extended autonomy, and additional components, a compact motor becomes essential.

More specifically, the volumetric power density of an electrical machine is improved when the volume is reduced at a constant torque and speed. Alternatively, speed must be increased to compensate for decreasing torque. [10] Additionally, to achieve higher torque density, one must consider enhancing either current density or flux density. Increased current density can be realized with improved cooling to prevent overheating, a challenging task when reducing the dimensions and heat exchange surfaces. Augmented flux density can be achieved by using more expensive materials with superior magnetic properties.

Furthermore, when considering an electric drive unit in which an electric motor is coupled with a gearbox to transfer power to the vehicle's wheels, a higher motor speed can result in a more efficient system. This advantage arises from the powertrain's enhanced capability to cover a wide range of speed-demanding operating points, allowing for the optimal utilization of the motor's efficiency across frequently encountered torque-speed combinations.

Nonetheless, achieving high-speed motor operation presents numerous design challenges. Attention must be devoted to mechanical strength, vibration control, and the mitigation of energy losses. High-speed rotation generates significant centrifugal forces, which can induce mechanical stress and deformation in motor components. Therefore, the design of bearings and rotor assemblies must account for these forces to prevent premature failure or imbalance-induced vibrations.

The choice of materials for constructing high-speed electric motors is critical. These materials must be both robust and lightweight to reduce inertia and withstand the stresses of high-speed operation. High-speed motors may also experience vibrations resulting from electromagnetic forces, such as cogging or harmonics. Additionally, eddy currents and hysteresis losses in the iron components increase proportionally with frequency, along with electromagnetic interference.

Undoubtedly, the design of high-speed motors presents numerous challenges. However, the performance and efficiency benefits they bring to the entire powertrain make these challenges worthwhile. In striving for advancements in high-speed motor technology, we unlock opportunities to redefine the future of electric mobility.

3.2 High-speed IPM Synchronous Motors Designs overview

The most frequently used electric motors for traction application are Induction Motors (IM) and Permanent Magnet Synchronous Motors (PMSM), however the second technology is more suitable for high rotational speeds. The IM are robust, reliable and their design is simple and cheap to produce. Nevertheless, it is well known that PMSM machines are more efficient thanks to the use of permanent magnets in the rotor, that are producing a magnetic field without the use of a current flow. Nowadays, the most performing permanent magnets are made of rear earth materials, such as Neodymium, used for Neodymium-Ferrum-Boron (NdFeB) magnets, Samarium and Cobalt, used for Samarium-Cobalt (SmCo) magnets. The first category particularly is the most used thanks to its high residual flux density (B_r) of generally around 1.4 T and its good demagnetization properties.

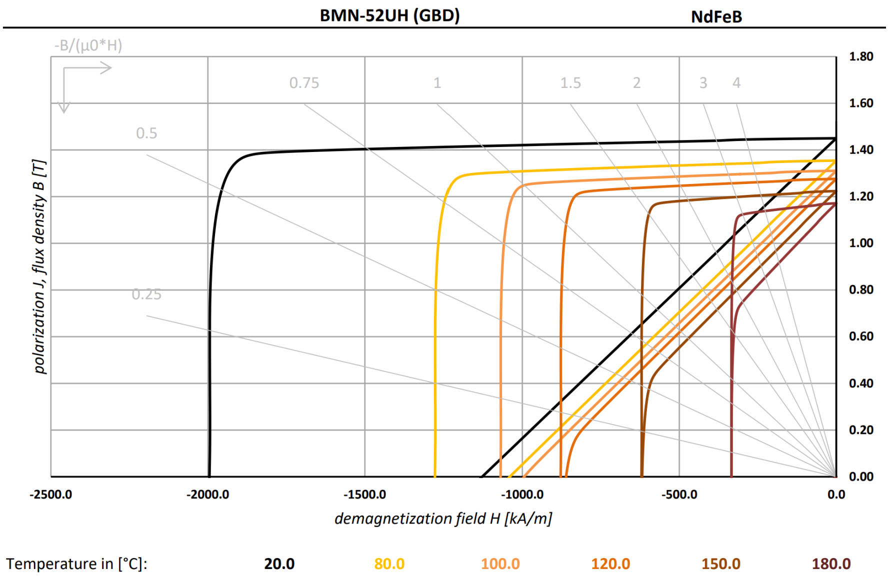

Figure 3.2: B-H Curve of BMN-52UH NdFeB magnet [11]

Among the PMSMs possible designs, one in particular is leading in the EVs industry. This specific motor is the Interior Permanet Magnets (IPM) Synchronous Motor.

In Figure 3.3 it is possible to see that there are three main popular geometries

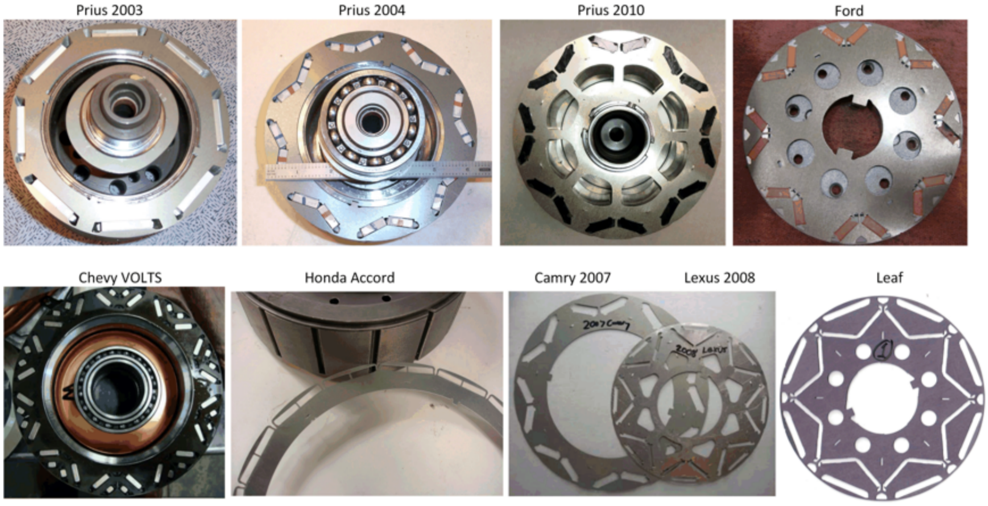

Figure 3.3: PMSM electric motors from different electric car producers [8]

of IPM motors among the ones used by automotive companies: the Flat-type, the V-type and the Triangle-Type (Figure 3.4).

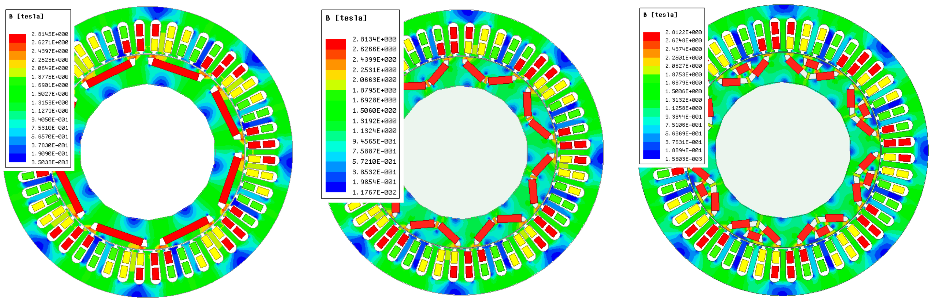

(a) (b) (c)

Figure 3.4: The three most popular IPM motors geometries used for automotive applications: (a) Flat-type; (b) V-type; (c) Triangle-type. [12]

The popularity of this particular lamination geometry can be attributed to its excellent mechanical retention properties. Notably, it ensures the secure fixation of the permanent magnets within the rotor structure, significantly reducing the risk of the rotor becoming dislodged, even under the duress of high speeds and mechanical stress.

However, the presence of iron encasing the magnets introduces a challenge related to flux leakage. A portion of the magnetic field tends to preferentially flow through the iron surrounding the magnets rather than effectively crossing the air gap. This phenomenon occurs due to the iron's higher magnetic permeability compared to that of the air. While burying the magnets within the rotor iron enhances mechanical stability, it simultaneously hinders the optimal production of air gap flux by the magnets.

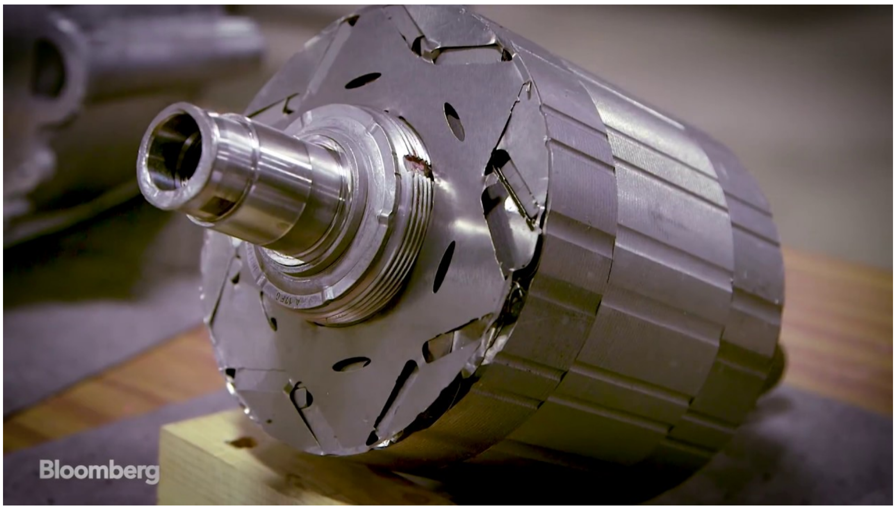

Figure 3.5: Tesla Model 3 Motor [13]

Tesla developed for its Tesla Model 3 a single barrier V-Shape IPM motor that has become a example to look at for other automotive industries because of its performant and efficient design. This particular motor will be further investigated in the next chapters and it is worth to introduce it now to make use of its rotor geometry to better understand what described before.

In Figure 3.6, a no-load analysis (absence of current) of the Model 3 geometry simulated in FEMM is presented. As illustrated in the diagram, two elements of the rotor pole exhibit a magnetic flux density (B) that reaches a level high enough to saturate the iron, measuring around 2 T. These two components, known as the Rib and the Bridge (located on both sides of the rotor pole), serve the sole purpose of providing structural support for the magnets. However, these two iron components inadvertently short-circuit the magnet's flux lines. This results in a flux leakage effect, where a portion of the magnet's magnetic field is effectively used only to saturate the two retaining features. Consequently, only a fraction of the magnet contributes to creating a useful magnetic field that spans the motor's airgap and interacts with the windings. cross the motor airgap and concatenates the windings.

Due to the centrifugal force acting on the magnets and on the outer part of the rotor yoke, the dimension of the rib and the two bridges increase with the maximum speed that the rotor aims to reach. On the other hand, the thicker those

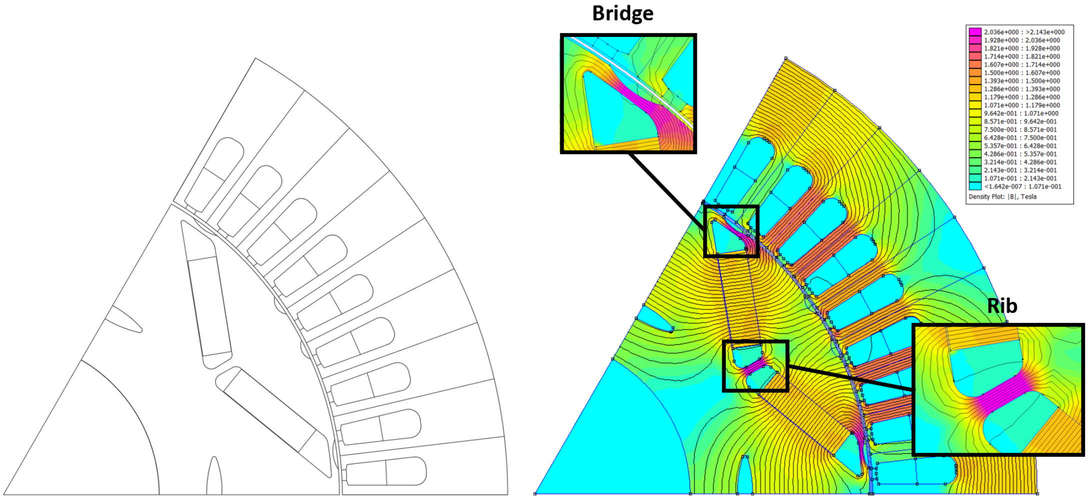

Figure 3.6: Tesla Model 3 Motor single pole model. Left: Drawing created in AutoCAD. Right: FEMM No-Load analysis with focus on Rib and Bridge

features are, the higher the is the flux leakage due to the higher permeability of these iron parts.

In order to increase the speed of this motor type, the optimal solution would to find a way to have a structural retaining of the rotor parts without a drastic degradation of the performance of the motor.

3.3 Wrapped Rotor solution

As already explained in the previous section, when the rotor is spinning, centrifugal force is acting on its parts, causing a displacement in the radial direction. This centrifugal force has a quadratic relationship with speed. In Permanent Magnets machines, the magnets can be surface mounted or buried in the iron. In the first case, glue is typically used to keep the magnets attached to the rotor iron. For IPM motors instead, the iron itself is protecting the magnets to fly away from the rotor. In both cases, at very high speeds this solutions are not sufficient. Furthermore, as already reported in the last section, the most popular magnets are made of NdFeB or SmCo. These PM materials have high compressive strength but low tensile strength and can't withstand the centrifugal force generated by high rotational speed [14]. Hence, high speed operation requires preferably a high-strength retaining sleeve, pre-stressing the PMs.

3.3.1 Overview and applications of the existing high-speed Wrapped Motor Designs

SPM motors

The most widely adopted application of sleeves in electric motors is prominently observed in high-speed Surface Permanent Magnet (SPM) motors.

SPM high-speed motors are required in a variety of applications, including turbochargers and electrified superchargers, flywheel energy storage systems, turbomolecular pumps, more electric engines, high-speed spindles, gas compressors, and microturbines (Figure 3.7).
This technology is widely used for small motors thanks to its high power density and its simple structure.

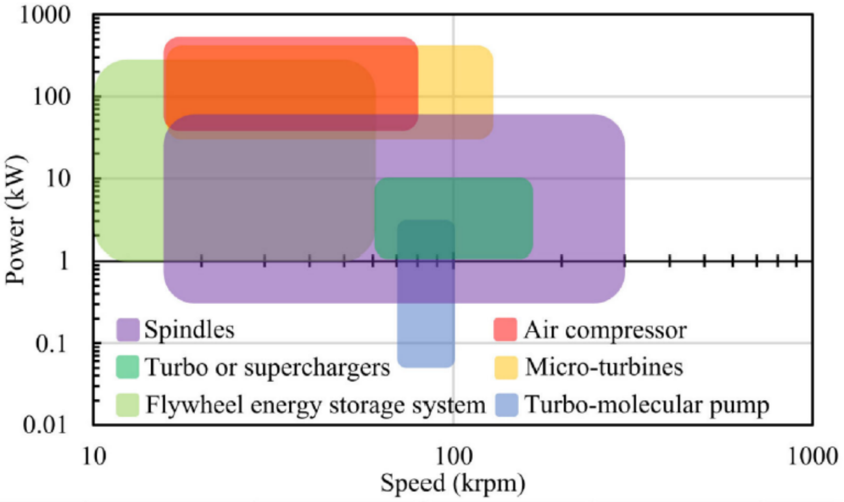

Figure 3.7: Power/speed ranges of the high-speed motors for different applications [15]

The design and analysis of wrapped SPMs have been deeply investigated by several authors [16]. The need of compressing the magnets against the rotor is essential in this geometry, and this makes the SPM motor the main candidate for the sleeve to be used. Thanks to the simplicity of its design, the rotor lamination of the SPM motor is taken as a reference for the sleeve technology implementation, so that many analytical model have been created referring to it.

Looking at the literature, one of the main problematic studied on SPM wrapped motors regards the direct application of the sleeve on the permanent magnets. When the pole coverage α_e is lower than one (Figure 3.8), the bending stress caused

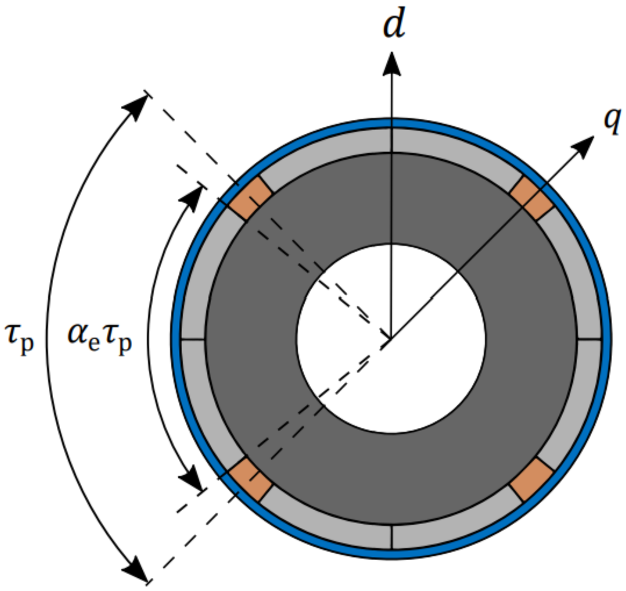

Figure 3.8: A wrapped 4-pole SPM rotor with circumferentially segmented PMs and pole gap fillers, leading to a pole coverage ratio < 1. d and q axes are indicated [17].

by the edges of the PMs and the stress induced by thermal expansion of the rotor are also harmful to the sleeves and may crack the sleeves [18]. Despite this problem, if well designed the SPM motor performs really well at high speed making use of a retaining sleeve.

However, this motor technology is not optimal for traction applications. Firstly, they tend to exhibit a higher risk of demagnetization due to mechanical and thermal stresses during variable load operation, which is common in traction applications. This could lead to a reduction in performance over time. Additionally, the design of SPM motors may be more complex to achieve the desired balance between torque density and other operational requirements in traction motors. This can be attributed to the way SPM motors generate torque. Due to the isotropy of the rotor, the inductance in the d axis (the axis of the rotor flux) and the one in the q axis (the axis at 90 electrical degrees with the rotor flux) are equal: $L_d = L_q$. This leads to an absence of reluctance torque, and the formula of the torque production of SPM motors appears to be:

$$T = \frac{3}{2} \cdot p \cdot \lambda_{PM} \cdot i_q$$

Furthermore, the variable load operation of an electric motor would require a good ability to adjust the internal magnetic flux by field weakening. In sleeved SPMs, there is an high magnetic airgap, that is the sum of the mechanical airgap, the thickness of the magnet and the sleeve thickness. This means that the inductance value is low and the flux weakening operation requires a very high current.

IPM motors and the Tesla Model S motor

As already explained in the previous sections, Interior Permanent Magnet (IPM) motors are often considered more suitable for traction applications. The internal arrangement of permanent magnets in IPM motors allows for greater control over the distribution of magnetic flux, resulting in better torque and efficiency management. The anisotropy of the magnetic circuit ($L_d \neq L_q$) of the rotor gives a good component of reluctance torque in addiction to the one generated with the magnets flux. The torque production of this motors can be evaluated with the espression:

$$T = \frac{3}{2} \cdot p \cdot [\lambda_{PM} \cdot i_q + (L_q - L_d) \cdot i_q \cdot i_d]$$

Moreover, thanks to the insertion of the magnets in the rotor iron, the magnetic airgap of the IPM motors results smaller than the SPM one, and it is just the sum of the mechanical airgap and the thickness of the sleeve, if present. This allows to perform field weakening applying using a lower current, making this operation efficient over a wide range of operating points.

In 2021, Tesla developed a traction motor that combines the advanced retaining properties of sleeve technology described for the SPM motors and the unquestionable advantages of the IPM motors for traction applications. This motor has been designed for the Model S Plaid car (Figure 1.3), that required 3 powerful motors to achieve the amazing performance of a 0-100 km/h acceleration of 2.1 s and maximum speed of 322 km/h.

In Figure 3.9, it is possible to see the Tesla Model S Plaid carbon wrapped rotor (Tesla patent [20]). The magnets, the pole piece and the rotor back iron are kept together in a compact structure thanks to the compressive strength between the sleeve and the shaft. As can be noticed, the sleeve allows to get rid of the radial ribs and the bridges of the iron lamination, that are the main cause of flux leakage of the standard IPM V-Shape motor. The ribs-free flux barrier allows also to add more magnet, leading to a better utilization of the available cross-sectional area in the rotor.

Nevertheless, the sleeve application induce increased manufacturing complexity and costs, as the rotor contains the sleeve as an extra component, and with the separated inner and outer laminations, also more parts in general.

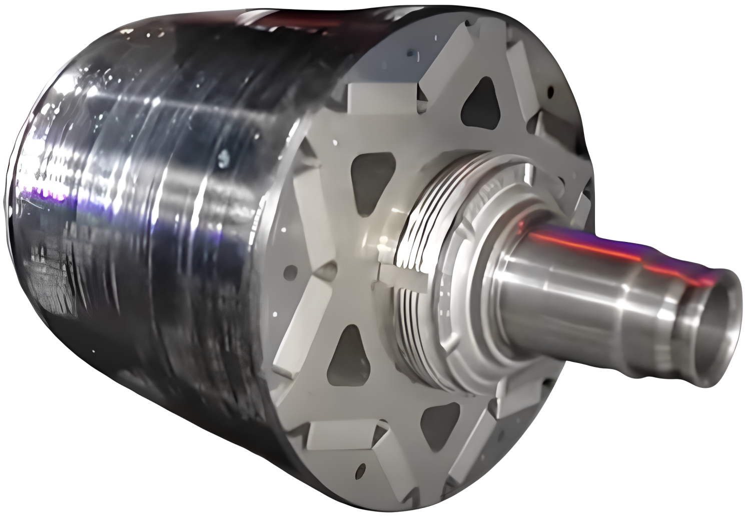

Figure 3.9: Tesla Model S Motor - Carbon wrapped rotor [19]

3.3.2 Materials

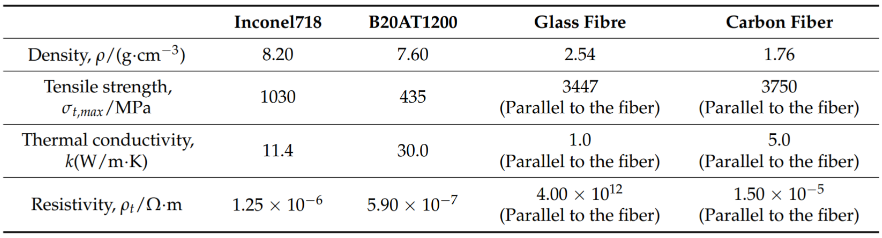

	Inconel718	B20AT1200	Glass Fibre	Carbon Fiber
Density, $\rho/(\mathrm{g{\cdot}cm^{-3}})$	8.20	7.60	2.54	1.76
Tensile strength, $\sigma_{t,max}/\mathrm{MPa}$	1030	435	3447 (Parallel to the fiber)	3750 (Parallel to the fiber)
Thermal conductivity, $k(\mathrm{W/m{\cdot}K})$	11.4	30.0	1.0 (Parallel to the fiber)	5.0 (Parallel to the fiber)
Resistivity, $\rho_t/\Omega{\cdot}\mathrm{m}$	1.25×10^{-6}	5.90×10^{-7}	4.00×10^{12} (Parallel to the fiber)	1.50×10^{-5} (Parallel to the fiber)

Figure 3.10: Comparison between material properties used for housing (e.g Inconel 718) or motor lamination (e.g. B20AT1200, a silicon steel) and sleeve materials like glass fiber and carbon fiber) [21]

- Fiber-Reinforced Composites: Composites, such as carbon fiber or glass fiber, are commonly used for rotor wrapping due to their excellent mechanical properties.
  Key properties include:
  - Tensile Strength: High tensile strength, making them suitable for high-speed applications.
  - Low Density: Lightweight, reducing rotor inertia and aiding in rapid acceleration.

- Epoxy Resins: Epoxy resins are often used as binders for composite materials,

providing mechanical support and electrical insulation.
Key properties include:
- Adhesive Strength: Good adhesion to fibers, ensuring a strong bond.
- Dielectric Properties: High electrical insulation to prevent electrical losses.

3.3.3 Wrapping techniques

The two main wrapping techniques to apply the sleeve to the rotor are shown and quickly described in Figure 3.11 and Figure 3.12. In the first methodology, the sleeve is pre-constructed and then assembled with the rotor trough pressing or temperature difference.

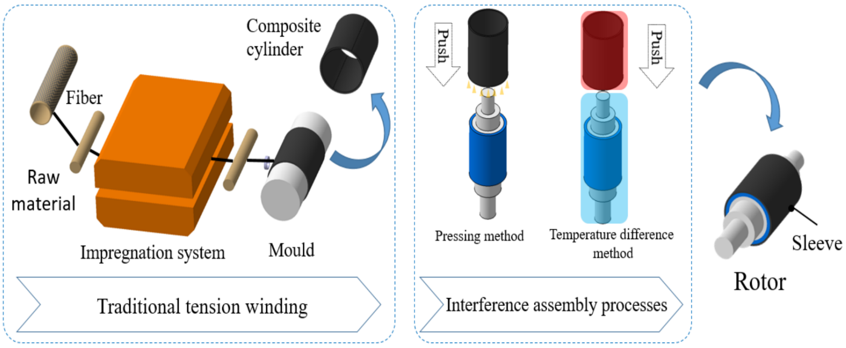

Figure 3.11: Sleeve application trough interference between the sleeve and the rotor using temperature difference or pressing. [21]

In the second methodology, the sleeve is directly wrapped around the rotor, appling the pre-stress keeping in tension the fiber.

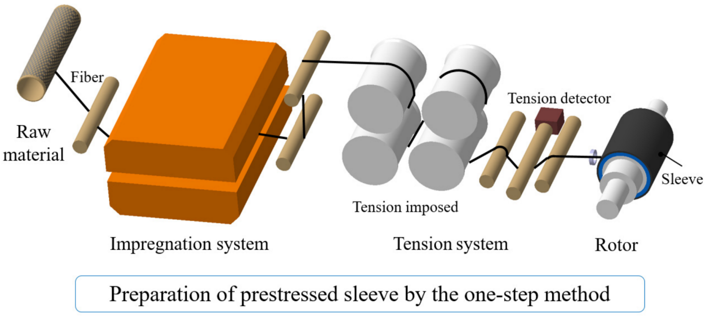

Figure 3.12: Sleeve application trough wrapping around the rotor, applying a pre-stress to the fiber. [21]

Chapter 4

Sleeve Design for Wrapped IPM motors

In this section, will be described the methodology for creating an analytical model useful for the design of a V-Type IPM motor that utilizes a sleeve for rotor containment at specific rotation speeds. The model aims to simplify the study of sleeve sizing and pretension characteristics required to support the mechanical structure of the rotor based on construction parameters and operating conditions. To facilitate this description, we will draw upon the study conducted by Josef Binder [17, 22] in collaboration with Energy Department of Poltecnico di Torino (DENERG) in his analysis of motors with a carbon sleeve, reporting parts of his work to include and explain the starting point of this thesis. The necessary conditions for designing such a motor, the equivalent model that simplifies the study of structural rotor containment, and the equations of the analytical model derived from his analysis will be outlined in the next sections.

4.1 Sleeve conditions

The conditions to impose when approaching the design of sleeves for wrapped IPM machines are in common with the SPM machines and are mandatory to ensure the structural containment of the rotor parts, the integrity of the magnets, of the iron parts and of the sleeve itself. Hereafter, the rules that will be applied for the design study of the V-type rotor are listed:

1. PMs must remain securely attached to the rotor back-iron, preventing any risk of detachment and ensuring continuous compression along their height.
2. PM compressive stress must remain within acceptable limits during this state of compression.

3. Tensile stress in the PMs, potentially occurring in the width direction, must remain below the considerably lower PM tensile stress limit.

4. Sleeve tensile stress, in both circumferential and fiber directions, should not exceed the designated sleeve tensile stress limit.

5. Sleeve radial stress must remain below the significantly lower stress limit in a direction perpendicular to the fibers.

Condition 1 is the main design constraint to be followed, which is why the sleeve design can be also described as a “sleeve prestress design”, primarily aiming to prevent PM lift-off. Conditions 2 to 6 on the other hand ensure, that while fulfilling condition 1, all loaded rotor components remain intact. Especially conditions 4 and 5 for the sleeve stress must be checked in regions of maximum sleeve stress, usually where bending occurs [17].

It is also essential to understand what are the source of stress for the materials inside the rotor and their nature:

- Speed causes centrifugal body forces acting in radial direction on all rotor components. As the PMs are not structurally connected the rotor back-iron, these body forces tend to push the PMs (and the pole pieces) away from the inner lamination.

- Prestressing the sleeve onto the rotor adds both radial and circumferential stress to the sleeve. A larger prestress results in a larger compression of the PMs.

- Rotor temperature increase leads a to larger thermal expansion of PMs and lamination compared to the CF-sleeve. The outcome on the stresses is the same as for an increased prestress.

The target is to minimize the sleeve thickness ensuring the motor integrity. In order to evaluate the stress in the rotor parts and in the sleeve, considering also the effect of an applied prestress, a FEA software using a multiple body approach has to be used for the simulations. This can be computationally expensive and not supported on open source software. Therefore, an analytical method to forecast the behaviour of the rotor components at different speeds for various sleeve thickness and prestress values can be a powerful pre-design tool for the developement of this type of machines.

4.2 Equivalent Rotor Geometry

In this section, we will delve into the simplification process of the parametrized and streamlined wrapped rotor depicted in Figure 3.9. The key strategy involves creating a structure that can be efficiently analyzed to achieve the previously mentioned objectives. Initially, the rotor is segmented into three distinct components:

1. The sleeve, denoted as index 1.
2. The combined PMs and pole piece, identified as index 2.
3. The inner lamination, designated by index 3.

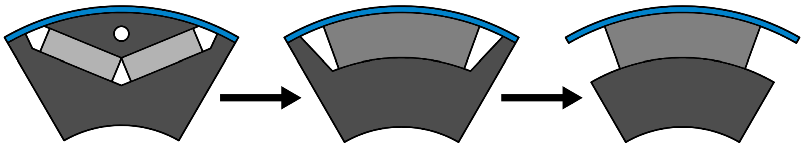

Figure 4.1: Simplifications of the wrapped rotor geometry towards the analytical sleeve stress design [22]

The combined PMs and pole piece (abbreviated as PM+pp) are reconfigured into a ring segment with equivalent density and elastic properties, as illustrated in Figure 4.1. This ring segment makes contact with the inner lamination at an average radius dependent on the specific PM position. Additionally, the contact between the sleeve and inner lamination is disregarded, transforming the inner laminate into a counterpart solely for the compression of the equivalent PM ring segment. All material properties of the sleeve and the inner lamination remain unaltered.

The resulting configuration includes the sleeve as a continuous ring, the PM+pp as a ring segment, and the inner laminates once again as a continuous ring. This configuration allows for the utilization of well-established stress and displacement solutions in the design of the sleeve.

4.3 Stress and Displacement of the Simplified 3-layer Rotor

This section is reserved for simply reporting and explaining the equations coming from the thesis work of Josef Binder on the development of an analytical model for the wrapped rotors structural analysis. In collaboration with Politecnico di Torino and D.IMEAS, the results of the analytical model have been validated trough 3D FEA softwares.

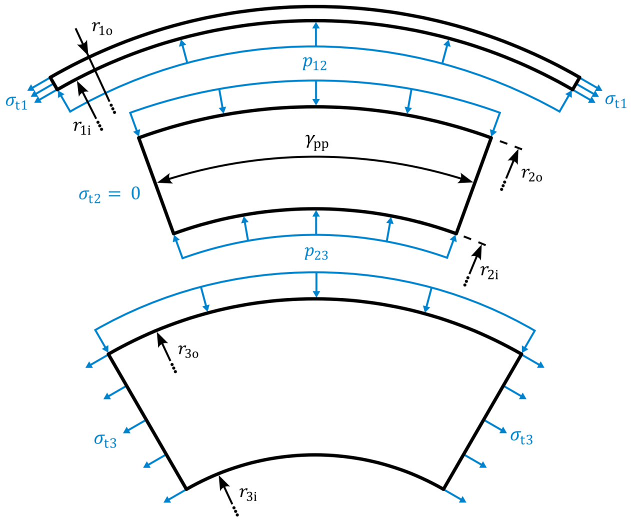

Figure 4.2: Radii (black) and stresses (blue) in the simplified 3-layer equivalent rotor. [22]

4.3.1 Sleeve Quantities

The analytical model equations are applicable to materials with homogeneous and isotropic elastic properties. This assumption is extended to all three rotor layers. Although this assumption oversimplifies the orthotropic CF-sleeve, it enables a more efficient calculation of the sleeve quantities and provides reasonably accurate results.

Given that the designed retaining sleeves are typically thin compared to their diameter, the computation of sleeve stresses and displacements can be semplified by treating them as "thin shells." When considered "infinitely thin," the radial stress within the disk becomes negligibly small, effectively zero. Simultaneously, the circumferential stress within the sleeve becomes independent of the radial coordinate. In this context, the sleeve radius $r_{1,av}$ can be introduced as follows:

$$r_{1,av} = \frac{r_{1o} + r_{1i}}{2}$$

Referring to the definitions in Figure 4.2, assuming inner contact pressure p_{12} to PM+pp without an outer contact, the sleeve quantities are as follows:

$$\sigma_{r1} = 0$$
$$\sigma_{t1} = p_{12} \cdot \frac{r_{1,av}}{h_1} + \frac{\omega^2 \cdot \varepsilon_1 \cdot r_{1,av}^2}{2}$$
$$u_1 = p_{12} \cdot \frac{r_{1,av}^2}{2E_1 h_1} + \frac{\omega^2 \cdot \varepsilon_1 \cdot r_{1,av}^3}{3E_1} + r_{1,av} \cdot \alpha_{th,1} \cdot \Delta T_1$$

4.3.2 PM+pp Quantities

Determining the quantities in the middle layer of the rotor presents a greater challenge. Unlike the continuous disk of the previous layers, the equivalent PM+pp segment is divided into circumferentially distributed pieces that are isolated from each other. These pieces can no longer transmit circumferential stress, leading to the fundamental assumption:

$$\sigma_{t2} = 0$$

Let's begin by examining the dynamic equilibrium equation of a disk volume element with a constant axial thickness, considering the PM+pp segment (denoted as subscript 2):

$$\frac{d}{dr}(r \cdot \sigma_{r2}) - \sigma_{t2} + \frac{\omega^2 \cdot \varepsilon_2 \cdot r^2}{2} = 0$$

With the circumferential stress being zero, this equation can be integrated and a first integration constant needs to be introduced, denoted as C_1. This yields an expression for the radial stress within the middle rotor layer:

$$\sigma_{r2} = \frac{C_1}{r} - \frac{\omega^2 \cdot \varepsilon_2 \cdot r^2}{3}$$

Utilizing the ordinary equation for displacement and Hooke's law while respecting $\sigma_{t2} = 0$, the result is:

$$\frac{du_2}{dr} = \frac{C_1}{E_2 r} - \frac{\omega^2 \cdot \varepsilon_2 r^2}{3E_2} + r \cdot \alpha_{th,2} \cdot \Delta T_2$$

Another integration, incorporating a second constant C_2, provides the formula for the radial displacement:

$$u_2 = C_1 \cdot \frac{1}{E_2} \cdot \ln r + C_2 - \frac{\omega^2 \cdot \varepsilon_2}{9E_2} \cdot r^3 + r \cdot \alpha_{th,2} \cdot \Delta T_2$$

4.3.3 Inner Lamination Quantities

In the case of the innermost layer, the inner lamination ring is considered. Here, it is assumed that the inner contact pressure is zero, implying that the laminates are mounted onto the shaft without any press or shrink fit. However, on the outer radius, the ring is subjected to p_{23}, which leads to the following expressions for stresses and displacement:

$$\begin{aligned}
\sigma_{r3} &= -p_{23} \cdot \frac{r_{3o}^2}{r_{3o}^2 - r_{3i}^2} \left(1 - \left(\frac{r_{3i}}{r}\right)^2\right) \\
&\quad + \frac{\omega^2 \epsilon_3}{8} \left(r_{3o}^2 + r_{3i}^2 - \left(r_{3o} r_{3i}\right)^2 - r^2\right) \\
\sigma_{t3} &= -p_{23} \cdot \frac{r_{3o}^2}{r_{3o}^2 - r_{3i}^2} \left(1 + \left(\frac{r_{3i}}{r}\right)^2\right) \\
&\quad + \frac{\omega^2 \epsilon_3}{8} \left(r_{3o}^2 + r_{3i}^2 + \left(r_{3o} r_{3i}\right)^2 - 1 + 3\nu_3 - \frac{r^2}{3} + \nu_3 \cdot r^2\right) \\
u_3 &= -p_{23} \cdot \frac{1}{E_3} \cdot \frac{r_{3o}^2}{r_{3o}^2 - r_{3i}^2} \left((1 - \nu_3) \cdot r + \frac{r_{3i}^2}{r} \cdot (1 + \nu_3) \cdot \frac{1}{r}\right) \\
&\quad + \frac{\omega^2 \epsilon_3}{8E_3} \cdot r \cdot \left((r_{3o}^2 + r_{3i}^2)(1 - \nu_3) + (1 + \nu_3) \left(r_{3o} r_{3i}\right)^2 - 1 - \nu_3 \cdot r^2\right) \\
&\quad + r \cdot \alpha_{th,3} \cdot \Delta T_3
\end{aligned}$$

Collecting all these equations (excluding $\sigma_{r1} = 0$ and $\sigma_{t2} = 0$), a total of seven equations a resulting for the sleeve (σ_{t1}, u_1), the PM+pp segment (σ_{r2}, u_2), and the inner lamination (σ_{r3}, σ_{t3}, u_3). This equation system involves four unknowns: the two contact pressures (p_{12}, p_{23}), and the constants (C_1, C_2). Consequently, four boundary conditions are required to solve the problem.

4.3.4 Boundary Conditions Before Lift-off

First, let's consider the scenario where the second layer is still in contact with the inner ring, prior to the lift-off of the PMs. The two boundary conditions can be derived from the equality of radial stresses:

$$\begin{aligned}
\sigma_{r2}(r_{2o}) &= -p_{12} \\
\sigma_{r2}(r_{2i}) - \sigma_{r3}(r_{3o}) &= 0
\end{aligned}$$

To introduce prestress to the sleeve, let's take into account the interference fit between the sleeve and the second layer, represented by the assembly interference

Δu_{12} between the two radial displacements u_1 and u_2 at the interface radius $r_{1i} = r_{2o}$. Between the second and third layers, the interference is zero in the absence of a prestressed fit between PMs and the inner lamination. Therefore, the equations results in:

$$\begin{aligned} u_1 - u_2(r_{2o}) &= \Delta u_{12} \\ u_2(r_{2i}) - u_3(r_{3o}) &= 0 \end{aligned}$$

In practice, components that are meant to fit together can be manufactured with the interference already present. To install the sleeve, thermal expansion or contraction can be utilized. By cooling the rotor without applying the wrapping and/or heating the sleeve before mounting it onto the rest of the rotor, the return to the construction temperature results in a tight fit, creating prestress.

The equivalent interference can be calculated as follows:

$$\Delta u_{12} = \sigma_{t1} \cdot \frac{r_{1,av}}{E_1}$$

4.3.5 Boundary Conditions After Lift-off

If, for a given prestress and temperature, the rotor speed becomes too high, the PMs will detach from the rotor at a certain point. When this occurs, the sign of the contact pressure p_{23} changes. this moment can be determined by monitoring p_{23}):

$$p_{23} = \begin{cases} > 0 : & \text{PMs are compressed, no lift-off} \\ \leq 0 : & \text{PMs have detached} \end{cases}$$

Once the second condition is satisfied, the boundary conditions must be adjusted. While $\sigma_{r2}(r_{2o}) = -p_{12}$ and $\sigma_{r2}(r_{2i}) - \sigma_{r3}(r_{3o}) = 0$ remain unchanged because the PM+pp segments are pushed outward into the wrapping, $u_1 - u_2(r_{2o}) = \Delta u_{12}$ and $u_2(r_{2i}) - u_3(r_{3o}) = 0$ need to be replaced. $\sigma_{r2}(r_{2i}) = 0$ confirms that the equivalent middle segment is detached, ensuring that the radial stress at its inner radius is zero. Equation $p_{23} = 0$ solves the equations for the inner lamination ring, which is rotating independently from the other layers.

4.4 System equations in matrix form

To implement efficiently the equations in MATLAB code, the Symbolic Toolbox [23] offers a convenient approach. This toolbox enables the prior definition of variables and their utilization within equations. In this specific context, the analytical equations are employed to determine the parameters of the sleeve, resulting in two pressures, p_{12} and p_{23}, and two constants, C_1 and C_2.

However, it's worth noting that the Symbolic Math Toolbox is computationally intensive. The equations are evaluated within two nested for-loops, iterating through various sleeve thicknesses and prestresses. Consequently, the script's execution becomes slow and time-consuming.

To enhance the code's efficiency, a viable solution is to reformulate the equations into a matrix form. This approach allows the output evaluations to be computed as products of input equations and a matrix of constants.

Hereafter, the 9 equations for stress and displacement related to the Sleeve, the PM+PP and the inner laminate are reported again in a compact summary with the purpose of having them easily within reach when going trough the conversion into matrix form.

Sleeve quantities:

$$\begin{aligned}
&\sigma_{\mathrm{r1}} = 0\\
&\sigma_{\mathrm{t1}} = p_{12} \cdot \frac{r_{1,\mathrm{av}}}{h_1} + \omega^2 \cdot \varrho_1 \cdot r_{1,\mathrm{av}}^2\\
&u_1 = p_{12} \cdot \frac{r_{1,\mathrm{av}}^2}{E_1 \cdot h_1} + \omega^2 \cdot \varrho_1 \cdot \frac{r_{1,\mathrm{av}}^3}{E_1} + r_{1,\mathrm{av}} \cdot \alpha_{\mathrm{th},1} \cdot \Delta T_1
\end{aligned}$$

PM+PP quantities:

$$\begin{aligned}
&\sigma_{\mathrm{r2}} = \frac{C_1}{r} - \omega^2 \cdot \frac{\varrho_2}{3} \cdot r^2\\
&\sigma_{t2} = 0\\
&u_2 = C_1 \cdot \frac{1}{E_2} \cdot \ln r + C_2 - \omega^2 \cdot \frac{\varrho_2}{9E_2} \cdot r^3 + r \cdot \alpha_{\mathrm{th},2} \cdot \Delta T_2
\end{aligned}$$

Inner laminate quantities:

$$
\begin{aligned}
\sigma_{\mathrm{r3}} &= -p_{23} \cdot \frac{r_{3\mathrm{o}}^2}{r_{3\mathrm{o}}^2 - r_{3\mathrm{i}}^2} \cdot \left(1 - \left(\frac{r_{3\mathrm{i}}}{r}\right)^2\right) \\
&\quad + \omega^2 \cdot \varrho_3 \cdot \frac{3 + v_3}{8} \cdot \left(r_{3\mathrm{o}}^2 + r_{3\mathrm{i}}^2 - \left(\frac{r_{3\mathrm{o}} \cdot r_{3\mathrm{i}}}{r}\right)^2 - r^2\right) \\
\sigma_{\mathrm{t3}} &= -p_{23} \cdot \frac{r_{3\mathrm{o}}^2}{r_{3\mathrm{o}}^2 - r_{3\mathrm{i}}^2} \cdot \left(1 + \left(\frac{r_{3\mathrm{i}}}{r}\right)^2\right) \\
&\quad + \omega^2 \cdot \varrho_3 \cdot \frac{3 + v_3}{8} \cdot \left(r_{3\mathrm{o}}^2 + r_{3\mathrm{i}}^2 + \left(\frac{r_{3\mathrm{o}} \cdot r_{3\mathrm{i}}}{r}\right)^2 - \frac{1 + 3v_3}{3 + v_3} \cdot r^2\right) \\
u_3 &= -p_{23} \cdot \frac{1}{E_3} \cdot \frac{r_{3\mathrm{o}}^2}{r_{3\mathrm{o}}^2 - r_{3\mathrm{i}}^2} \cdot \left((1 - v_3) \cdot r + r_{3\mathrm{i}}^2 \cdot (1 + v_3) \cdot \frac{1}{r}\right) \\
&\quad + \omega^2 \cdot \frac{\varrho_3}{E_3} \cdot \frac{3 + v_3}{8} \cdot r \cdot \left(\left(r_{30}^2 + r_{3\mathrm{i}}^2\right)(1 - v_3) + (1 + v_3)\left(\frac{r_{3\mathrm{o}} \cdot r_{3\mathrm{i}}}{r}\right)^2 - \frac{1 - v_3^2}{3 + v_3} \cdot r^2\right) \\
&\quad + r \cdot \alpha_{\mathrm{th},3} \cdot \Delta T_3
\end{aligned}
$$

4.4.1 Boundary Conditions Before Lift-Off

$$
\begin{aligned}
\sigma_{\mathrm{r2}}\left(r_{2\mathrm{o}}\right) &= -p_{12} \\
\sigma_{\mathrm{r2}}\left(r_{2\mathrm{i}}\right) - \sigma_{\mathrm{r3}}\left(r_{3\mathrm{o}}\right) &= 0 \\
u_1 - u_2\left(r_{2\mathrm{o}}\right) &= \Delta u_{12} \\
u_2\left(r_{2\mathrm{i}}\right) - u_3\left(r_{3\mathrm{o}}\right) &= 0
\end{aligned}
$$

The aim is to write every equation with the form:

$$K_1 \cdot C_1 + K_2 \cdot p_{12} + K_3 \cdot C_2 + K_4 \cdot p_{23} = G$$

This will allow to write the system of equation in matrix form:

$$
\begin{bmatrix} K_{11} & K_{12} & K_{13} & K_{14} \\ K_{21} & K_{22} & K_{23} & K_{24} \\ K_{31} & K_{32} & K_{33} & K_{34} \\ K_{41} & K_{42} & K_{43} & K_{44} \end{bmatrix} \cdot \begin{Bmatrix} C_1 \\ p_{12} \\ C_2 \\ p_{23} \end{Bmatrix} = \begin{Bmatrix} G_1 \\ G_2 \\ G_3 \\ G_4 \end{Bmatrix} \tag{4.1}
$$

1st Equation

$$\begin{aligned}\sigma_{\mathrm{r2}}\left(r_{\mathrm{2o}}\right) &= -\mathbf{p_{12}} \\ \frac{\mathbf{C_1}}{r_{\mathrm{2o}}} - \omega^2 \cdot \frac{\varrho_2}{3} \cdot {r_{\mathrm{2o}}}^2 &= -\mathbf{p_{12}} \\ \frac{\mathbf{C_1}}{r_{\mathrm{2o}}} + \mathbf{p_{12}} &= \omega^2 \cdot \frac{\varrho_2}{3} \cdot {r_{\mathrm{2o}}}^2\end{aligned}$$

Let's assign to K constants the parameters that can be developed independently:

$$\begin{aligned}K_{11} &= \frac{1}{r_{\mathrm{2o}}} \\ G_1 &= \omega^2 \cdot \frac{\varrho_2}{3} \cdot {r_{\mathrm{2o}}}^2\end{aligned}$$

Therefore, the first equation can be written in a compact form:

$$K_{11} \cdot \mathbf{C_1} + \mathbf{p_{12}} = G_1$$

Finally, it is possible to conclude that:

$$\begin{aligned}K_{12} &= 1 \\ K_{13} &= 0 \\ K_{14} &= 0\end{aligned}$$

2nd Equation

$$\begin{aligned}&\sigma_{\mathrm{r2}}\left(r_{\mathrm{2i}}\right) - \sigma_{\mathrm{r3}}\left(r_{\mathrm{3o}}\right) = 0 \\ &\left(\frac{\mathbf{C_1}}{r_{\mathrm{2i}}} - \omega^2 \cdot \frac{\varrho_2}{3} \cdot {r_{\mathrm{2i}}}^2\right) - \\ &\Bigg(-\mathbf{p_{23}} \cdot \frac{r_{\mathrm{3o}}^2}{r_{\mathrm{3o}}^2 - r_{\mathrm{3i}}^2}\left(1 - \left(\frac{r_{\mathrm{3i}}}{r_{\mathrm{3o}}}\right)^2\right) \\ &+ \omega^2 \varrho_3 \frac{3 + \upsilon_3}{8}\left(r_{\mathrm{3o}}^2 + r_{\mathrm{3i}}^2 - \left(\frac{r_{\mathrm{3o}} \cdot r_{\mathrm{3i}}}{r_{\mathrm{3o}}}\right)^2 - {r_{\mathrm{3o}}}^2\right)\Bigg) = 0\end{aligned}$$

The whole parenthesis $\left(r_{\mathrm{3o}}^2 + r_{\mathrm{3i}}^2 - \left(\frac{r_{\mathrm{3o}} \cdot r_{\mathrm{3i}}}{r_{\mathrm{3o}}}\right)^2 - {r_{\mathrm{3o}}}^2\right)$ becomes null.

The product $\frac{r_{\mathrm{3o}}^2}{r_{\mathrm{3o}}^2 - r_{\mathrm{3i}}^2}\left(1 - \left(\frac{r_{\mathrm{3i}}}{r_{\mathrm{3o}}}\right)^2\right)$ is equal to 1. Furthermore, the equation can be simplified as follows:

$$\frac{\mathbf{C_1}}{r_{\mathrm{2i}}} + \mathbf{p_{23}} = \omega^2 \cdot \frac{\varrho_2}{3} \cdot {r_{\mathrm{2i}}}^2$$

Let's assign to K constants the parameters that can be developed independently:

$$K_{21} = \frac{1}{r_{2\mathrm{i}}}$$
$$G_2 = \omega^2 \cdot \frac{\varrho_2}{3} \cdot {r_{2\mathrm{i}}}^2$$

Therefore, the second equation can be written in a compact form:

$$K_{21} \cdot \mathbf{C_1} + K_{24} \cdot \mathbf{p_{23}} = G_2$$

Finally, it is possible to conclude that:

$$K_{22} = 0$$
$$K_{23} = 0$$
$$K_{24} = 1$$

3nd Equation

$$u_1 - u_2\left(r_{2o}\right) = \Delta u_{12}$$
$$\left(\mathbf{p_{12}} \cdot \frac{r_{1,\mathrm{av}}^2}{E_1 \cdot h_1} + \omega^2 \cdot \varrho_1 \cdot \frac{r_{1,\mathrm{av}}^3}{E_1} + r_{1,\mathrm{av}} \cdot \alpha_{\mathrm{th},1} \cdot \Delta T_1\right)$$
$$-\left(\mathbf{C_1} \cdot \frac{1}{E_2} \cdot \ln r_{2\mathrm{o}} + \mathbf{C_2} - \omega^2 \cdot \frac{\varrho_2}{9E_2} \cdot {r_{2\mathrm{o}}}^3 + r_{2\mathrm{o}} \cdot \alpha_{\mathrm{th},2} \cdot \Delta T_2\right) = \Delta u_{12}$$

Let's gather similar pieces of the equation. It is also useful to isolate the unknowns:

$$\mathbf{C_1} \cdot \frac{1}{E_2} \cdot \ln r_{2\mathrm{o}} - \mathbf{p_{12}} \cdot \frac{r_{1,\mathrm{av}}^2}{E_1 \cdot h_1} + \mathbf{C_2}$$
$$= \omega^2 \cdot \varrho_1 \cdot \frac{r_{1,\mathrm{av}}^3}{E_1} + \omega^2 \cdot \frac{\varrho_2}{9E_2} \cdot {r_{2\mathrm{o}}}^3$$
$$+ r_{1,\mathrm{av}} \cdot \alpha_{\mathrm{th},1} \cdot \Delta T_1 - r_{2\mathrm{o}} \cdot \alpha_{\mathrm{th},2} \cdot \Delta T_2 - \Delta u_{12}$$

Let's assign to K constants the parameters that can be developed independently:

$$K_{31} = \frac{1}{E_2} \cdot \ln r_{2\mathrm{o}}$$
$$K_{32} = -\frac{r_{1,\mathrm{av}}^2}{E_1 \cdot h_1}$$
$$G_3 = \omega^2 \cdot \varrho_1 \cdot \frac{r_{1,\mathrm{av}}^3}{E_1} + \omega^2 \cdot \frac{\varrho_2}{9E_2} \cdot {r_{2\mathrm{o}}}^3$$
$$+ r_{1,\mathrm{av}} \cdot \alpha_{\mathrm{th},1} \cdot \Delta T_1 - r_{2\mathrm{o}} \cdot \alpha_{\mathrm{th},2} \cdot \Delta T_2 - \Delta u_{12}$$

Therefore, the third equation can be written in a compact form:

$$K_{31} \cdot \mathbf{C_1} + K_{32} \cdot \mathbf{p_{12}} + \mathbf{C_2} = G_3$$

Finally, it is possible to conclude that:

$$\begin{aligned} K_{33} &= 1 \\ K_{34} &= 0 \end{aligned}$$

4th Equation

$$\begin{aligned}
& u_2\left(r_{2\mathrm{i}}\right) - u_3\left(r_{3\mathrm{o}}\right) = 0 \\
& \left(\mathbf{C_1} \cdot \frac{1}{E_2} \cdot \ln r_{2\mathrm{i}} + \mathbf{C_2} - \omega^2 \cdot \frac{\varrho_2}{9E_2} \cdot {r_{2\mathrm{i}}}^3 + r_{2\mathrm{i}} \cdot \alpha_{\mathrm{th},2} \cdot \Delta T_2\right) \\
& - \Bigg(- \mathbf{p_{23}} \cdot \frac{1}{E_3} \cdot \frac{r_{3\mathrm{o}}^2}{r_{3\mathrm{o}}^2 - r_{3\mathrm{i}}^2} \cdot \left(\left(1 - v_3\right) \cdot r_{3\mathrm{o}} + r_{3\mathrm{i}}^2 \cdot \left(1 + v_3\right) \cdot \frac{1}{r_{3\mathrm{o}}}\right) \\
& + \omega^2 \cdot \frac{\varrho_3}{E_3} \cdot \frac{3 + v_3}{8} \cdot r_{3\mathrm{o}} \\
& \cdot \left(\left(r_{30}^2 + r_{3\mathrm{i}}^2\right)\left(1 - v_3\right) + \left(1 + v_3\right)\left(\frac{r_{3\mathrm{o}} \cdot r_{3\mathrm{i}}}{r_{3\mathrm{o}}}\right)^2 - \frac{1 - v_3^2}{3 + v_3} \cdot {r_{3\mathrm{o}}}^2\right) \\
& + r_{3\mathrm{o}} \cdot \alpha_{\mathrm{th},3} \cdot \Delta T_3 \Bigg) = 0
\end{aligned}$$

Let’s simplify the equation:

$$\begin{aligned}
& \mathbf{C_1} \cdot \frac{1}{E_2} \cdot \ln r_{2\mathrm{i}} + \mathbf{C_2} \\
& + \mathbf{p_{23}} \cdot \frac{1}{E_3} \cdot \frac{r_{3\mathrm{o}}}{r_{3\mathrm{o}}^2 - r_{3\mathrm{i}}^2} \cdot \left(\left(1 - v_3\right) \cdot {r_{3\mathrm{o}}}^2 + \left(1 + v_3\right) \cdot r_{3\mathrm{i}}^2\right) \\
& = \omega^2 \cdot \Bigg(\frac{\varrho_2}{9E_2} \cdot {r_{2\mathrm{i}}}^3 + \frac{\varrho_3}{E_3} \cdot \frac{3 + v_3}{8} \cdot r_{3\mathrm{o}} \\
& \cdot \left(\left(r_{3\mathrm{o}}^2 + r_{3\mathrm{i}}^2\right)\left(1 - v_3\right) + \left(1 + v_3\right) \cdot r_{3\mathrm{i}}^2 - \frac{1 - v_3^2}{3 + v_3} \cdot {r_{3\mathrm{o}}}^2\right)\Bigg) \\
& - r_{2\mathrm{i}} \cdot \alpha_{\mathrm{th},2} \cdot \Delta T_2 + r_{3\mathrm{o}} \cdot \alpha_{\mathrm{th},3} \cdot \Delta T_3
\end{aligned}$$

Let’s assign to K constants the parameters that can be developed independently:

$$\begin{aligned}
K_{41} &= \frac{1}{E_2} \cdot \ln r_{2\mathrm{i}} \\
K_{44} &= \frac{1}{E_3} \cdot \frac{r_{3\mathrm{o}}}{r_{3\mathrm{o}}^2 - r_{3\mathrm{i}}^2} \cdot \left((1 - v_3) \cdot {r_{3\mathrm{o}}}^2 + (1 + v_3) \cdot r_{3\mathrm{i}}^2 \right) \\
G_4 &= \omega^2 \cdot \left(\frac{\varrho_2}{9E_2} \cdot {r_{2\mathrm{i}}}^3 + \frac{\varrho_3}{E_3} \cdot \frac{3 + v_3}{8} \cdot r_{3\mathrm{o}} \right. \\
&\quad \left. \cdot \left(\left(r_{3\mathrm{o}}^2 + r_{3\mathrm{i}}^2 \right) (1 - v_3) + (1 + v_3) \cdot r_{3\mathrm{i}}^2 - \frac{1 - v_3^2}{3 + v_3} \cdot {r_{3\mathrm{o}}}^2 \right) \right) \\
&\quad - r_{2\mathrm{i}} \cdot \alpha_{\mathrm{th},2} \cdot \Delta T_2 + r_{3\mathrm{o}} \cdot \alpha_{\mathrm{th},3} \cdot \Delta T_3
\end{aligned}$$

Therefore, the fourth equation can be written in a compact form:

$$K_{41} \cdot \mathbf{C_1} + \mathbf{C_2} + K_{44} \cdot \mathbf{p_{23}} = G_4$$

Finally, it is possible to conclude that:

$$\begin{aligned}
K_{42} &= 0 \\
K_{43} &= 1
\end{aligned}$$

Full equation in matrix form

$$\begin{bmatrix} K_{11} & 1 & 0 & 0 \\ K_{21} & 0 & 0 & 1 \\ K_{31} & K_{32} & 1 & 0 \\ K_{41} & 0 & 1 & K_{44} \end{bmatrix} \cdot \begin{Bmatrix} C_1 \\ p_{12} \\ C_2 \\ p_{23} \end{Bmatrix} = \begin{Bmatrix} G_1 \\ G_2 \\ G_3 \\ G_4 \end{Bmatrix} \tag{4.2}$$

4.4.2 Boundary Conditions After Lift-Off

After the lift-off it is possible to impose $p_{23} = 0$. Therefore $\sigma_{\mathrm{r}2} \left(r_{3\mathrm{o}} \right) = 0$. The boundary equations become:

$$\begin{aligned}
\sigma_{\mathrm{r}2} \left(r_{2\mathrm{o}} \right) &= -p_{12} \\
\sigma_{\mathrm{r}2} \left(r_{2\mathrm{i}} \right) &= 0 \\
u_1 - u_2 \left(r_{2\mathrm{o}} \right) &= \Delta u_{12} \\
p_{23} &= 0
\end{aligned}$$

The aim is to derive the three unknowns, writing every equation with the form:

$$K_1 \cdot C_1 + K_2 \cdot p_{12} + K_3 \cdot C_2 = G$$

This will allow to write the system of equation in matrix form:

$$\begin{bmatrix} K_{11} & K_{12} & K_{13} \\ K_{21} & K_{22} & K_{23} \\ K_{31} & K_{32} & K_{33} \end{bmatrix} \cdot \begin{Bmatrix} C_1 \\ p_{12} \\ C_2 \end{Bmatrix} = \begin{Bmatrix} G_1 \\ G_2 \\ G_3 \end{Bmatrix} \tag{4.3}$$

1st Equation

The 1st equation remains unchanged from the previous boundary conditions. The elements will be just reported once more:

$$K_{11} = \frac{1}{r_{2\mathrm{o}}}$$
$$G_1 = \omega^2 \cdot \frac{\varrho_2}{3} \cdot {r_{2\mathrm{o}}}^2$$

The 1st equation in a compact form:

$$K_{11} \cdot \mathbf{C_1} + \mathbf{p_{12}} = G_1$$

Finally, it is possible to conclude that:

$$K_{12} = 1$$
$$K_{13} = 0$$

2nd Equation

$$\frac{\mathbf{C_1}}{r_{2\mathrm{i}}} - \omega^2 \cdot \frac{\varrho_2}{3} \cdot {r_{2\mathrm{i}}}^2 = 0$$
$$\frac{\mathbf{C_1}}{r_{2\mathrm{i}}} = \omega^2 \cdot \frac{\varrho_2}{3} \cdot {r_{2\mathrm{i}}}^2$$

Let's assign to K constants the parameters that can be developed independently:

$$K_{21} = \frac{1}{r_{2\mathrm{i}}}$$
$$G_2 = \omega^2 \cdot \frac{\varrho_2}{3} \cdot {r_{2\mathrm{i}}}^2$$

The 2nd equation in a compact form:

$$K_{21} \cdot \mathbf{C_1} = G_2$$

Finally, it is possible to conclude that:

$$K_{22} = 0$$
$$K_{23} = 0$$

3rd Equation

The 3rd equation remains unchanged from the previous boundary conditions. The elements will be just reported once more:

$$
\begin{aligned}
K_{31} &= \frac{1}{E_2} \cdot \ln r_{2\mathrm{o}} \\
K_{32} &= -\frac{r_{1,\mathrm{av}}^2}{E_1 \cdot h_1} \\
G_3 &= \omega^2 \cdot \varrho_1 \cdot \frac{r_{1,\mathrm{av}}^3}{E_1} + \omega^2 \cdot \frac{\varrho_2}{9E_2} \cdot {r_{2\mathrm{o}}}^3 \\
&\quad + r_{1,\mathrm{av}} \cdot \alpha_{\mathrm{th},1} \cdot \Delta T_1 - r_{2\mathrm{o}} \cdot \alpha_{\mathrm{th},2} \cdot \Delta T_2 - \Delta u_{12}
\end{aligned}
$$

Therefore, the third equation can be written in a compact form:

$$K_{31} \cdot \mathbf{C_1} + K_{32} \cdot \mathbf{p_{12}} + \mathbf{C_2} = G_3$$

Finally, it is possible to conclude that:

$$K_{33} = 1$$

Full equation in matrix form

$$
\begin{bmatrix} K_{11} & 1 & 0 \\ K_{21} & 0 & 0 \\ K_{31} & K_{32} & 1 \end{bmatrix} \cdot \begin{Bmatrix} C_1 \\ p_{12} \\ C_2 \end{Bmatrix} = \begin{Bmatrix} G_1 \\ G_2 \\ G_3 \end{Bmatrix} \tag{4.4}
$$

4.4.3 Improvements from the equations form conversion

Thanks to the conversion of the equations in matrix form, the computational time required to perform the evaluation of the unknowns has been is approximately 330 times less than using the Matlab Symbolic Toolbox. This indeed justify the effort of converting the equations. Unfortunately, analyzing the matrices resulted from the conversion trying to make use of matrix operations, there are no evident characteristic to further simplify their structure. This would make even faster the analytical evaluation of the sleeve stress.

Chapter 5

Sleeve Designer Tool

The content of this chapter regards the approach used for the creation of the pre-design tool for the sleeve parameters, making use of the equations described in the previous section. The target is to include in the SyR-e option tab a section to analytically evaluate the thickness of the sleeve and the pre-stress to apply to retain the rotor at a certain speed.

5.1 Sleeve designing plane

As described in the sleeve conditions in section 4.1, one of the conditions to respect for the rotor to be considered structurally retained is that the magnets need to be attached to the back iron and not to lift-off from it. The speed at which the magnet starts to lift-off will be then considered as the maximum speed that the rotor is allowed to reach. To evaluate the lift-off speed, two trends need to be evaluated. The first is related to the stress of the sleeve for a certain thickness as a function of the speed without any pre-stress applied, which is representative of the magnet detaching as soon as the rotor start to spin, increasing the sleeve stress drastically with rising speed. The second trend regards again the stress of the sleeve as a function of the speed, but this time with a certain pre-stress applied. The pre-stress represent a compressive effect that the sleeve has on the PM+pp element. This means that the magnet will remain attached to the rotor inner yoke as long as the centrifugal force does not overcome the prestress applied. The intersection between this two stress trends related to speed determines the speed at which the magnets detach. However, the stress for which the lift-off speed is determined is not necessarily breaking the sleeve, if this is lower than the maximum sleeve tensile strength. If this is the case, there is a region of speeds in which the magnet is detached from the iron but the sleeve is still intact and in a deformation status. Nevertheless, this region is dangerous and will be considered as a not allowed operating condition.

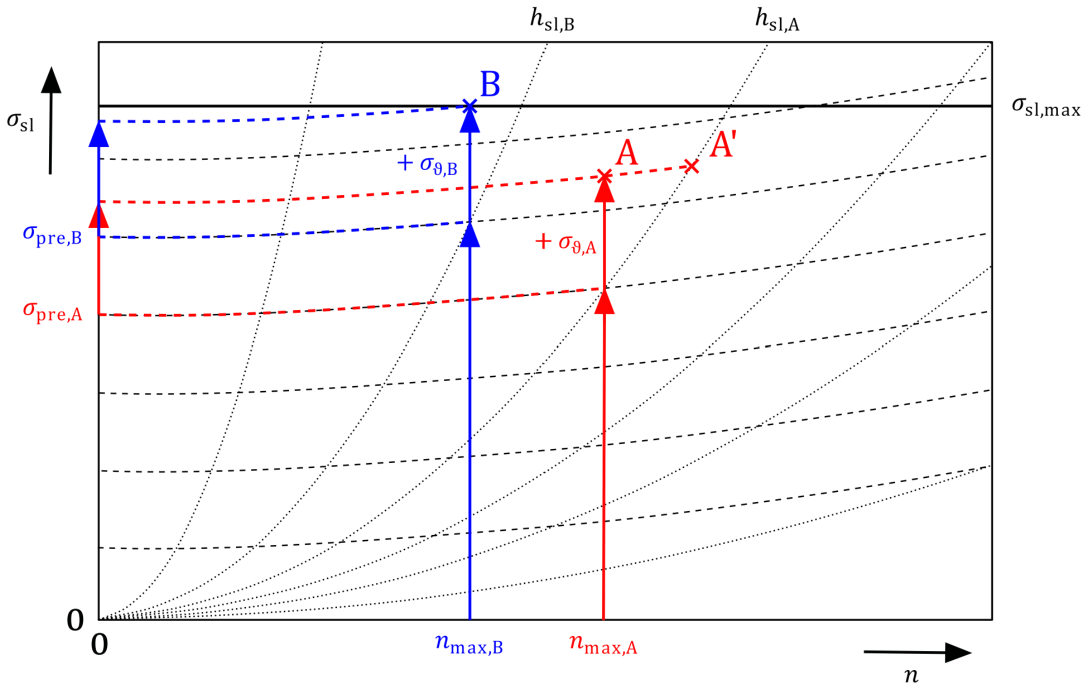

Figure 5.1: (n, σ_{sl}) sleeve design plane. The dotted lines indicate constant sleeve thickness, the dashed lines constant pre-stress. Design A is not optimal, B however gives a minimized sleeve thickness [22]

In Figure 5.1, it is possible to see the concept just described. In this plane though, a set of sleeve thickness values and a set of pre-stress values is reported. Having the two design parameters as vectors allows to design the sleeve for a certain speed just drawing a line starting from a speed value and finding where the constant sleeve thickness curve and the constant pre-stress curve are intersecting. It is straightforward to understand that there are infinite combinations to avoid the magnets to lift off. However, the target is to minimize the sleeve thickness to use a magnetic airgap as small as possible.

5.2 Explicit form of the Sleeve Designer

In order to evaluate the curves described before, it is essential to take as inputs the parameters of the rotor equivalent model described in 4.2. Another essential information is the sleeve yield stress of the sleeve, that will define the upper limit condition of the sleeve stress. One last parameter to define is the worst condition operating temperature of the rotor, that will increase the sleeve stress due to a thermal expansion. In Figure 5.1, this effect is represented by the stress offset labeled as σ_θ. Making use of the equations described in 4.3 and transformed in matrix form in 4.4, the pressure p_{12} acting on the sleeve can be evaluated. Furthermore, the stress on the sleeve, labeled with the index 1 in the equivalent model, can be calculated as follows:

$$s_{t1_{max}} = p_{12} * \frac{r_{1_{av}}}{h_1}$$

Making use of this equation, the two curves described in the previous section can then evaluated as follows:

- Sleeve thickness curves: setting the pre-stress equal to 0, the sleeve stress needs to be evaluated over rising values of speed for different values of sleeve thickness (Figure 5.1).
- Pre-stress curves: for a constant value of sleeve thickness, the sleeve stress is evaluated for rising speed values (Figure 5.1).

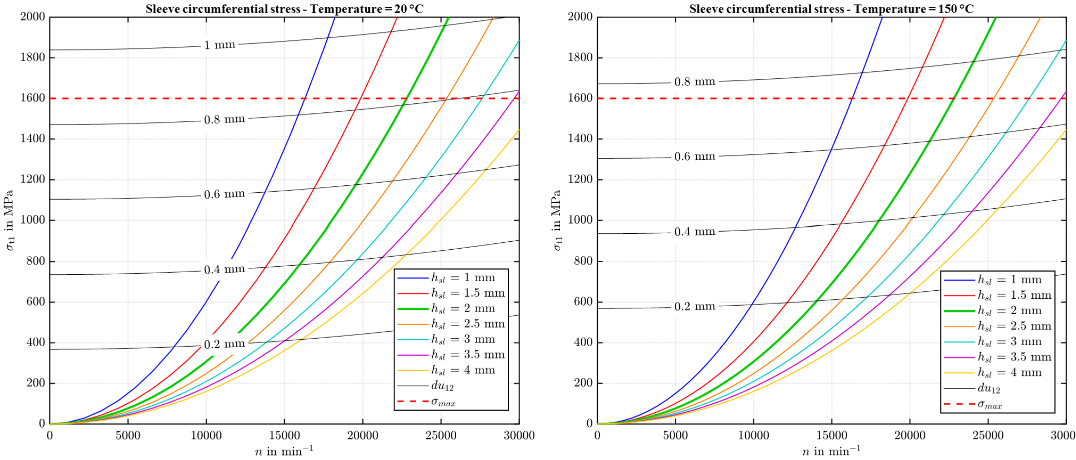

Figure 5.2: Sleeve designer explicit form at 20°C and 150 °C - pre-stress evaluated with a sleeve thickness of 2mm

In Figure 5.2 it is possible to visualize how the stress-speed plane has been implemented in MATLAB. The pre-stress ha been defined as a negative interference (in mm) between the sleeve and the rotor outer radius. The effect of the temperature is to move the pre-stress curves to higher values of sleeve stress. Although this leads to a lower applicable max negative interference before the sleeve breakage, it is clear to see that the temperature is beneficial to the lift-off speed, thanks to the higher compression between the rotor inner core and the sleeve.

This plane gives good indications to obtain the useful parameters to design the sleeve for a determined value of speed trough the analytical model. However, this implementation has a strong limitation, gived by the fact that the pre-stress values are evaluated for a fixed thickness (e.g. in Figure 5.2 they are evaluated for a 2mm sleeve thickness). This means that the intersection between the pre-stress curves and the curves evaluated for different sleeve thicknesses is an approximation. A solution to overcome this problem would be to take advantage of the concept that the maximum speed allowed is the lift-off speed. This means that the the envelope around the intersection point is useful only to understand the behaviour for the speed values different from the maximum speed. For the sake of the pre-design tool then, a plane with the sleeve thickness in the x axis, the pre-stress in the y axis and the lift-off reported as a contour plot dependent on the two values is what could improve the evaluation of the useful parameters.

5.3 Final form of the Sleeve Designer

It has been previously explained that calculating the effect of the negative interference between the sleeve and the outer radius of the rotor using a fixed sleeve thickness is an approximation. In Figure 5.3 it is possible to understand the entity of this approximation, looking at 3 constant sleeve thickness (1 mm, 2 mm and 3 mm) curves and 2 sets of pre-stress applied envelopes, each containing 3 curves evaluated at the three sleeve thickness values.

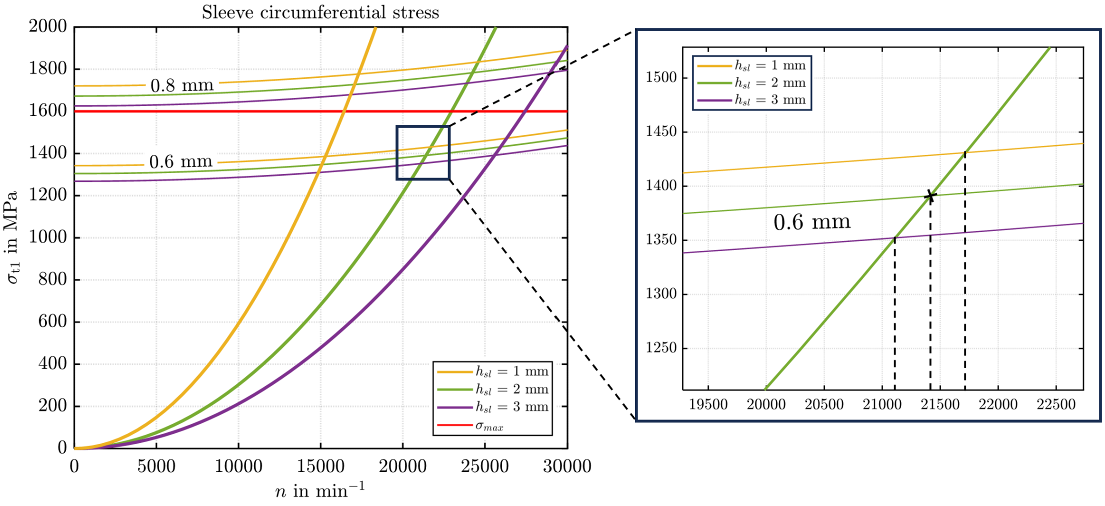

Figure 5.3: Negative interference evaluated for different sleeve values.

As illustrated in the right plot, intersecting a curve with a constant sleeve thickness (e.g., 2 mm) and no pre-stress, with a stress envelope calculated for a different sleeve thickness (e.g., 1 mm), results in extrapolating an incorrect value for the lift-off speed.

To address the approximation of lift-off speed across a set of N sleeve thickness values and M pre-stress values, one approach is to explore N different plots. These plots would consist of a curve with a single sleeve thickness and no pre-stress, along with M curves representing applied pre-stress values evaluated with the N-th sleeve thickness.

However, this process can be cumbersome and time-consuming for evaluating the thickness-pre-stress combination for a specific maximum speed.

The proposed solution aims to consolidate all relevant information into a single plot, without loosing the useful information present in the explicit sleeve design plane. To do so, a new plane has been developed. The lift-off speed is visualized as a contour plot on a sleeve thickness (x-axis) - negative interference (y-axis) plane. This allows for the selection of various thickness-interference combinations to achieve a desired lift-off speed. The objective is to minimize the sleeve thickness and consequently the magnetic airgap, creating the most power-dense rotor design capable of reaching a specific maximum speed.

To attain this goal, it is crucial to understand and document the necessary constraints that limit the design selection.

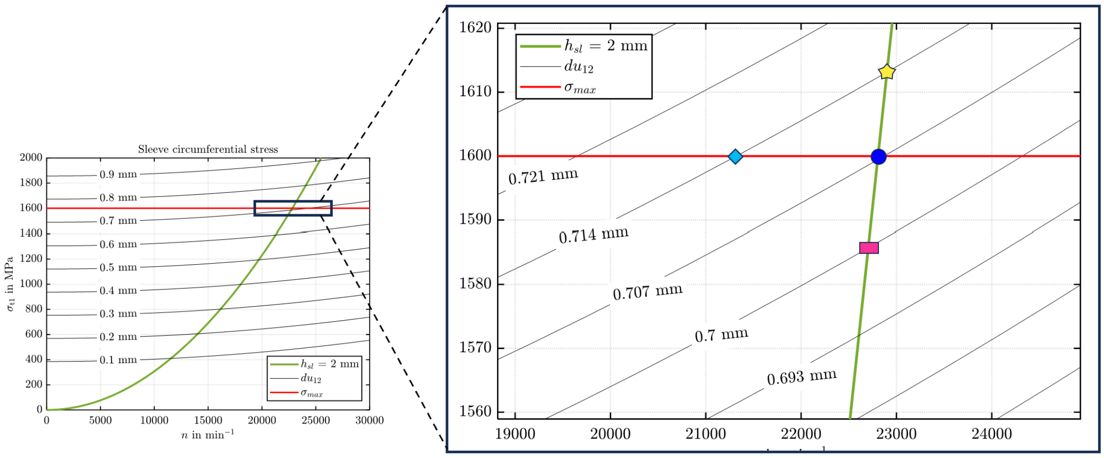

Figure 5.4: Various points of interest in the explicit sleeve design plane with stress curves evaluated with a 2 mm sleeve thickness. ■ Unoptimal lift-off speed point. ● Optimal lift-off speed point. ◆ Unoptimal pre-stress point. ☆ Lift-off point laying above the max stress of the sleeve.

In Figure 5.4, the zoom on the right plot reveals four distinct points that merit description on an explicit sleeve design plane, with stress curves evaluated at a constant sleeve thickness.

The description commences with point ▬, situated at the intersection of the constant no pre-stress curve and the stress curve with a pre-stress of 0.7 mm negative interference. By projecting a vertical line onto the x-axis, the lift-off speed for the design with that specific thickness-interference combination can be evaluated. However, it is evident that the point does not lie on the sleeve's maximum stress (σ_{max}) line. Considering the lift-off speed as the maximum speed (due to the magnets not detaching from the rotor back iron), it indicates that the sleeve is not pushed to its breaking limit at the rotor's maximum speed. Therefore, these sleeve parameters can be deemed sub-optimal, and an alternative combination could potentially result in a higher maximum speed, as observed in the case of point ●. The projection in this instance would yield a higher speed than before, harnessing the full capabilities of the sleeve by applying a greater sleeve interference of 0.707 mm.

Conversely, point ◆ illustrates a condition where an even higher negative interference (0.714 mm) would cause the stress envelope to intersect the maximum stress value at a considerably lower speed. This lower speed should be considered as the maximum speed of the rotor, as opposed to the intersection with the no pre-stress curve (point ☆), which lies above the sleeve's maximum stress.

Every information can be easily evaluated at a specific temperature (in this case 150 °C) in the final form of the Sleeve Designer in Figure 5.5 for every preferable set of sleeve thickness values (in this case a vector between 0.5 mm and 5 mm) and negative interference (in this case a vector between 0 mm and 1 mm).

Comparing this plain and the one in Figure 5.4, every point laying on a contour on the white background area can be described as the point ▬. The every plot laying on the intersection between a contour plot and the border line between the white background area and the Danger Area can be considered as an optimal point similar to ●. Every point on a contour belonging to the Danger Area is a lift off speed evaluated for a combination of thickness - interference that intersect above the maximum stress of the sleeve, as represented with the point ☆). Finally, The Breakage Area represent every contour plot evaluated for an applied negative interference that would cause a stress exceeding the maximum sleeve stress at 0 rpm. The point ◆ is not represented in any way from this plane because it would make the contour plot look chaotic without adding any useful information, because suboptimal.

It is possible to conclude that the final form of Sleeve Designer contain all the essential set of information to design the sleeve maximizing the motor performance. In the actual implementation of the Sleeve Designer an additional safety factor of

20 % has been applied. This means that the maximum speed that on the contour lines is 20 % lower than the speed that the motor could reach theoretically. This conservative approach allows to neglect every possible error that analytical model can induce in the design.

Regarding the effect of the temperature, it is important to underline that the contour lines and the two limit areas have two different behaviours. To consider a proper stress scenario for a set of speed values, the contour plot has to be evaluated at a ambient temperature. The reason behind that has to be attributed to the negative interference value, which is defined as a difference between the inner radius of the sleeve and the outer radius of the radius when they are both at ambient temperature. On the other hand, limit of the Danger Area and the Breakage Area are temperature dependent. The higher temperature, the lower the maximum applicable interference will be.

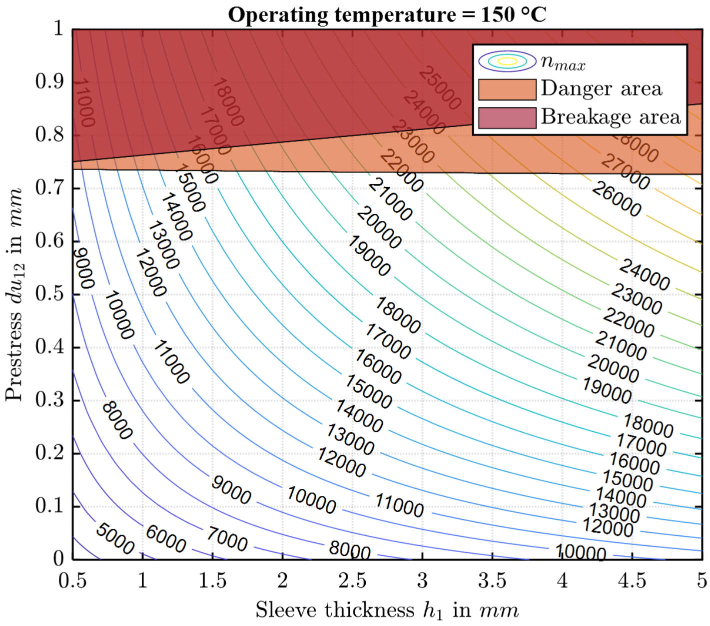

Figure 5.5: Final form of the sleeve designer

To sum up, to make use properly of the final Sleeve Designer tool, a user should apply the following workflow:

1. Provide the geometry parameters, including the max stress of the sleeve, and the operating temperature as input
2. Define the vectors of sleeve thickness and negative interference to investigate

3. Plot the Sleeve Designer trough a dedicated button in SyR-e
4. Chose a maximum speed to design the motor for and find the intersection between its relative contour on the plane and the Danger Area border line
5. Derive the combination of sleeve thickness and negative interference to apply to design a motor that can go up to the desired maximum speed

Chapter 6

Sleeve Motor Design

6.1 Methodology for the analysis

The analytic sleeve pre-design tool described in 5.3 has been exploited in this chapter to design motors for three target speeds: 14, 18 and 21 krpm. Adopting the Model S Plaid motor (Figure 6.1 as a baseline, all the parameters used for the following study will refer to this particular geometry.

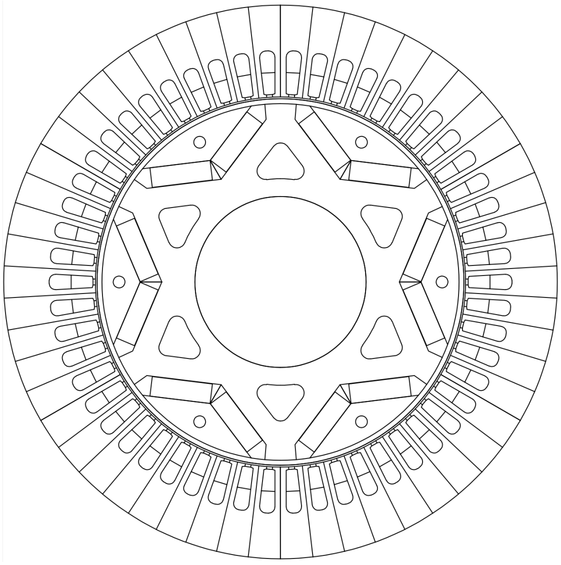

Figure 6.1: Model S Model full geometry

Among the parameters reported in Table 6.1, the only parameter that will be investigated for the three different speeds is the sleeve thickness. To perform a fair analysis, maintaining the independent parameters constant for all the geometries is

Table 6.1: Baseline sleeve motor - Tesla Model S Plaid parameters

Main Motor Parameters		Stator Parameters	
Number of pole pairs	3	Tooth length [mm]	18.85
Number of 3-phase sets	1	Tooth width [mm]	4.35
Number of slots/(pole*phase)	3	Yoke length [mm]	18.45
Number of stator slots	54	Slot width [mm]	4.6
Airgap thickness [mm]	0.7	Slot shape	Trapezoidal
Stator outer radius [mm]	112.5	Stator slot opening [p.u.]	0.275
Airgap radius [mm]	74.5	Tooth tang. depth [mm]	1
Shaft radius [mm]	34.75	Tooth tang. angle [°]	15
Stack length [mm]	134	Fillet at slot bottom [mm]	2.5
Material Data		**Rotor Parameters**	
Stator core material	M270-35A	Barriers angles alpha [°]	21
Stator slot material	Copper	Barriers width [mm]	8.36
Rotor core material	M270-35A	Tangential ribs width [mm]	-
Magnet material	BMN-52UH	Tangential ribs fillet in [mm]	-
Shaft material	Air	Tangential ribs fillet out [mm]	-
Sleeve material	DW325	Radial ribs width [mm]	-
Total motor mass	32.7454	Radial ribs fillet in [mm]	-
Rotor inertia	0.92394	Radial ribs fillet out [mm]	-
		Magnet width [mm]	24.6

essential. Parameters that are dependent on the sleeve have been readjusted in order to keep as much as possible the geometry main characteristics unchanged (e.g. in SyR-e, the central barrier offset has been modified to make the geometry feasible for higher values of sleeve and to keep the same V-Shape angle). To find the combination of sleeve thickness and pre-stress, the Sleeve Designer plane has been used considering a rotor temperature of 150 °C. This is a very conservative assumption, considering that such temperature is very dangerous for PM motors due to the demagnetization effect of the magnets, related to the decrease of the coercive field with the temperature increase in NdFeB magnets. Also other problems can be caused by the operation at such temperature, like the acceleration of the degradation of the insulators over time. A well design rotor should never operate at that temperature.

6.2 14krpm candidate

Generating the Sleeve Designer plane using the parameters of the Model S Plaid motor, the selection of a candidate for a certain speed results quite easy. In Figure 6.2, the right figure represent the Sleeve Design plane and the data tip window that shows how the candidate for 14krpm has been selected. Following the 14krpm contour line up to reach the minimum sleeve thickness size that do not enter the Danger area, the Sleeve Designer suggests to assign a sleeve thickness of 1.1 mm, applying a negative interference between the sleeve and the rotor of 0.735 mm.

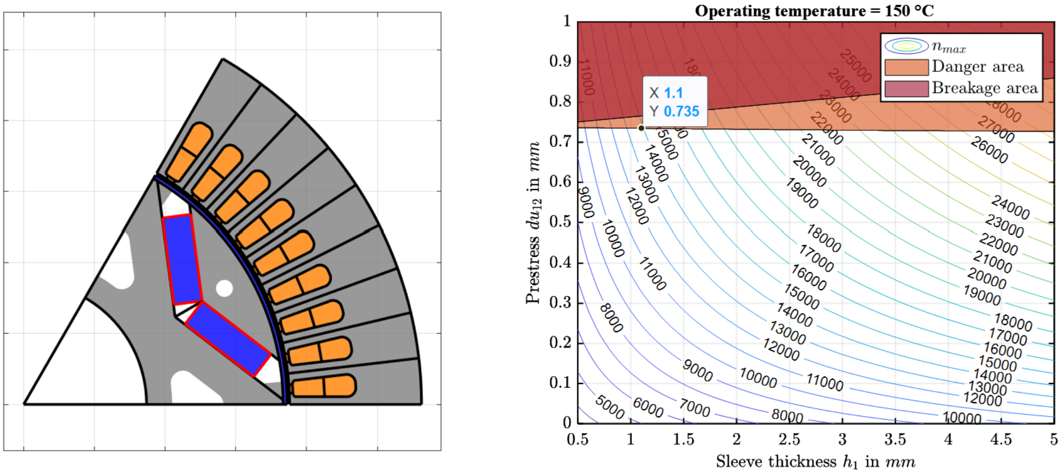

Figure 6.2: Sleeve 14krpm Design

6.3 18krpm

Following the same approach used to design the 14 krpm geometry, a new motor for a maximum speed of 18 krpm wants to be designed.

The same Sleeve Designer plane, evaluated with the Tesla Model S Plaid Parameters, will be used again. The intersection between the 18 krpm contour line and the border line of the Danger Area gives as a result the two values of sleeve thickness and negative interference, respectively 1.9 mm and 0.731 mm, to design the motor with the minimum magnetic airgap for the selected maximum speed. In Figure 6.3, on the left side is possible to visualize the geometry designed with the Sleeve Designer plane (with the data tip of this specific selection) on the right side.

6.4 21krpm

One last time, the same Sleeve Designer plane will be used, to design a motor able to reach a maximum speed of 21 kprm.

For this specific speed, the optimal parameters are 2.6 mm for the sleeve thickness and 0.731 mm for the negative interference. In Figure 6.4, the design is reported

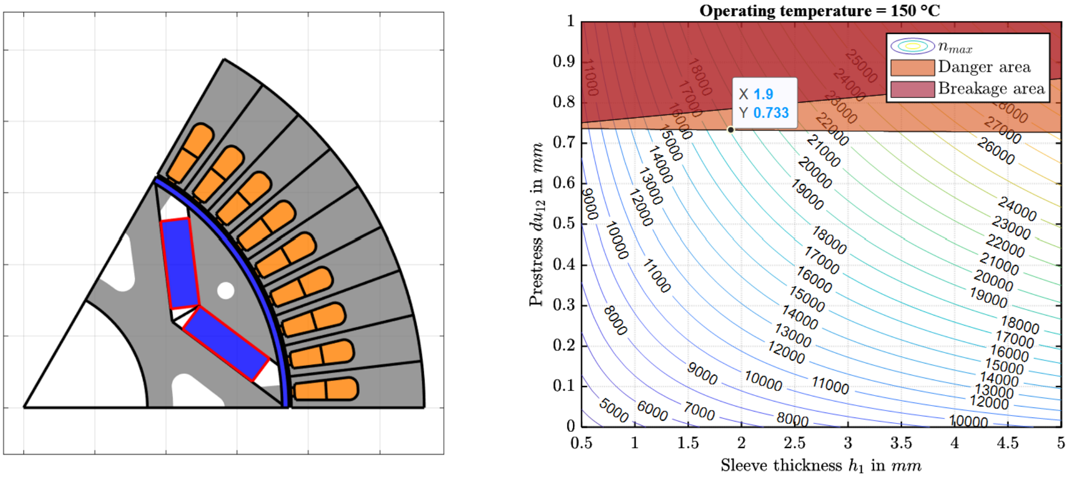

Figure 6.3: Sleeve 18krpm Design

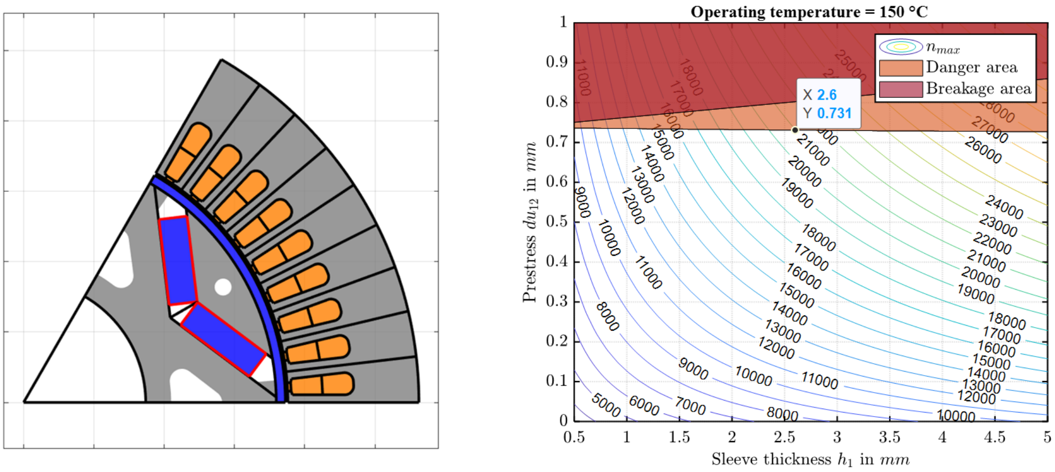

Figure 6.4: Sleeve 21krpm Design

on the left and the related Sleeve Designer plane with the data tip selection shown on the right.

Chapter 7

Ribs Motor Design

7.1 Methodology for the analysis

In this chapter, the IPM V-Type motor designed by Tesla for the Model 3 is taken as a baseline and redesigned at the same three different speeds used to design the wrapped motors in the previous chapter (14krpm, 18krpm and 21krpm). In order to achieve this target, it is useful to understand what are the main parameters affecting the mechanical structure of this type of motor. The parameters of interest for this analysis are in fact concerning two main retaining features of the motor: the radial rib and the tangential rib (previously also called as bridge). Both this two parts have three main control parameters: the width [mm], the fillet in [mm] and the fillet out [mm] (that are the radius of the corners of the flux barrier). By changing these 6 parameters iteratively, the aim is to converge to a geometry for each of the three speeds of interest, ensuring that the Von Mises stress in every part of the rotor does not exceed the max stress limit of 450 MPa, characteristic of the M270-35A rotor core material.
In order to perform the structural simulations of the rotor geometries, the PDE Tool of MATLAB implemented in SyR-e will be adopted trough the Simulation tab of SyR-e. In order to make use of more realistic rotors compared to the geometry parameterized in SyR-e, the custom FEMM geometries have been imported. To change the features dimensions, every geometry has been exported in DXF format, imported to AutoCAD, customized and re-imported to FEMM.

7.2 Ribs Baseline - Model 3

As already cited before, the Model 3 motor developed by Tesla (Figure 7.1) has been used as the baseline for this analysis. This IPM V-Shape geometry present not only the standard elements of the common geometry of its genre, but also some particular features that will be included in the analysis, such as mass reduction holes and different dents at the outer rotor radius.

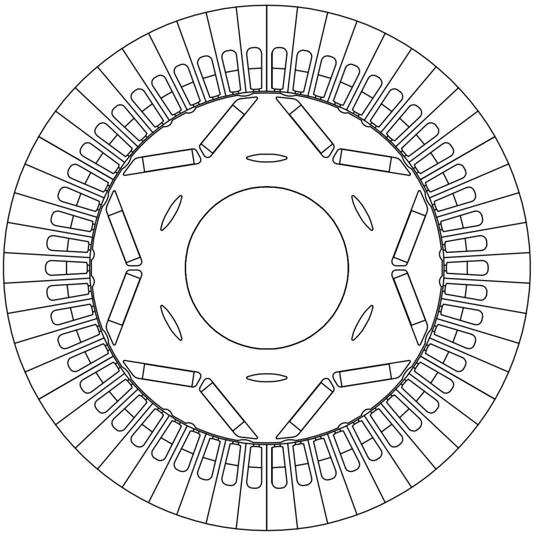

Figure 7.1: Tesla Model 3 full geometry model, available in SyR-e

Main Motor Parameters		Stator Parameters	
Number of pole pairs	3	Tooth length [mm]	18.85
Number of 3-phase sets	1	Tooth width [mm]	4.35
Number of slots/(pole*phase)	3	Yoke length [mm]	18
Number of stator slots	54	Slot width [mm]	4.6
Airgap thickness [mm]	0.7	Slot shape	Trapezoidal
Stator outer radius [mm]	112.5	Stator slot opening [p.u.]	0.275
Airgap radius [mm]	74.95	Tooth tang. depth [mm]	1
Shaft radius [mm]	34.75	Tooth tang. angle [°]	15
Stack length [mm]	134	Fillet at slot bottom [mm]	2.5
Material Data		**Rotor Parameters**	
Stator core material	M270-35A	Barriers angles alpha [°]	23.7
Stator slot material	Copper	Barriers width [mm]	6.6
Rotor core material	M270-35A	Tangential ribs width [mm]	1.65
Magnet material	BMN-52UH	Tangential ribs fillet in [mm]	0.48
Shaft material	Air	Tangential ribs fillet out [mm]	3.46
Sleeve material	-	Radial ribs width [mm]	1.85
Total motor mass	34.8848	Radial ribs fillet in [mm]	1.8
Rotor inertia	0.039168	Radial ribs fillet out [mm]	1.47
		Magnet width [mm]	21.5

Table 7.1: Baseline Ribs motor - Tesla Model 3 parameters

In Table 7.1, the main parameters of the Model 3 motor have been reported. In the following sections, where new rotor will be generated for the three different target speeds previously reported, every parameter of the machine will be kept constant, except for rotor the rotor parameters regarding the radial and tangential ribs. An important assumpion is to keep constant the magnets size, to have a fair comparison between different speeds in term of Von Mises stress and, subsequentially, in performance.

7.3 14krpm design structural analysis

The Model 3 baseline model already present in SyR-e has maximum structural speed of 14 krpm. Thus, the research of the optimal candidate for this speed didn't ask any additional ribs parameters variations.

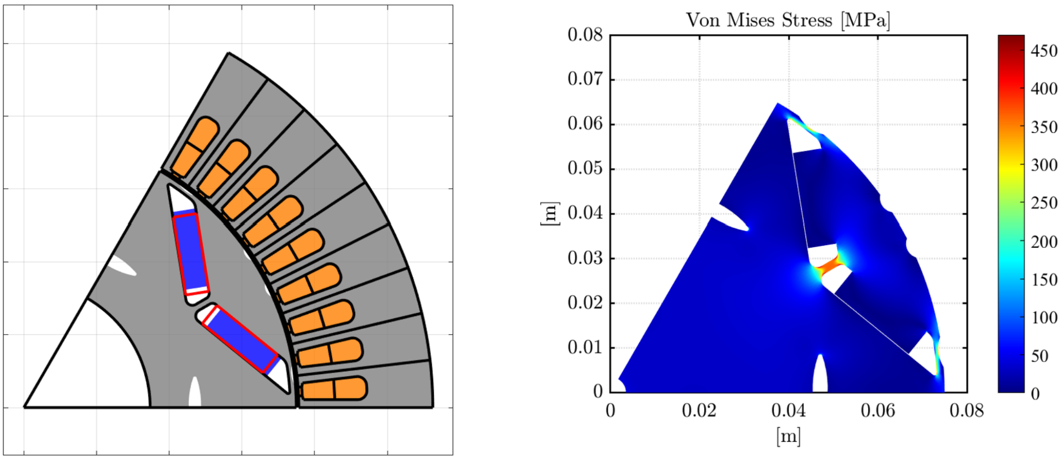

Figure 7.2: Ribs Motor - 14krpm Design

Therefore, the radial and tangential ribs values that are necessary to retain structurally this motor at 14krpm are:

$$\text{Radial rib width} = 1.85\text{mm}$$

$$\text{Tangential rib width} = 1.65\text{mm}$$

In the colorbar on the Von Mises Stress plot in Figure 7.2, it is possible to notice that there are some parts of the motor crossing slightly the 450 MPa limit. However it is a marginal acceptable condition, but it is important to ensure that this points are laying only in the tangential ribs junctions. Effectively, this over stressed areas are not as much problematic for maximum speed analysis as for fatigue analysis, that is related to the stress of the rotor over several cycles of operation. A small margin of limit cross will be then considered acceptable in this areas.

7.4 18krpm design structural analysis

Starting from the Model 3 baseline, the 18krpm candidate required 18 iterations before converging to a solution able to satisfy the condition of a max stress lower than 450 MPa.

	Radial Rib			Tangential Ribs		
Iteration	Width [mm]	Fillet In [mm]	Fillet Out [mm]	Width [mm]	Fillet In [mm]	Fillet Out [mm]
0	1.85	1.8	1.47	1.65	0.48	3.46
1	**2.5**	1.8	1.47	1.65	0.48	3.46
2	**3**	1.8	1.47	1.65	0.48	3.46
3	3	1.8	**2**	1.65	0.48	3.46
4	3	**2.3**	2	1.65	0.48	3.46
5	3	2.3	**2.5**	1.65	0.48	3.46
6	**3.2**	2.3	2.5	1.65	0.48	3.46
7	3.2	**2.7**	2.5	1.65	0.48	3.46
8	3.2	2.7	**2.8**	1.65	0.48	3.46
9	3.2	2.7	2.8	1.65	**1**	3.46
10	3.2	2.7	2.8	1.65	**1.5**	3.46
11	3.2	2.7	2.8	1.65	1.5	**2.5**
12	3.2	2.7	2.8	**2**	1.5	2.5
13	3.2	2.7	2.8	2	**2**	2.5
14	3.2	2.7	2.8	2	2	**2**
15	3.2	2.7	2.8	**2.3**	2	2.5
16	3.2	2.7	2.8	2.3	2	**1.2**
17	3.2	2.7	2.8	2.3	**2.5**	1.2
18	3.2	2.7	2.8	2.3	2.5	**2**

Table 7.2: Iterations to converge to a 18krpm geometry with an acceptable max Von Mises stress. In green, dimension increase. In red, dimension decrease

In Figure 7.2, all the iterations are reported. As can be noticed, the approach adapted was to change one parameter per iteration, analyzing for each of them the maximum stress of the new geometry generated trough structural analysis. The choice of the parameter to vary has been based on where the maximum stressed point was laying. For example, if it was at the center of the rib, the rib width was changed consequentially, with an increase that would have probably relaxed the stress in that point. On the other hand, if the max stress point was laying closer to one of the two fillets, the radius of that specific junction was increased.

The procedure just elucidated led to the geometry in Figure 7.3, with the two rib parameters being equal to:

$$\text{Radial rib width} = 3.2\text{mm}$$

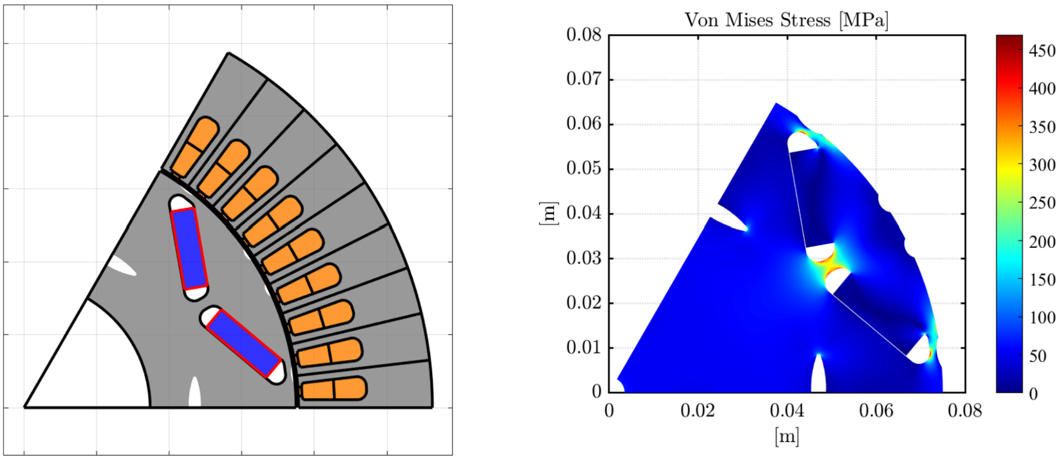

Figure 7.3: Ribs Motor - 18krpm Design

Tangential rib width = 2.3mm

This iterative process for structural analysis conversion is very time consuming, considering that every feature modification has been done manually. Several advanced motor design software make use of Multi-Objective optimization to perform this process automatically, assigning boundaries to the ribs dimensions and setting as objective function the minimization of the flux leakage.

7.5 21krpm design structural analysis

Following the same approach explained in the previos section, the 21krpm ribs motor has been structurally optimized requiring fewer iterations. Starting from the 18krpm geometry, the structural analysis converged mainly changing the width of the radial and tangential ribs. This means that after a certain speed, there is not further need of changing drastically the fillets dimensions, while the width of the ribs is playing a more predominant role. The iterations for the convergence will not be reported again, because the idea behind the process is already clear looking to Table 7.2.

Finally, in Figure 7.4 is reported the geometry optimized for 21krpm, that has the two ribs parameters equal to:

Radial rib width = 4.6mm

Tangential rib width = 3.8mm

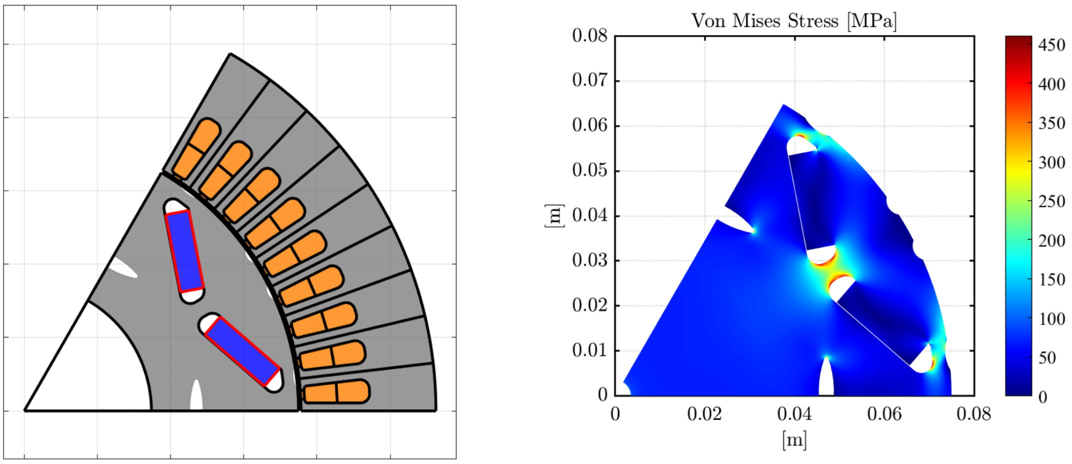

Figure 7.4: Ribs Motor - 21krpm Design

7.6 Considerations on the ribs motor structural analysis

During the analysis of the ribs motor, taking as example the real geometry of the Tesla Model 3 motor, various details have been investigated to improve the stress analysis as much as possible. This reverse-engineering process leaded to take in consideration three main features end their effect on the rotor mechanical integrity: the magnet holders inside the rotor barriers, the dents at the outer rotor radius and the mass reduction holes.

7.6.1 Magnets holders

This features, highlighted in Figure 7.5, are added in the magnets slots to avoid the magnets to move due to centrifugal force. However, there is a chance that this holders are also helping to relax the stress in the ribs, making use of the propriety of the magnet to sustain some compressing pressure.

To test the effect of the holders, they have been added in the custom geometry trough AutoCAD and, subsequently, imported in the FEMM custom geometry. This allowed to use the Matlab PDE tool to make a structural simulation including the holders trough SyR-e.

The test for the benefit of the holders have been performed when trying to optimize the ribs geometry for 14krpm. Unfortunately, the implementation of this feature has revealed two main problems that are clearly visible in Figure 7.6. The first regards the steep corner between the holder and the side of the barrier. In this

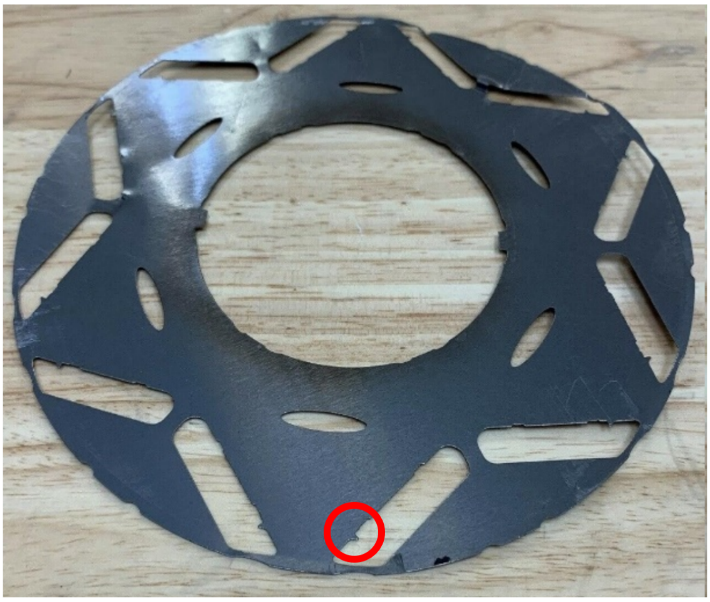

Figure 7.5: Model 3 Lamination - Magnet holder [24]

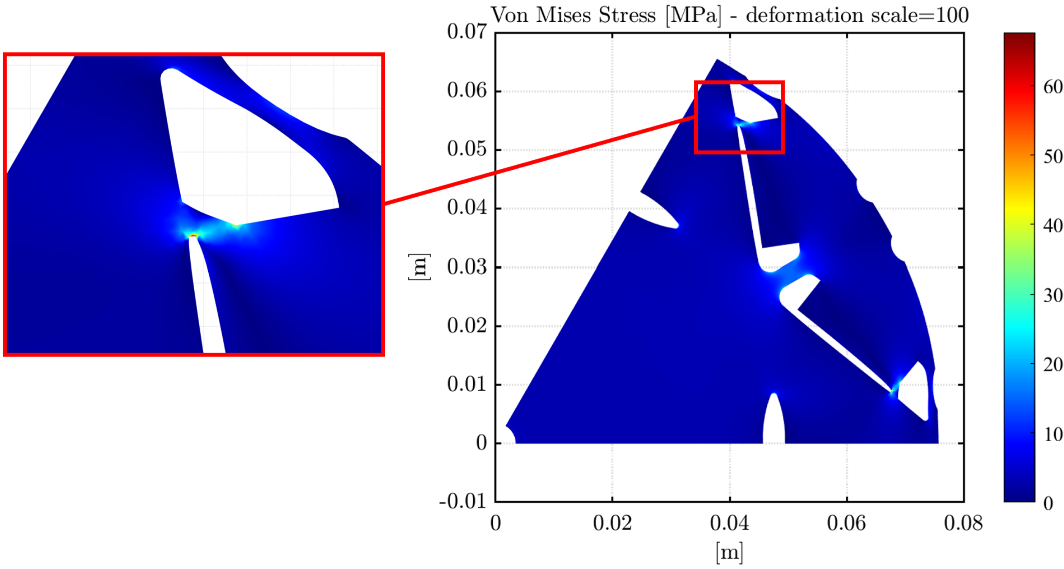

Figure 7.6: Von Mises Stress plot with deformation scale = 100 at 14rpm of a geometry with magnet holders

region, the mesh is problematic and the stress appears to be out of scale compared to what should be in the reality. The second problem has to deal with the PDE tool, that is only able to create a single body for the structural analysis. From the deformation at 100 scale, it is clear to see that the magnet remains attached to the holder as it is part of it. In a realistic model, the magnet should be separated with an air gap from all the elements of the rotor iron. This would allow to simulate a motion of the magnet inside the pocket and to visualize the effect of the holder on the stress. This limitation can't be overcome using the PDE tool that SyR-e is adopting.

7.6.2 Effect of the mass reduction holes

During the optimization of the 18krpm motor with ribs, the problematic of relaxing the stress on the tangential ribs brought to investigating on the effect of the mass reduction holes on the structure of the rotor at high speed. These features are there most probably to reduce the inertia of the rotor to have a better dynamic behaviour. Another usage of those holes could be to have channels for cooling the rotor with air or flowing oil. But it would be interesting to understand if they are also useful to rleax the stress in the rotor ribs. In order to do this, three different geometry have been analyzed. Starting from the ribs parameters reported for the iteration 14 in Table 7.2, a geometry without holes, one with the standard Model 3 holes and a final one with the holes designed for the Model S Plaid rotor have been structurally simulated trough SyR-e.

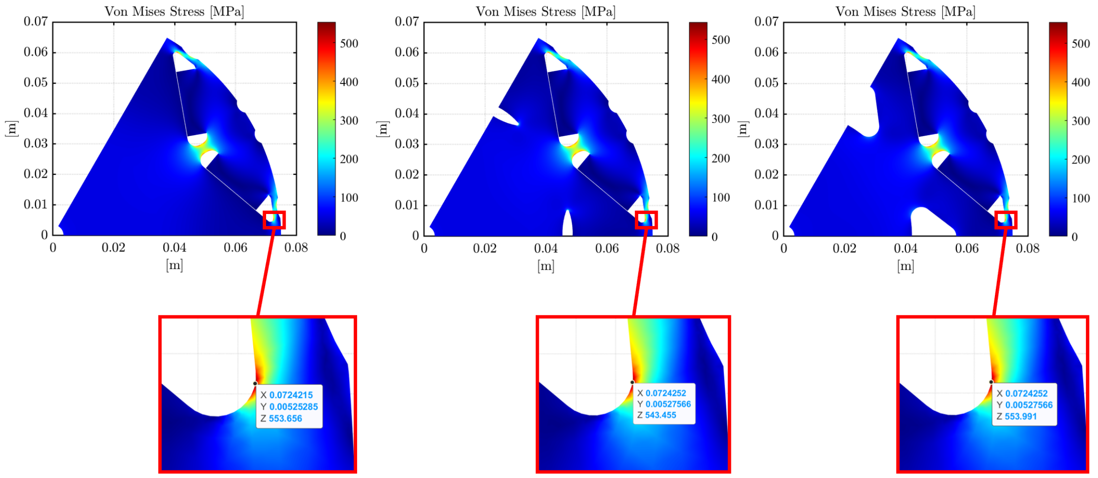

Figure 7.7: From left to right: no mass reduction hole, normal mass reduction hole, bigger mass reduction hole - 18krpm structural analysis.

In Figure 7.7 the results of the analysis are reported. Looking at the most stressed point for the three geometries, that is the junction of the barrier with the bridge, there is not a clear trend with the reduction of mass in the core. What can be deduced is that the holes are not playing a significant role on relieving stress from the bridges.

Chapter 8

Sleeve vs. Ribs motors comparison

In this final section, a comparative analysis will be conducted between the sleeve motors designed in Chapter 6 and the rib motors designed in Chapter 7. The target is to determine whether the sleeve motors, which pose higher construction challenges, exhibit significantly better performance and efficiency than the rib motors across the three speeds for which they have been designed. In order to compare the two technologies, the same system parameters are settled and most of the geometrical parameters that can be commonized, need to be equal. To extract the useful information, a set of simulations have been performed, allowing to collect curves and maps related to the motors behaviours over certain conditions of temperature, operation and control. For every maximum speed, the two technologies will be analyzed side by side, in order to have a direct comparison and visualize all the differences that are playing a role in the characterization of each motor.

8.1 Considerations on the geometrical parameters adopted for the comparison

To have a fair comparison between the two motor technologies, the geometrical parameters that are playing a major role in power and torque production need to be equal. This is the case for the motors designed in Chapter 6 and 7 for the two technologies. Summarizing:

- The stators exhibit uniformity in terms of dimensions, materials, pole count, windings, and electrical rating. This consistency is particularly justified by the shared cooling system and inverter.

- It is plausible that the selection of materials in the rotor aligns with similarity. The exclusive feature distinguishing the Model S Plaid rotor is the CF-wrapping.
- Both the inner and outer radii of the rotors are identical, and they share a common principal PM arrangement characterized by a V-shaped flux barrier. The mechanical air gap of both rotors to the stator's inner surface is equal to 0.7 mm.

The main difference between the two rotor geometries is related to the magnet size. The absence of the ribs in the sleeved motor allows to fit more magnet compared to the standard IPM V-Shape geometry. For the three different speed analyzed, one main constraint in the structural analysis was to keep the magnet size constant, which in the sleeve motor is 42.6 % higher than the ribs motor.

8.2 Considerations on the system parameters adopted for the comparison

In order to evaluate performance and efficiency and compare them between two motors, it is essential to adopt the same system parameters, as they would be implemented in the same powertrain. The assumption then is to use the same battery and the same inverter to supply the motor. Regarding the battery, for this analysis it will only useful to impose the same DC link voltage. Nowadays, most of the electric car manufacturer are making use of batteries with a DC Voltage of around 400 V at 100 SoC (State of Charge). This is the case also for the Model 3 and Model S Plaid platforms developed by Tesla. However, the Model 3 Baseline motor available in SyR-e, of which the stator has been taken as a starting point for every motor designed in Chapter 6 and Chapter 7, is designed for a DC Link of 230 V. In order to adapt the motors for a higher voltage, it is necessary to redesign the stator windings. The logic behind the rewinding of this machines is to change the back EMF (Electro-Magnetic Force, measured in V) accordingly to the DC Link voltage, applying the Faraday's law for windings:

$$E = N_t \cdot \frac{dlambda_B}{dt}$$

Since the rotor will remain unchanged, the component of variation of magnetic flux over time $\frac{d\lambda_B}{dt}$ at every speed will remain the unvaried. Hence, the number of turns in series per phase N_s has to be linearly re-scaled based on the voltage ratio between the old DC Link and the new one:

$$N_{s_{[400V]}} = N_{s_{[230V]}} \cdot \frac{400V}{230V}$$

One main advantage of increasing the DC Link voltage and rewind the machine is to supply the motor with the same power, decreasing the nominal current. This play a big role on the inverter size, that is typically reduced for a lower nominal current. Also the efficiency could benefit from a lower current level, thanks to lower Joule losses:

$$P_{J_{avg}} = R_{AC} \cdot I_{rms}^2$$

However, the slot size of the stator has been kept constant in the voltage conversion. This means that to increase the number of turns, the conductor size needs to be decreased and the resistance is consequently increased. Also the slot fill factor has been kept constant, even if the insulation thickness may be higher for the 400V winding, demanding for more space in the slot for insulating material.

All this considerations led to designing the a new winding making use of the Winding tab in SyR-e In Figure 8.1 it is possible to visualize the winding re-designing, with the old 230 V slot model on the left and the 400 V on the right.

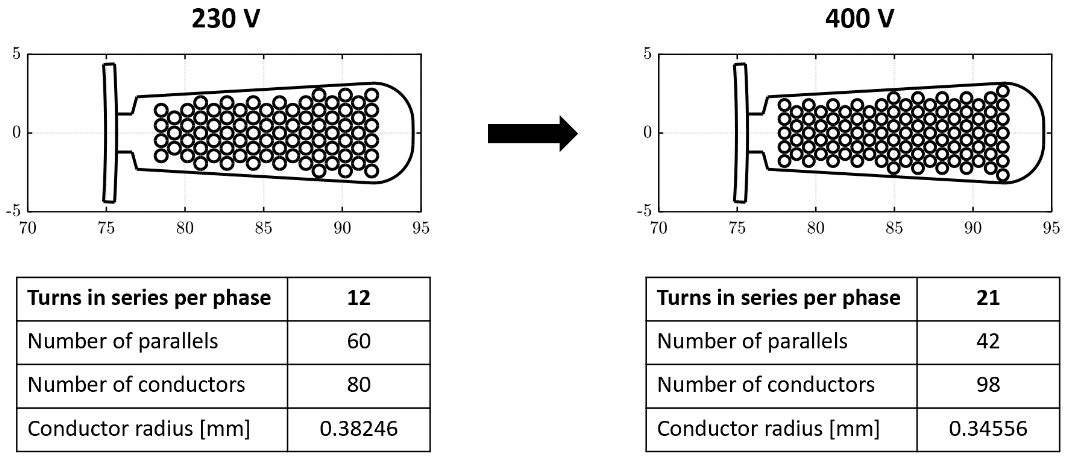

Turns in series per phase	12
Number of parallels	60
Number of conductors	80
Conductor radius [mm]	0.38246

Turns in series per phase	21
Number of parallels	42
Number of conductors	98
Conductor radius [mm]	0.34556

Figure 8.1: Slot model - winding re-design from 230 V to 400 V DC Link

Apart from the inverter, another limit for the current comes from the thermal limits of the motor. In order to be consistent with the thermal capacity of the Model 3 Baseline motor, the RMS current density J_s $[A \cdot mm^2]$ in the slot has been kept constant. With the new winding, the rated current for the motors passed from rated phase current amplitude $\hat{I}_{s,ph,N} = 1403A$ to $\hat{I}_{s,ph,N} = 803A$.

8.2.1 Simulations performed for the comparison

The majority of the simulation outcomes that will be presented are derived from generating motor flux maps, as detailed. Torque (T) and flux linkages (λ_d, λ_q) are computed over both d and q current, providing an intricate magnetic model of the machine and enabling insights into its performance through thorough postprocessing. The flux map simulations in this study were executed with the following configurations:

- A single machine pole with $Q_s/(2p) = 9$ stator slots was chosen for the simulation to capitalize on the motor's symmetry, thereby reducing simulation time.
- The rotor angular excursion was limited to 60° (electrical) instead of the full 360° to further leverage symmetries and expedite simulation time. A 180° excursion was necessary for the iron loss flux maps. In both scenarios, 30 rotor positions were assessed.
- The axis convention was established as PM, aligning λ_{PM} along the positive d axis.
- The number of simulated current quadrants was set to 2, with $i_q \geq 0$ and $i_d \leq 0$. For each half-axis, 15 current points were computed, resulting in 15 i_q and 29 i_d levels for both standard flux map and iron-loss flux map simulations.
- The RMS current density was $J_s = 36\,\mathrm{A/mm^2}$, targeting short-time peak conditions, and the rated phase current amplitude ($I_{\mathrm{s,ph,N}}$) was approximately 803 A, slightly below the inverter current limit. The DC link voltage was selected as $V_{\mathrm{DC}} = 400\,\mathrm{V}$.
- The PM temperature was set to $\theta_{\mathrm{PM}} = 20°\mathrm{C}$. The winding temperature (θ_{Cu}) was set to 100°C. However, even this parameters are not representative of the average operation of the motors, they are functional for the sake of the comparison.

Exactly the same configuration has been applied for the Iron Loss - Flux maps evaluation.

With the slot model evaluation, the results regarding the skin effect for the AC Loss model are extracted, including in the Loss Maps the contribute related to the AC conductor resistance. The evaluation has been performed in the process of redesigning the new slot model for the 400 V DC Link.

Additional simulations conducted using SyR-e involve the computation of the air gap flux density distribution under no-load conditions, also considering $\Theta_{PM} =$ 20 °C.

Characteristic currents ($\hat{I}_{\text{ch}}$) are calculated for both motor types to assess their flux weakening capability:

$$\hat{I}_{\text{ch}} = \frac{\lambda_{\text{PM}}}{L_d}$$

Motors with $\hat{I}_{\text{ch}}$ greater than the rated current are typically governed by Maximum Torque per Ampere (MTPA) until the inverter voltage limit is reached. Subsequently, the motor can only attain a finite speed, and the output power tends toward zero. For $\hat{I}_{\text{ch}} = \hat{I}_{\text{s,ph,N}}$, the motor theoretically achieves infinite speed. The power vs. speed curve asymptotically follows the "characteristic power" (P_{ch}), and the power factor tends toward unity:

$$P_{\text{ch}} = \frac{3}{2} \cdot \hat{U}_{\text{s,ph,N}} \cdot \hat{I}_{\text{ch}}$$

.

In this scenario, where the rated and characteristic currents are equal, the situation is optimal concerning power output. In the third case, if the available rated current ($\hat{I}_{\text{s,ph,N}}$) exceeds $\hat{I}_{\text{ch}}$, the machine may be controlled by MTPA until the voltage limit is reached, after which both current and voltage remain constant. Higher speeds are achieved by reducing the current and following the Maximum Torque per Voltage (MTPV) control strategy, but the power asymptote will be lower than in the second case.

8.3 Performance comparison

In the performance analysis, the motor technology with sleeve is paired and compared with the one with ribs for equal maximum speeds that they can achieve. Three sections will be presented to organize the analysis, where the results will be reported and discussed to compare the two geometries.
The first section deals with the no-load analysis of the magnetic flux density distribution at the air gap and in the stator teeth, in addition to a complete flux density map plotted on the pole geometry of both motor technologies.
In the second section, magnetic models of fluxes concerning currents in the d and q axes will be presented. Just as a quick reminder, the model is commonly articulated using linear relationships $\lambda_d = L_d \cdot i_d + \lambda_P M$ and $I_q = L_q \cdot i_q$ between currents and fluxes, where the inductances L operate in the corresponding axis direction. However, it's crucial to note that the real behavior tends to be mostly nonlinear, primarily owing to magnetic saturation effects. Hence, it is essential to make use of curves able to caputure both the saturation effect and the cross coupling. Following, the characteristic current trends of each motor, plotted on a same new graph for a direct comparison.

Finally, the third section will present the torque and power curves of the two motors, comparing on the same graph the torque curves concerning current and the consequent control locus in the d and q axes. This will include iso-torque and iso-current curves at peak conditions, as well as the MTPA and MTPV curves (if applicable).

The analysis of results for each speed will follow the same descriptive format, aiming to facilitate understanding of the comparison given the large amount of graphs and data presented.

8.3.1 Performance comparison for 14 krpm maximum speed designs

The two geometries compared in this section are the sleeve motor designed in 6.2 and the ribs motor design in 7.3.

No-Load Flux Density Distribution

From the static magnetic solver in FEMM, the no-load flux density distributions are extracted for both motors. The shaft, not considered, is filled with air in both instances.

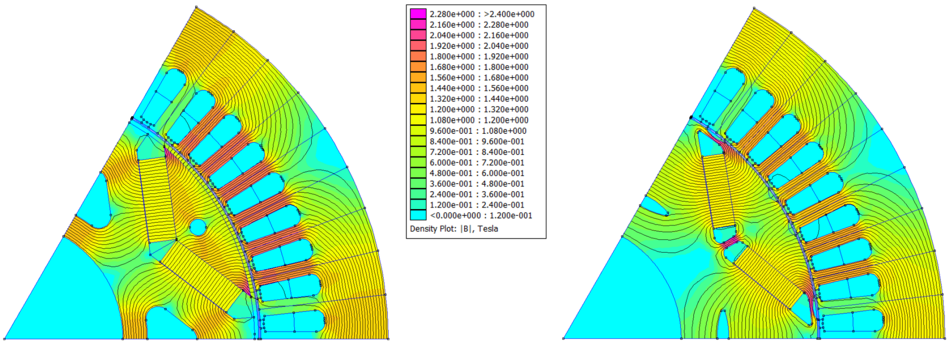

Figure 8.2: No load flux density map of the sleeve motor (left) and the ribs motor (right) designed for 14krpm

In Figure 8.2, the flux density distribution is plotted over the two motors geometries. The sleeve motor (left) has the highest flux density values on the side corners of the rotor pole piece, that are saturated reaching up over 2.4 T. All the other parts of the geometry are under the magnetic saturation level of 2 T.

The ribs motor exhibits its maximum flux densities in the radial and tangential ribs, both reaching magnetic saturation. As already explained in 3.2, this rotor parts are a flux leakage source, reducing the magnet flux crossing the air gap.

In terms of the stators, back-iron flux densities are comparable, with up to 1.5 T in the sleeve motor and 1.4 T in the ribs motor.

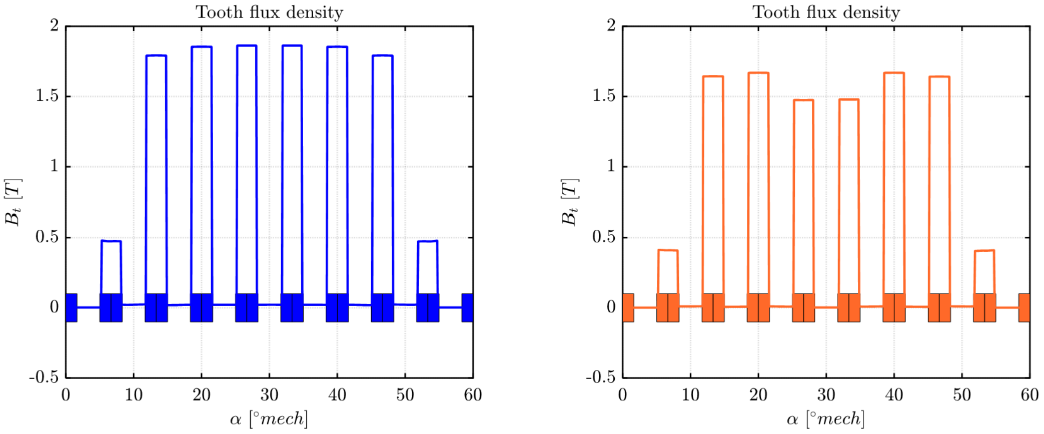

Figure 8.3: No load Tooth flux density distribution of the sleeve motor (left) and the ribs motor (right) designed for 14krpm

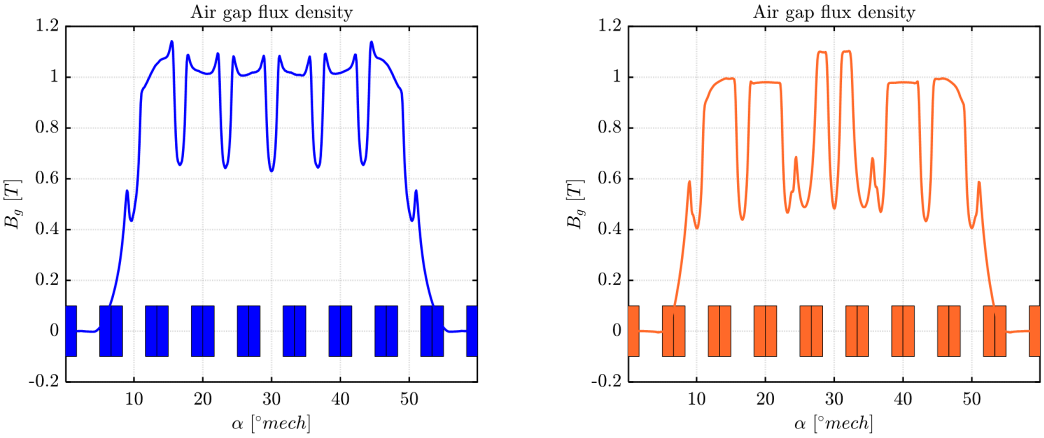

Figure 8.4: No load Air gap flux density distribution of the sleeve motor (left) and the ribs motor (right) designed for 14krpm

Analyzing the air gap and tooth flux densities, as shown in Figure 8.3 and 8.4 (teeth reported by rectangles), a minor decrease in the pole center is observed for the ribs motor. This is attributed to the flux short-circuiting effect provided by the ribs, weakening the flux density in the middle of the pole. In the sleeve motor, on the other hand, the flux density level remains consistently average. The flux density of the sleeve motor stator teeth has a top value around of 1.8 T.

It is indeed a warring value, considering that under load this iron parts could easily saturate. Nevertheless, the flux density has been evaluated with a magnet temperature of $\Theta_{PM} = 20°$ C, leading to a residual flux density $B_r = 1.45$ T. In usual loading conditions (with current flowing in the windings), the magnets operate at higher temperature values, causing a B_r reduction due to the negative temperature coefficient of *NeFeB* (e.g. for $\Theta_{PM} = 80°$ C the $B_r = 1.35$ T).

In both motors, the maximum air gap flux density is approximately $1.1T$. Additionally, the copper-filled slots naturally cause local, slot-periodic decreases in flux density.

Magnetic Model Comparison and Characteristic Current

As an outcome directly derived from the computation of the flux map, the flux linkages in the d and q axes can be graphed against both i_d and i_q currents, thereby constructing the magnetic model of the machine.

In Figure 8.5, the magnetic models of the two compared motors are presented. Alongside the continuous lines representing exclusive d or q current, the dashed and dotted lines illustrate the flux linkages when both currents are concurrently generating flux. This insight can shed light on cross-saturation effects. The terms $\hat{I}_{d,max}$ and $\hat{I}_{q,max}$ denote the maximum d or q current of the corresponding axis, meaning $\hat{I}_{d,max} = \hat{I}_{q,max} = \hat{I}_{s,ph,N} = 803$ A. Conversely, $\hat{I}_{d,min}$ corresponds to –803 A, and $\hat{I}_{q,min}$ corresponds to 0 A, causing the continuous and dotted blue and dark orange graphs to overlap.

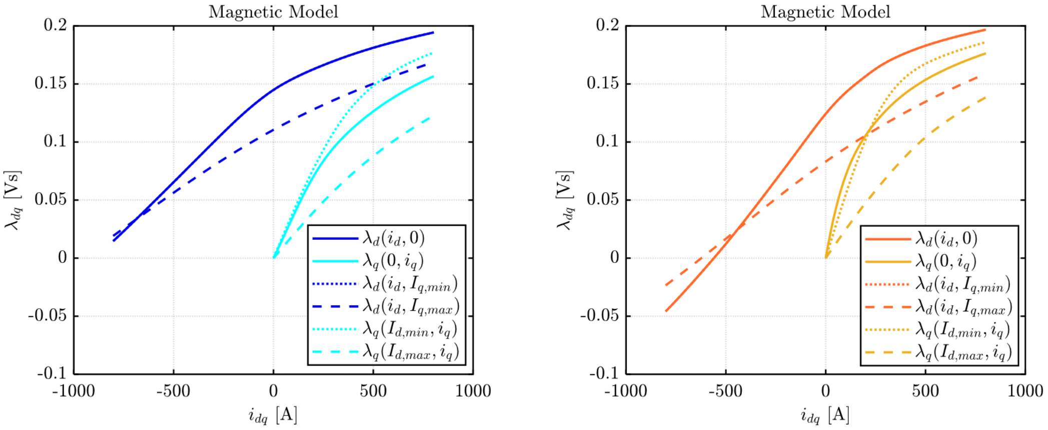

Figure 8.5: Magnetic Model of the sleeve motor (left) and the ribs motor (right) designed for 14krpm

In both magnetic model plots (Figure 8.5) sharing the same axis scale, several distinctions become immediately apparent. Firstly, the PM flux linkages λ_{PM} can be extracted at λ_d when both currents are zero: it is observed 0.145 Vs for the sleeve motor and 0.124 Vs for the ribs motor. Despite utilizing 42.6 % more PM mass and avoiding flux leakage through iron bridges, the increase in $\lambda_P M$ for the sleeve motor is merely 17 %, likely attributed to the larger magnetic air gap that necessitates crossing the sleeve. Considering the larger effective magnetic air gap and thicker PMs in the sleeve motor, the motor inductances are expected to be lower than in the ribs motor. This notion is supported by the overall flatter λ_d and λ_q curves in the S Plaid – the curves appear horizontally "stretched" away from the zero current axis compared to the Model 3 graphs. Based on Figure 8.5, it is possible to estimate the inductances in the linear ranges to be $L_{d,lin} \approx 171$ μH and $L_{q,lin} \approx 333$ μH (sleeve motor), as well as $L_{d,lin} \approx 225$ μH and $L_{q,lin} \approx 603$ μH (ribs motor).

To initially evaluate the reluctance torque performance of the motors, we can now compare the saliency ratios ξ for the inductances in the linear range:

$$\xi = \frac{L_{q,lin}}{L_{d,lin}}$$

Motors with a higher saliency ratio exhibit an increased reluctance torque component. Designs with higher saliency ratios are preferred to enhance overall torque and torque density. For the sleeve motor, we find $\xi = 1.94$, while for the ribs motor, we obtain $\xi = 2.68$, indicating the ribs motor design is superior in utilizing the saliency torque component.

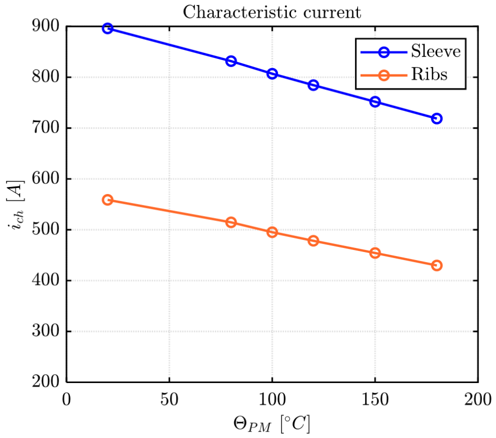

Figure 8.6: Comparison between Characteristic Currents at various temperatures for the sleeve motor and the ribs motor designed for 14krpm

In Figure 8.6 it is reported the comparison between the two characteristic currents of the motors over various PM temperature values. For the sleeve motor, the characteristic current $\hat{I}_{\text{ch}}$ is higher than rated current $\hat{I}_{s,ph,N} = 803$ used for the performance analysis until a magnet temperature $\Theta_{PM} = 100°$. It means that below that magnet temperature, the sleeve motor will always operate with MTPA control up to maximum speed. It is not the case for the ribs motor, that already from $\Theta_{PM} = 20°$ (the temperature considered in this analysis) needs a MTPV operation after a certain speed. This operation degradates the high speed power for the ribs motor, differently from the sleeve rotor that will have a flat power curve over speed.

Torque and Power Curves and Rating

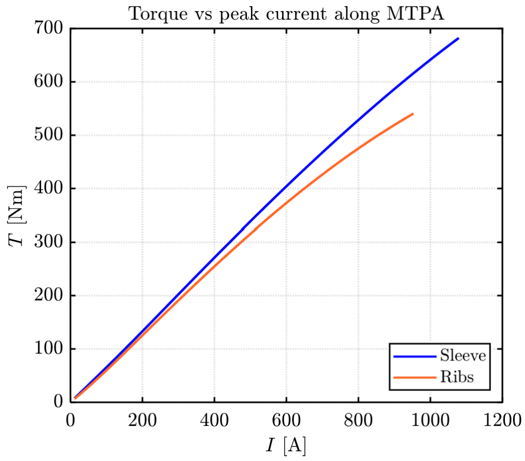

Figure 8.7: Comparison between Torque vs. Peak current along MTPA sleeve motor and rib motor designed for 14krpm

Torque production over current is displayed in Figure 8.7 for the two motors. It is clearly visible how the sleeve motor make better use of the current to produce torque at most of the current level. Especially after 200 A, the torque production starts to drop for the ribs motor, while it remains pretty linear for the sleeve motor. At the rated current $\hat{I}_{s,ph,N} = 803$, the torque difference is substantial. This will be even more clear looking at the torque curves here below.

In the coming plots, some markers will define the points of interest for the control behaviour just described. The symbol “$\circ$” will mark the end of the constant max. torque region, which defines the rated point of each motor. “$\diamond$” will indicate the beginning of the MTPV control range (only ribs motors) and “$\star$” the max. operating speed.

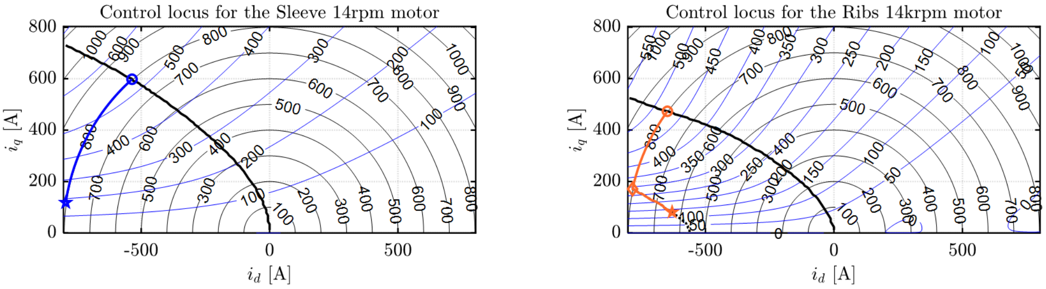

Figure 8.8: Control Locus of the sleeve motor (left) and rib motor (right) designed for 14krpm

In Figure 8.8, it is shown on the Control locus d,q plane what has been described for looking at the characteristic currents. The sleeve motor is controlled with MTPA until the max current value, which is kept until the maximum achievable speed. On the other hand, the ribs motor needs to switch to MTPV at a certain speed in order to mantain a certain max. torque at reduced current and machine flux.

This trends are even more clear looking at the curves of different motor parameters over speed.

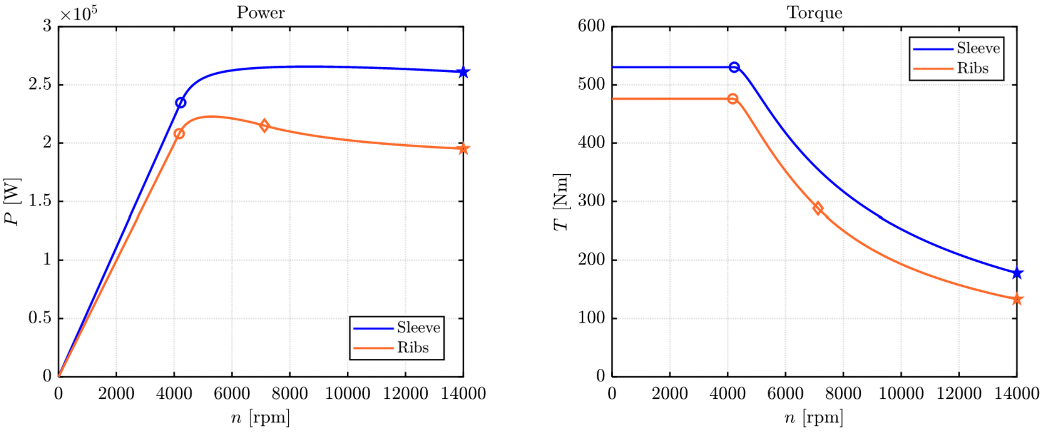

Figure 8.9: Power and Torque operation limit curves comparison between sleeve motor and ribs motor designed for 14krpm

In Figure 8.9, power and torque limit curves are reported and compared between the two motor technologies. The sleeve motor operating limits are distinctly higher than the ribs motor ones over all speed values. It is possible to notice the power degradation of the ribs motor compared to the almost flat curve of the sleeve motor.

Furthermore, the better utilization of the current for the sleeve motor leads to a higher max. torque all over the speed range.

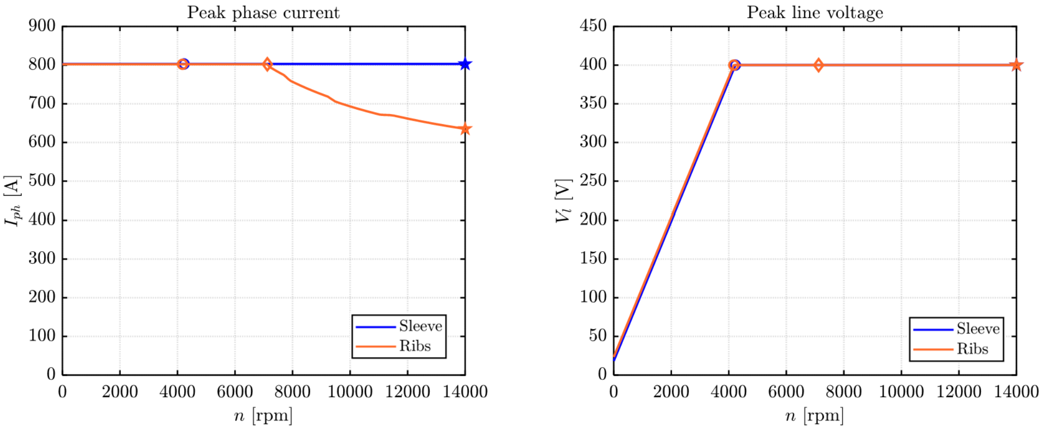

Figure 8.10: Peak phase current and Peak line voltage operation limit curves comparison between sleeve motor and ribs motor designed for 14krpm

In the left plot of Figure 8.10, the current trend for the ribs motor is demonstrating what described for the control locus.

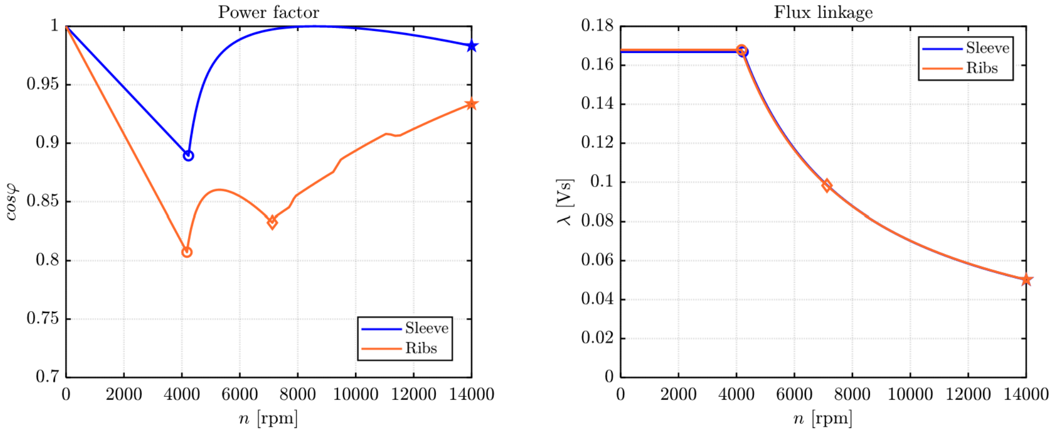

Figure 8.11: Power factor and Flux linkage operation limit curves comparison between sleeve motor and ribs motor designed for 14krpm

The left plot of Figure 8.11 reporting the power factor shows that, particularly after in the field weakening region, the sleeve motor has a way better performance in power conversion. Flux linkage looks to be slightly higher for the ribs motor in the constant power region, and equalize the sleeve motor one after base speed.

8.3.2 Performance comparison for 18 krpm maximum speed designs

The two geometries compared in this section are the sleeve motor designed in 6.3 and the ribs motor design in 7.4. The comparison will be more synthetic compared to the one did for the 14krpm motor, avoiding to repeat the already explained concepts and focusing more on the results.

No-Load Flux Density Distribution

Flux density distribution plot in Figure 8.12 shows how the thick ribs are holding back even more flux compared to the lower speed version.

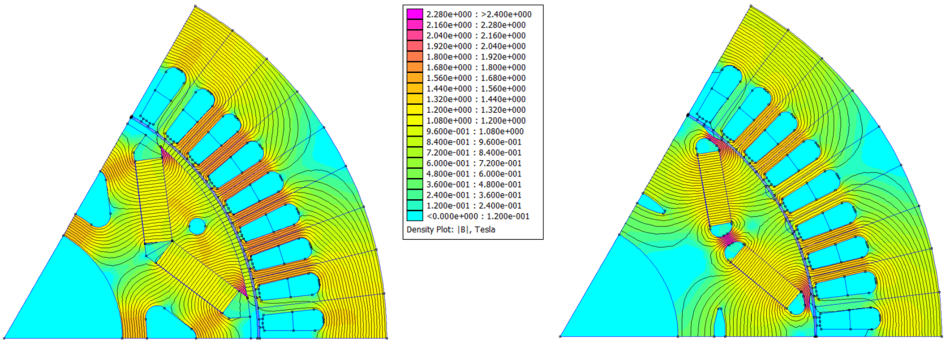

Figure 8.12: No load flux density map of the sleeve motor (left) and the ribs motor (right) designed for 18krpm

In terms of the stators, back-iron flux density is slightly lower in the ribs motor, reaching average values of 1.3 T compared to the 1.45 T in the sleeve motor.

The same difference in flux density magnitude can be observed in the stator teeth (Figure 8.13), that for both motor is below the saturation limit. The air gap flux density (Figure 8.14) have similar values in both the sleeve motor and the ribs motor, being around 0.9 T.

Magnetic Model Comparison and Characteristic Current

In both magnetic model plots (Figure 8.15) sharing the same axis scale, several distinctions become immediately apparent. Firstly, the PM flux linkages λ_{PM} can be extracted at λ_d when both currents are zero: it is observed 0.135 Vs for the sleeve motor and 0.112 Vs for the ribs motor. Despite utilizing 42.6 % more PM mass and avoiding flux leakage through iron bridges, the increase in λ_{PM} for the sleeve motor is merely 20 %, likely attributed to the larger magnetic air gap that necessitates crossing the sleeve.

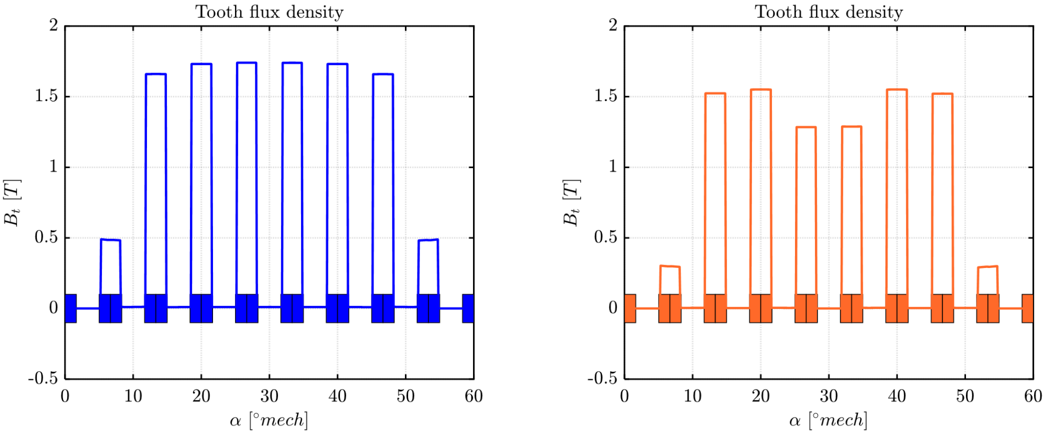

Figure 8.13: No load Tooth flux density distribution of the sleeve motor (left) and the ribs motor (right) designed for 18krpm

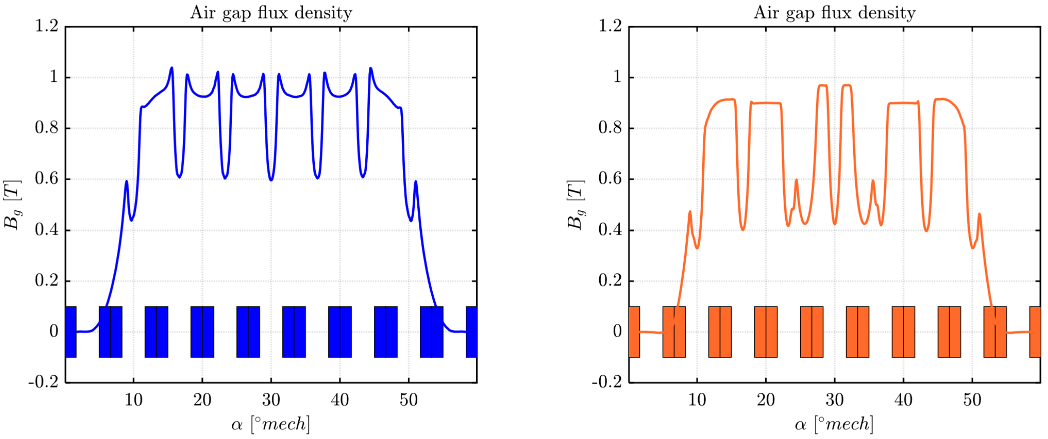

Figure 8.14: No load Air gap flux density distribution of the sleeve motor (left) and the ribs motor (right) designed for 18krpm

Based on Figure 8.15, it is possible to estimate the inductances in the linear ranges to be $L_{d,lin} \approx 159$ μH and $L_{q,lin} \approx 297$ μH (sleeve motor), as well as $L_{d,lin} \approx 243$ μH and $L_{q,lin} \approx 717$ μH (ribs motor).

To initially evaluate the reluctance torque performance of the motors, we can now compare the saliency ratios ξ for the inductances in the linear range:

$$\xi = \frac{L_{q,lin}}{L_{d,lin}}$$

For the sleeve motor, we find $\xi = 1.87$, while for the ribs motor, we obtain

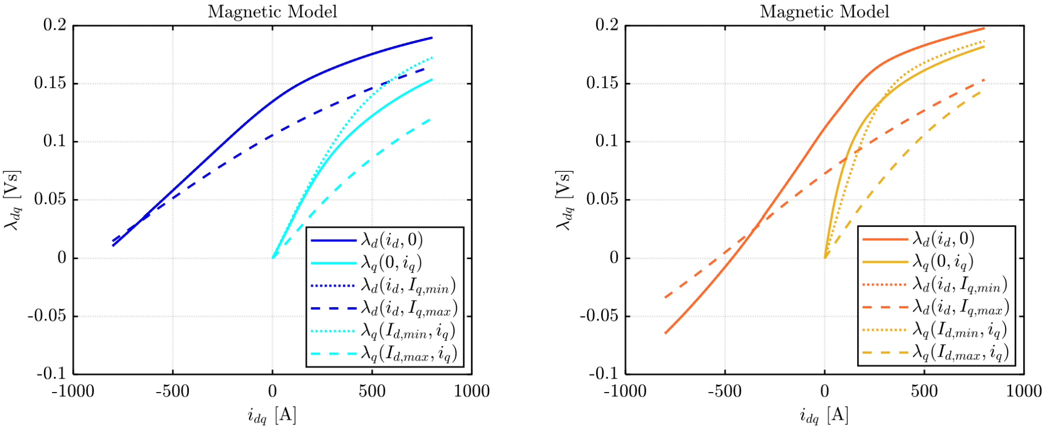

Figure 8.15: Magnetic Model of the sleeve motor (left) and the ribs motor (right) designed for 18krpm

$\xi = 2.95$, indicating the ribs motor design is superior in utilizing the saliency torque component.

In Figure 8.16 it is reported the comparison between the two characteristic currents of the motors over various PM temperature values. For the sleeve motor, the characteristic current $\hat{I}_{\text{ch}}$ is higher than rated current $\hat{I}_{s,ph,N} = 803$ used for the performance analysis until a magnet temperature $\Theta_{PM} = 80°$ C. It means that below that magnet temperature, the sleeve motor will always operate with MTPA control up to maximum speed. It is not the case for the ribs motor, that already from $\Theta_{PM} = 20°$ (the temperature considered in this analysis) needs a MTPV operation after a certain speed. This operation degradates the high speed power for the ribs motor, differently from the sleeve rotor that will have a flat power curve over speed. Compared to the ribs motor designed for 14krpm, the new ribs motor have considerably lower characteristic currents. On the other hand, the new sleeve for the sleeve motor is not affecting the characteristic current values so drastically.

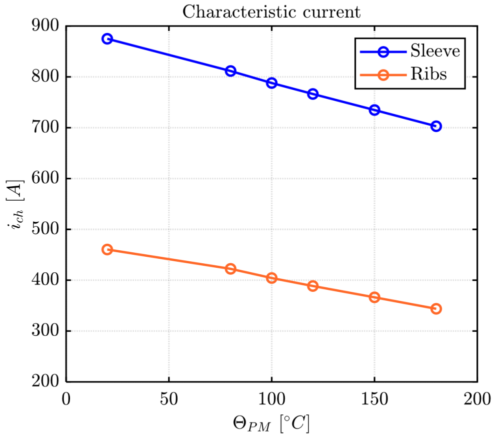

Figure 8.16: Comparison between Characteristic Currents at various temperatures for the sleeve motor and the ribs motor designed for 18krpm

Torque and Power Curves and Rating

Torque production over current is displayed in Figure 8.17 for the two motors. It is clearly visible how the sleeve motor make better use of the current to produce torque at most of the current level, and the difference is slightly more remarked compared to the 14krpm versions.

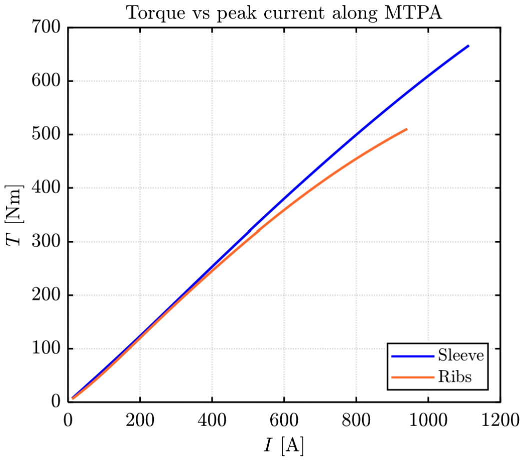

Figure 8.17: Comparison between Torque vs. Peak current along MTPA sleeve motor and rib motor designed for 18krpm

In the coming plots, some markers will define the points of interest for the control behaviour just described. The symbol "○" will mark the end of the constant max. torque region, which defines the rated point of each motor. "◇" will indicate the beginning of the MTPV control range (only ribs motors) and “⋆” the max. operating speed.

In Figure 8.17, it is shown on the Control locus d,q plane, where the only difference from the 14krpm designs is the MTPV control region for the ribs motor, that is moderately wider.

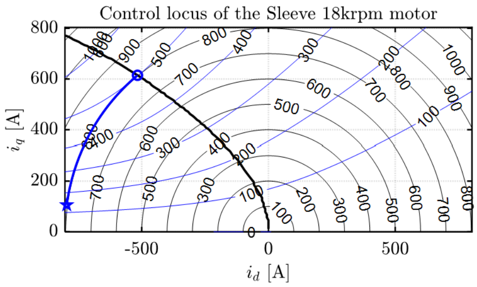

Figure 8.18: Control Locus of the sleeve motor (left) and rib motor (right) designed for 18krpm

This trends are even more clear looking at the curves of different motor parameters over speed.

In Figure 8.19, power and torque limit curves are reported and compared between the two motor technologies. The same trend visualized for the 14krpm motors can be noticed. The main difference is that the power gap bewteen the sleeve motor and the ribs motor is even more remarked.

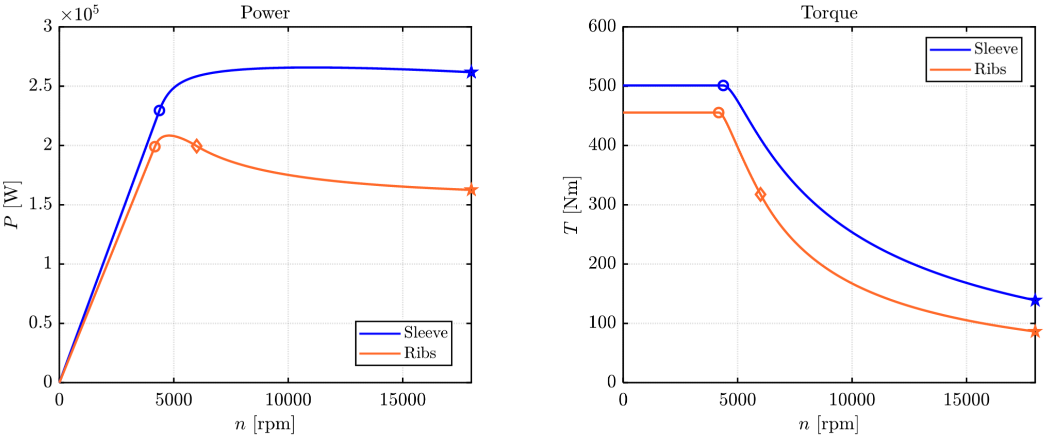

Figure 8.19: Power and Torque operation limit curves comparison between sleeve motor and ribs motor designed for 18krpm

Looking at the current degradation of the ribs motor on the left plot in Figure

8.20 the higher power gap is explained. The wider utilization of the MTPV control for the ribs motor has a big impact on the high speed power reduction.

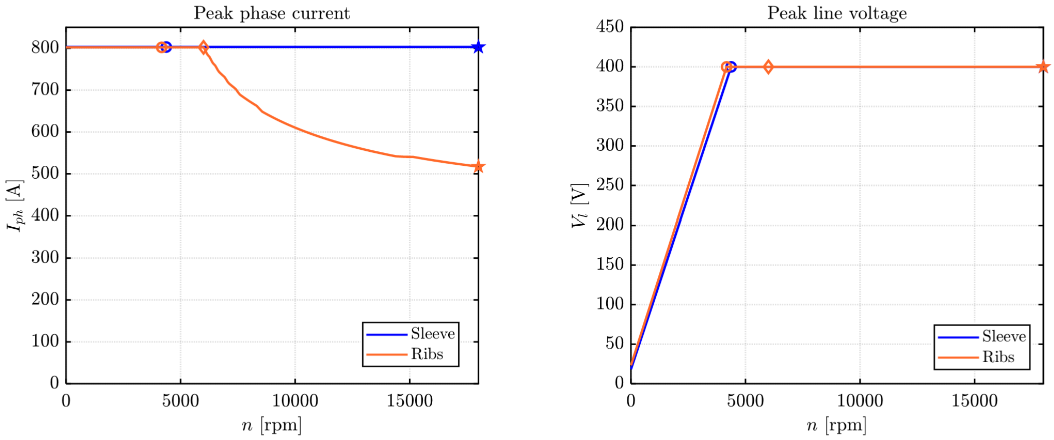

Figure 8.20: Peak phase current and Peak line voltage operation limit curves comparison between sleeve motor and ribs motor designed for 18krpm

The trends in 8.21 show that for both motors the increase of maximum achievable speed brought to a power factor degradation in equal measure. Regarding the flux linkage, the ribs motor design present a higher value in the constant torque region.

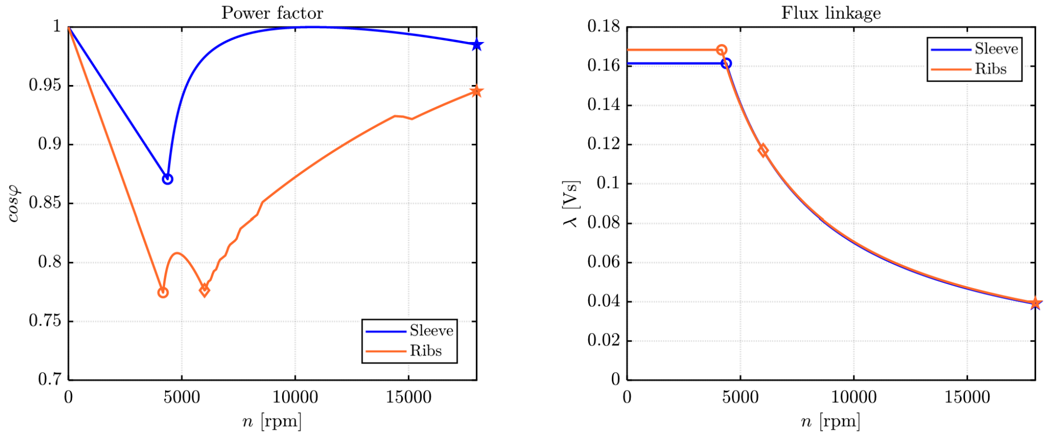

Figure 8.21: Power factor and Flux linkage operation limit curves comparison between sleeve motor and ribs motor designed for 18krpm

8.3.3 Performance comparison for 21 krpm maximum speed designs

The two geometries compared in this section are the sleeve motor designed in 6.4 and the ribs motor design in 7.5.

No-Load Flux Density Distribution

Flux density distribution plot in Figure 8.22 shows how the thick ribs are holding back even more flux compared to the lower speed versions.

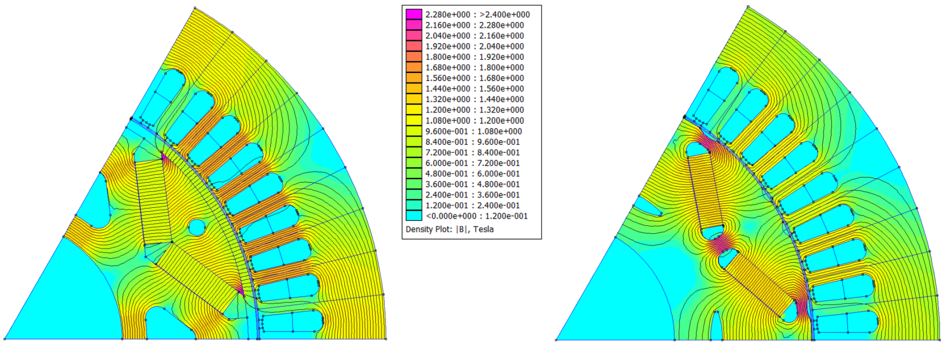

Figure 8.22: No load flux density map of the sleeve motor (left) and the ribs motor (right) designed for 21krpm

In terms of the stators, back-iron flux density is considerably lower in the ribs motor, reaching average values of 1 T compared to the 1.25 T in the sleeve motor.

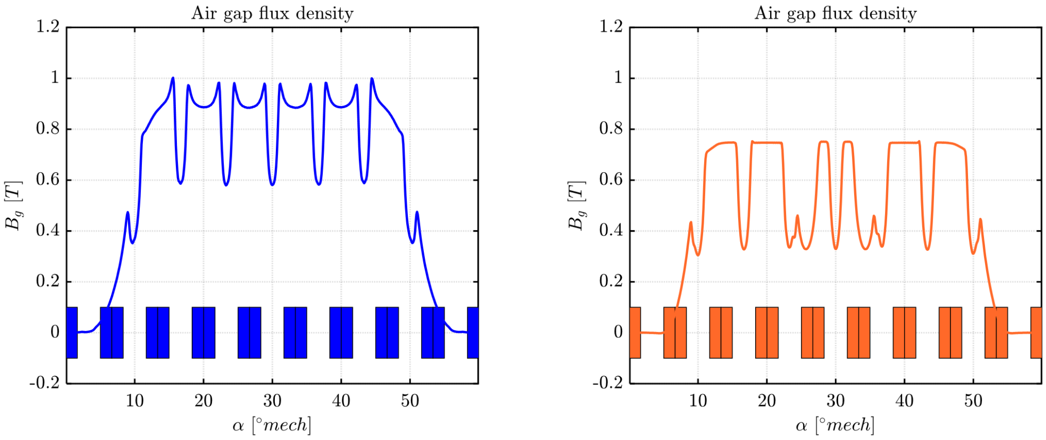

Figure 8.23: No load Air gap flux density distribution of the sleeve motor (left) and the ribs motor (right) designed for 21krpm

A even more remarked difference in flux density magnitude can be observed in the stator teeth (Figure 8.13), that for both motor is below the saturation limit, and in the air gap flux density (Figure 8.14), which is around 0.9 T for the sleeve motor and 0.75T for the ribs motor.

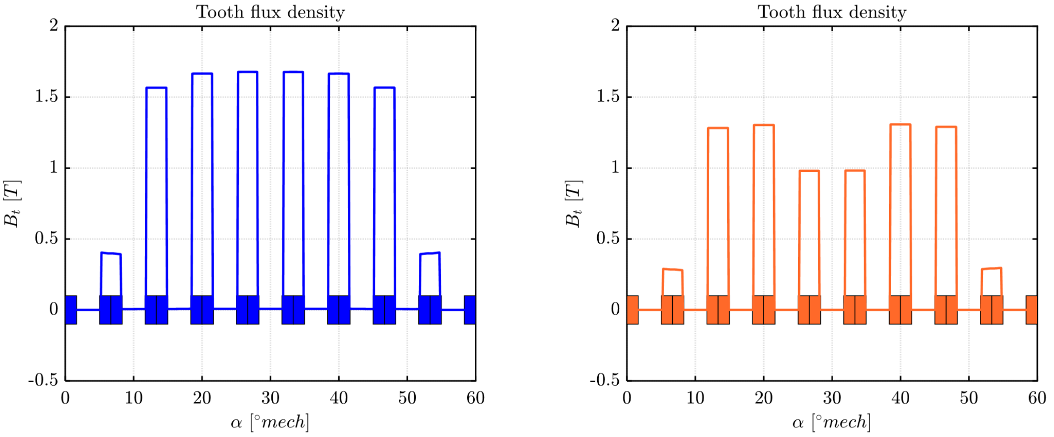

Figure 8.24: No load Tooth flux density distribution of the sleeve motor (left) and the ribs motor (right) designed for 21krpm

Magnetic Model Comparison and Characteristic Current

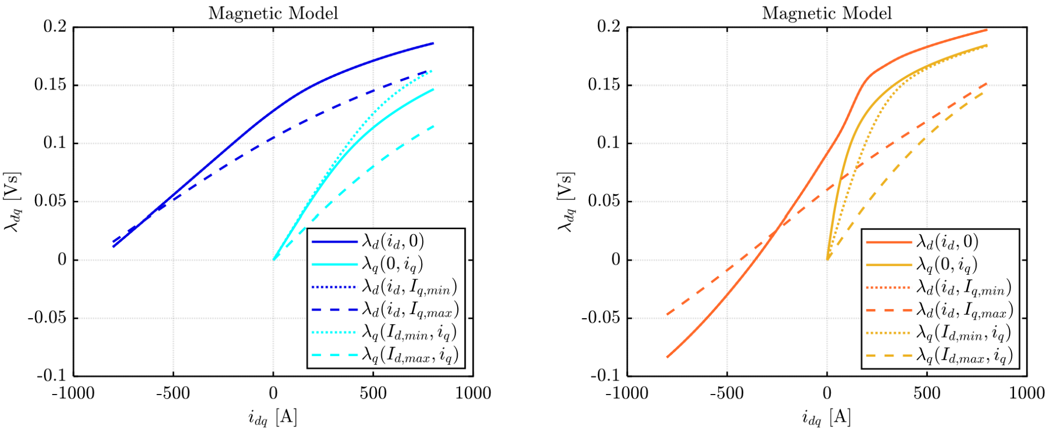

Figure 8.25: Magnetic Model of the sleeve motor (left) and the ribs motor (right) designed for 21krpm

In both magnetic model plots (Figure 8.25) sharing the same axis scale, several distinctions become immediately apparent. Firstly, the PM flux linkages λ_{PM} can be extracted at λ_d when both currents are zero: it is observed 0.128 Vs for the sleeve motor and 0.091 Vs for the ribs motor. For the 21krpm design, the 42.6 % more PM mass is finally making a significant difference, thanks to the increase in $\lambda_P M$ for of 40 %. Based on Figure 8.25, it is possible to estimate the inductances in the linear ranges to be $L_{d,lin} \approx 148$ μH and $L_{q,lin} \approx 253$ μH (sleeve motor), as well as $L_{d,lin} \approx 253$ μH and $L_{q,lin} \approx 905$ μH (ribs motor).

To initially evaluate the reluctance torque performance of the motors, we can now compare the saliency ratios ξ for the inductances in the linear range:

$$\xi = \frac{L_{q,lin}}{L_{d,lin}}$$

For the sleeve motor, we find $\xi = 1.70$, while for the ribs motor, we obtain $\xi = 3.57$, indicating the ribs motor design has more than double the saliency torque component than the sleeve motor.

In Figure 8.26 it is reported the comparison between the two characteristic currents of the motors over various PM temperature values. The trends are again very similar to the 14krpm and the 18krpm designs. Compared to the ribs motor designed for 18krpm, the new ribs motor have even lower characteristic currents. On the other hand, the sleeve motor characteristic is slightly increased compared to the 18krpm design. This means that probably there is a local minimum of characteristic current values between the 14krpm and the 21krpm designs.

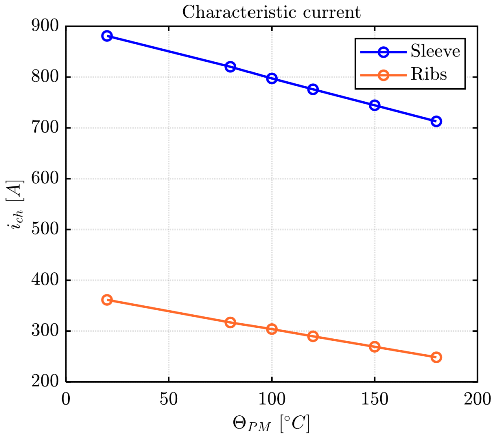

Figure 8.26: Comparison between Characteristic Currents at various temperatures for the sleeve motor and the ribs motor designed for 21krpm

Torque and Power Curves and Rating

Torque production over current is displayed in Figure 8.27 for the two motors. It is clearly visible how the sleeve motor make better use of the current to produce torque at most of the current level, and the difference is even more remarked compared to the lower speed versions.

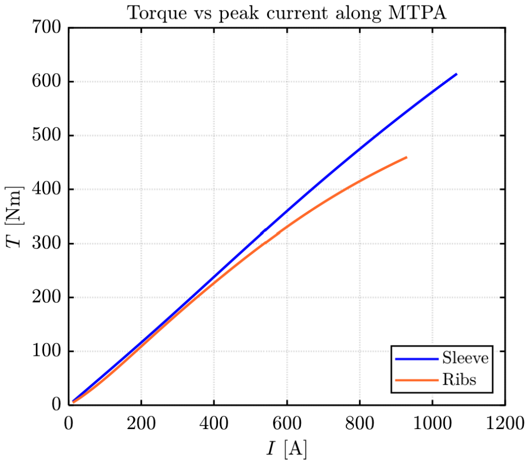

Figure 8.27: Comparison between Torque vs. Peak current along MTPA sleeve motor and rib motor designed for 21krpm

In the coming plots, some markers will define the points of interest for the control behaviour just described. The symbol “○” will mark the end of the constant max. torque region, which defines the rated point of each motor. “◇” will indicate the beginning of the MTPV control range (only ribs motors) and “⋆” the max. operating speed. In Figure 8.28, it is shown on the Control locus d,q plane, where the only difference from the 14krpm and 18krpm designs is the MTPV control region for the ribs motor, that is this time considerably wider.

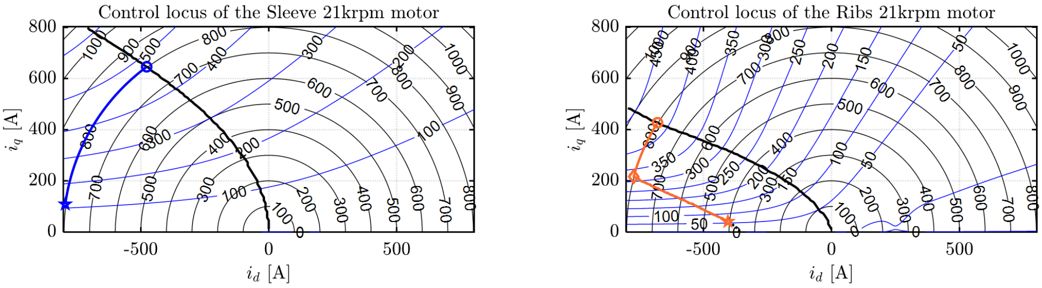

Figure 8.28: Control Locus of the sleeve motor (left) and rib motor (right) designed for 21krpm

In Figure 8.29, power and torque limit curves are reported and compared between the two motor technologies. The same trend visualized for the design for lower maximum speeds can be noticed. The power degradation for the ribs motor at 21krpm is massive compared to the sleeve motor. The sleeve motor keeps is flat power trend up to the maximum speed, as already seen for the lower speed designs.

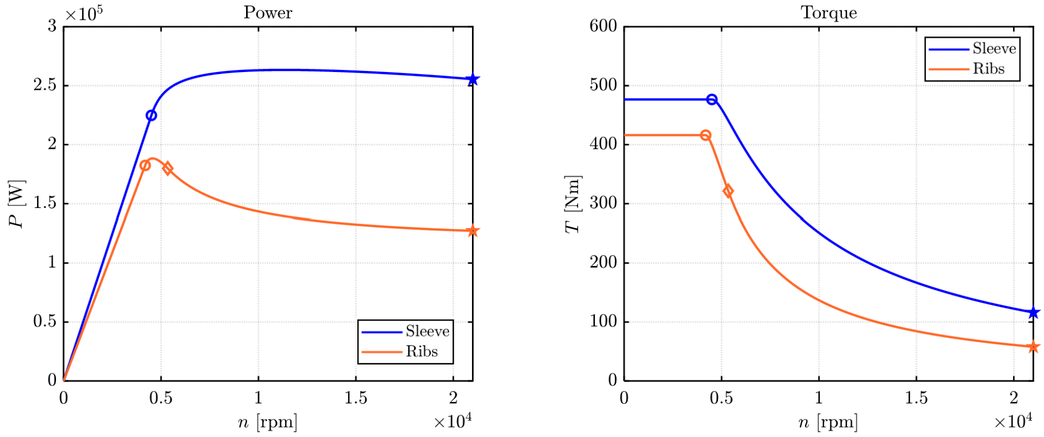

Figure 8.29: Power and Torque operation limit curves comparison between sleeve motor and ribs motor designed for 21krpm

The begin of the MTPV control for the ribs motor starts right after the base speed. As shown in the left plot of Figure 8.30, its rated current drops drastically, leading to a considerable power reduction.

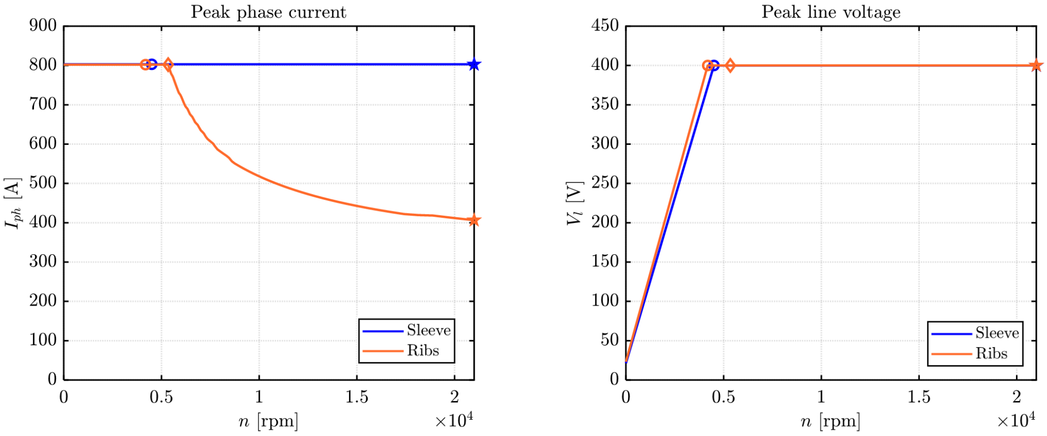

Figure 8.30: Peak phase current and Peak line voltage operation limit curves comparison between sleeve motor and ribs motor designed for 21krpm

The trends in 8.31 show that the higher speed design for ribs motor is subject to a big power factor degradation compared to the sleeve motor. Regarding the flux linkage, the ribs motor design present a again a higher value in the constant torque region.

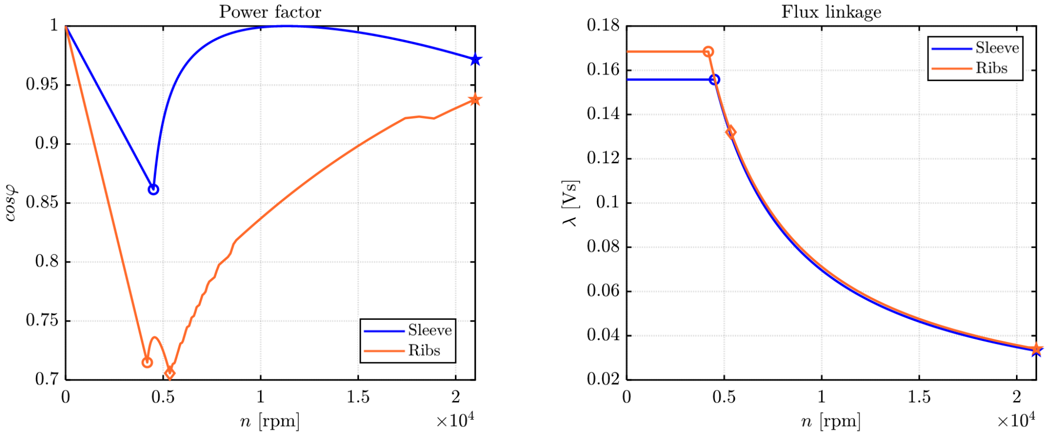

Figure 8.31: Power factor and Flux linkage operation limit curves comparison between sleeve motor and ribs motor designed for 21krpm

8.4 Efficiency comparison

Efficiency and loss maps derive from simulations, with 200 data points each for speed and torque. The ensemble of losses includes iron losses (eddy-current and hysteresis losses in stator and rotor iron) and stator Joule losses (resistive losses in stator windings). PM losses are excluded due to inconsistency in evaluating this component for sleeve motors, estimated to be an order of magnitude lower than iron losses with a similar speed trend. The skin effect, causing increased effective stator resistance in AC operation, is considered. Mechanical losses from bearings or air drag are neglected. The loss maps at different speeds need rescaling with the corresponding stator frequency, automated by SyR-e.

8.4.1 14 krpm

Efficiency comparison is illustrated in Figure 8.32. Both motors achieve max efficiencies of up to 97 %. However, the sleeve motor exhibits higher efficiencies in a wider area of operation, particularly at high torque.

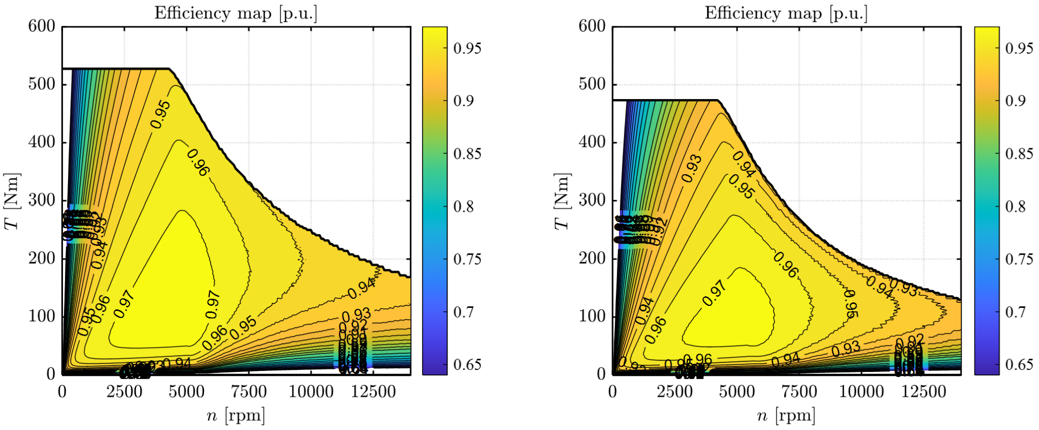

Figure 8.32: Efficiency maps of the sleeve motor (left) and the ribs motor (right) designed for 14krpm

Looking at the iron loss components in Figure 8.33, it can be noticed how the sleeve motor exhibits lower values in all the operating points. However, the ribs motor exhibits lower Joule losses (Figure 8.34 at high speeds, thanks to the higher component of reluctance torque of this technology. The two losses components combined are making the two motors equally efficient at high speeds. Nevertheless, the better current utilization of the sleeve motor for torque production makes it more efficient at high torque operations before 10000 rpm.

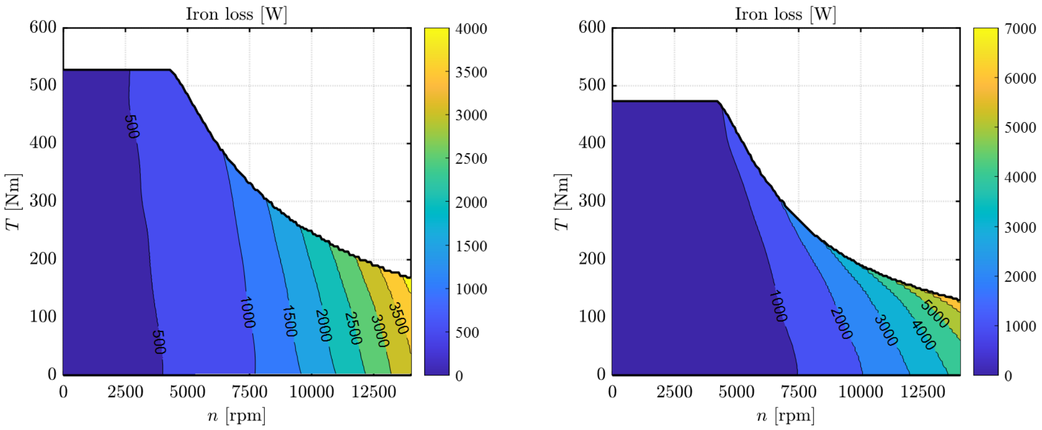

Figure 8.33: Iron Loss maps of the sleeve motor (left) and the ribs motor (right) designed for 14krpm

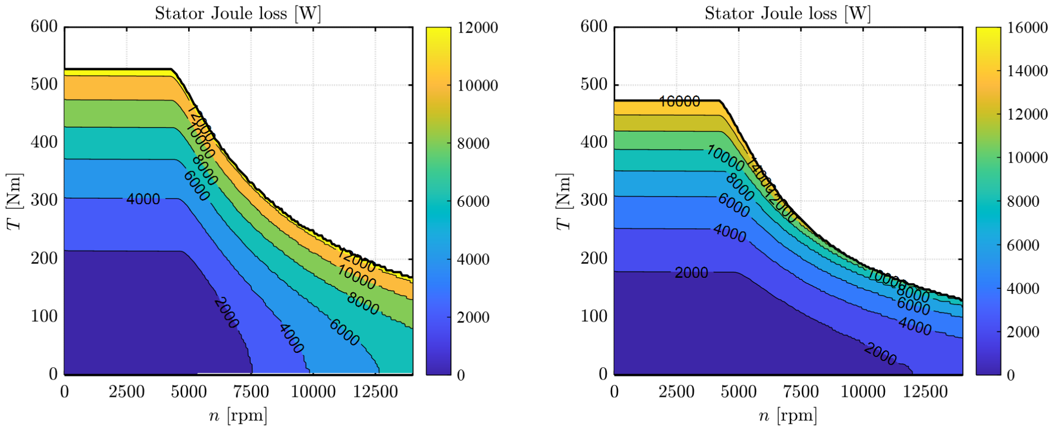

Figure 8.34: Joule Loss maps of the sleeve motor (left) and the ribs motor (right) designed for 14krpm

Consistent with the earlier analysis of speed characteristics, the sleeve motor demonstrates a strictly larger output power (Figure 8.35). Additionally, its power factor (Figure 8.36) is superior, particularly around the rated point of the two machines.

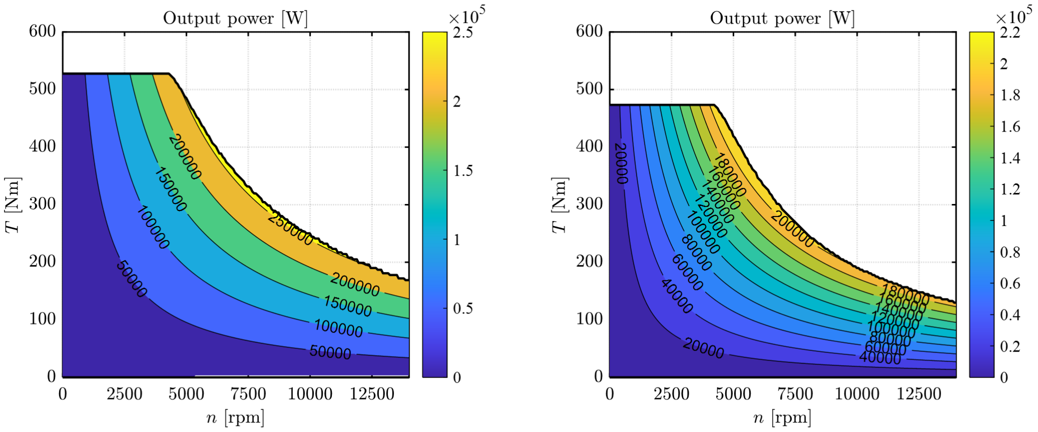

Figure 8.35: Power maps of the sleeve motor (left) and the ribs motor (right) designed for 14krpm

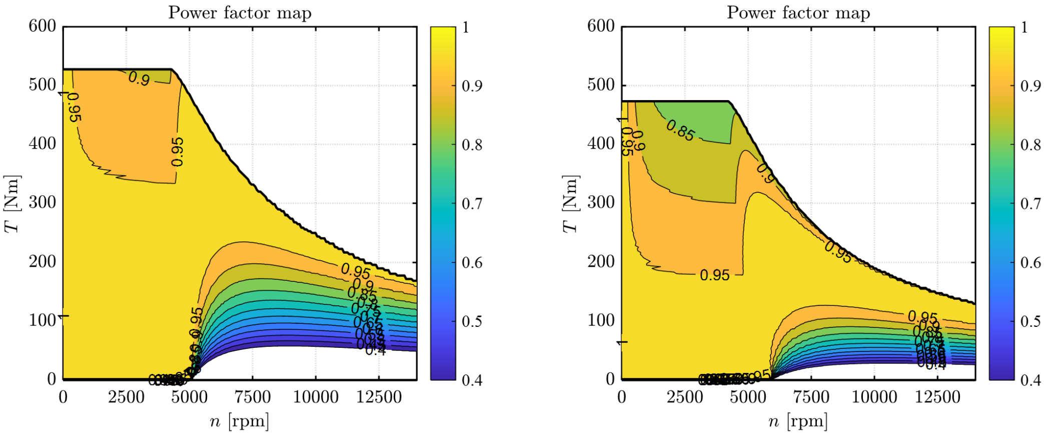

Figure 8.36: Power Factor maps of the sleeve motor (left) and the ribs motor (right) designed for 14krpm

In the current maps in Figure 8.37, the higher current current utilization of the sleeve motor at high speed is remarked. The ribs motor employs MTPV control to reduce stator current with rising speed (contributing also to lower Joule losses).

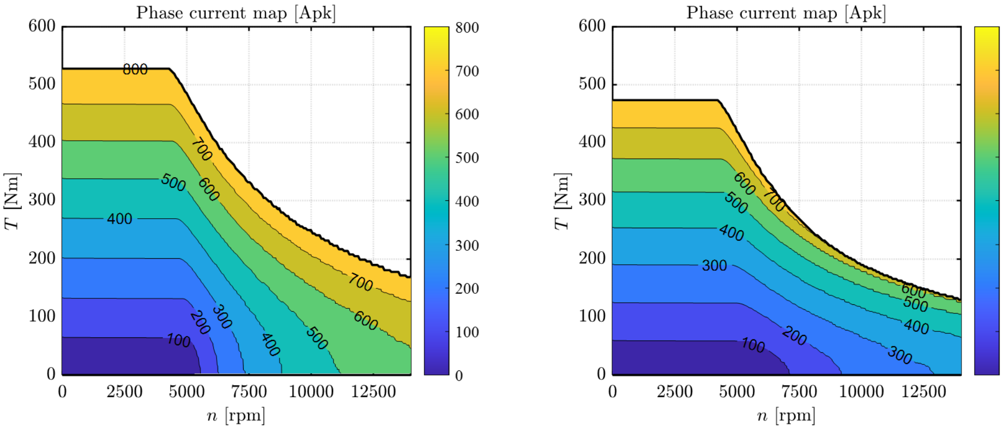

Figure 8.37: Phase current maps of the sleeve motor (left) and the ribs motor (right) designed for 14krpm

8.4.2 18 krpm

Efficiency comparison is illustrated in Figure 8.38. Both motors achieve max efficiencies of up to 97 %. However, the sleeve motor designed for 18krpm max. speed becomes slightly more efficient also at high speed compared to the ribs motor.

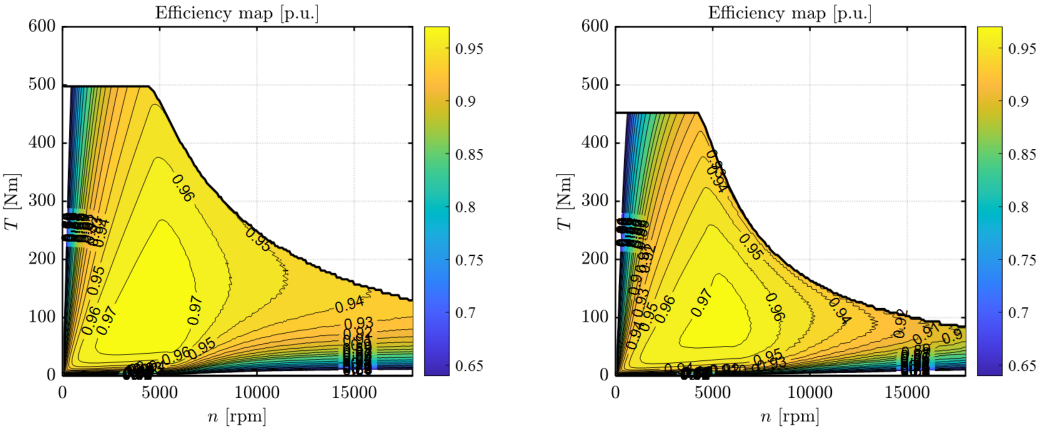

Figure 8.38: Efficiency maps of the sleeve motor (left) and the ribs motor (right) designed for 18krpm

Although the Joule losses (Figure 8.40) keep the same trend compared to the lower speed designs, the iron losses are considerably different. The ribs motor exhibits almost double the iron losses in every operating region, reason why the high speed efficiency appears to be compromised.

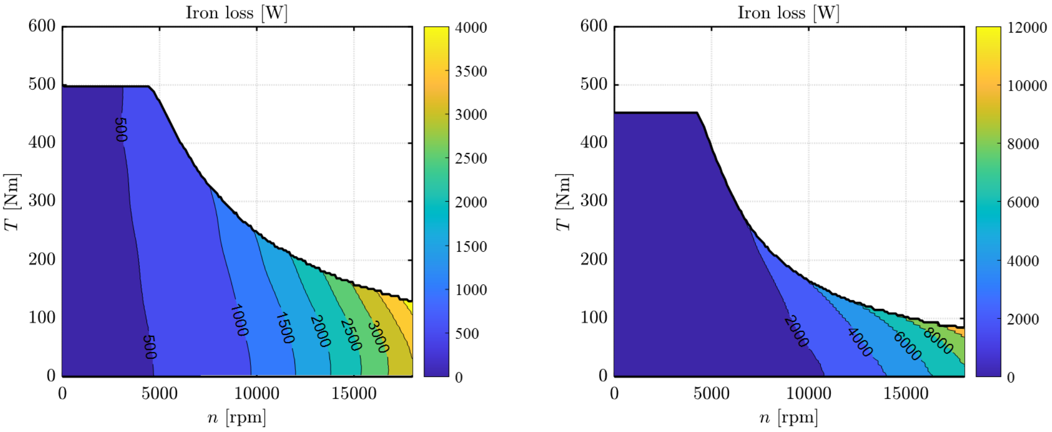

Figure 8.39: Iron Loss maps of the sleeve motor (left) and the ribs motor (right) designed for 18krpm

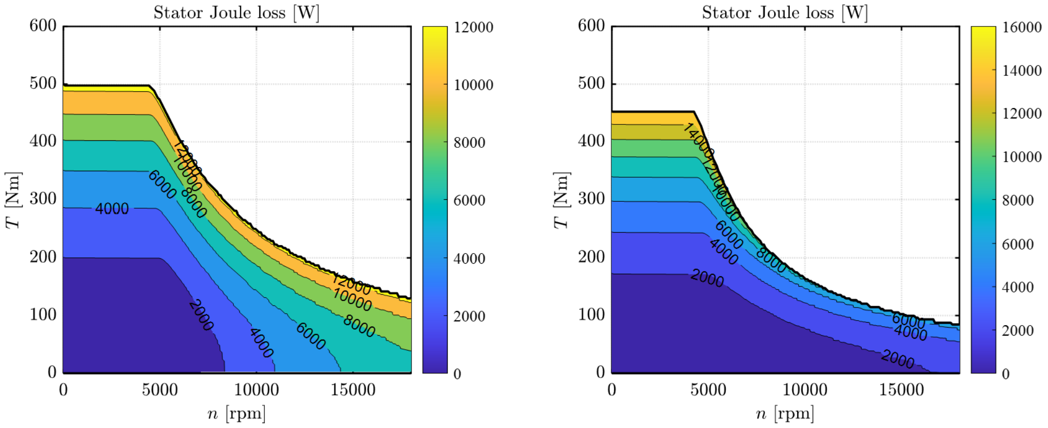

Figure 8.40: Joule Loss maps of the sleeve motor (left) and the ribs motor (right) designed for 18krpm

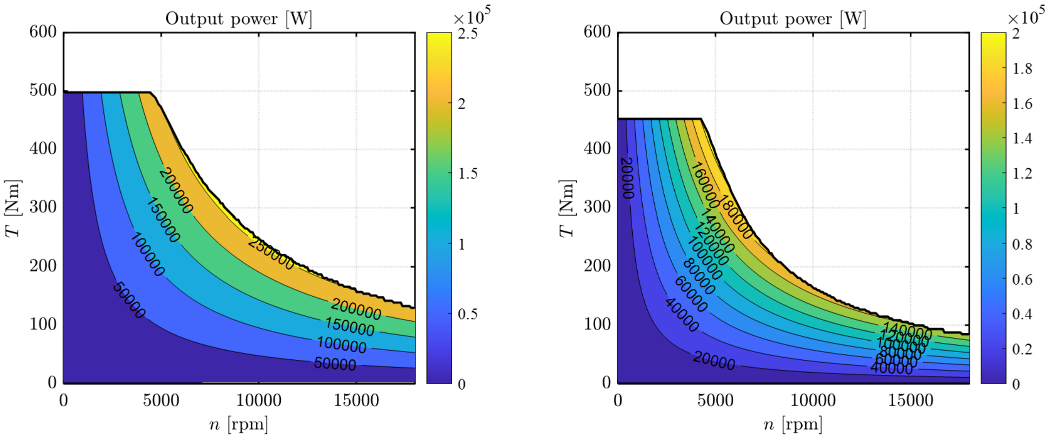

Figure 8.41: Power maps of the sleeve motor (left) and the ribs motor (right) designed for 18krpm

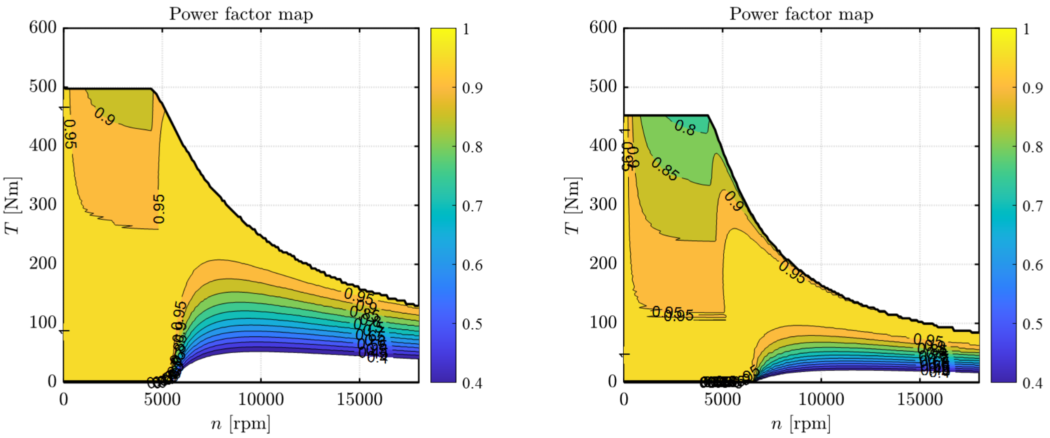

Figure 8.42: Power Factor maps of the sleeve motor (left) and the ribs motor (right) designed for 18krpm

Coherently with the previous analysis of speed characteristics, the sleeve motor demonstrates again a larger output power (Figure 8.41). Additionally, its power factor (Figure 8.42) is superior, particularly around the rated point of the two machines.

In the current maps in Figure 8.43, the higher current current utilization of the sleeve motor at high speed is remarked. The ribs motor employs MTPV control to reduce stator current with rising speed (contributing also to lower Joule losses)

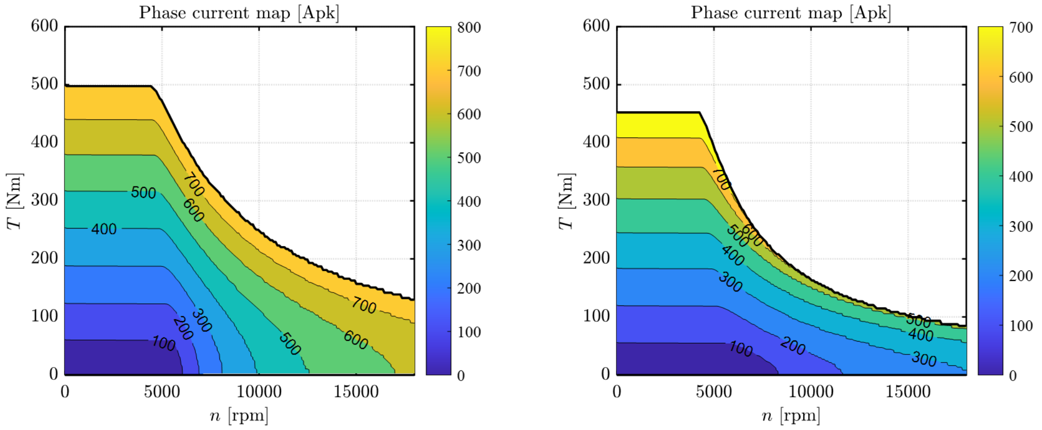

Figure 8.43: Phase Current maps of the sleeve motor (left) and the ribs motor (right) designed for 18krpm

8.4.3 21 krpm

Efficiency comparison is illustrated in Figure 8.44. Both motors achieve max efficiencies of up to 97 %. The sleeve motor present again higher efficiency in most of the operating points. Especially, it is capable to provide way higher performances compared to the ribs motor, maintaining good efficiencies in the whole envelope.

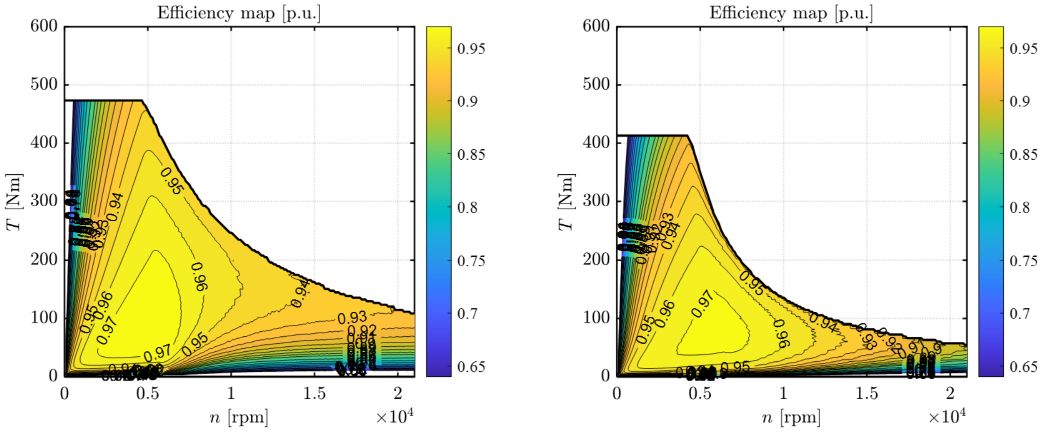

Figure 8.44: Efficiency maps of the sleeve motor (left) and the ribs motor (right) designed for 21krpm

In Figure 8.45 are reported the Joule losses maps, which are visibly higher in the sleeve motor at high speed operating conditions. The trend for the iron losses (Figure 8.45) is opposite, showing higher losses for the ribs motor at higher speeds.

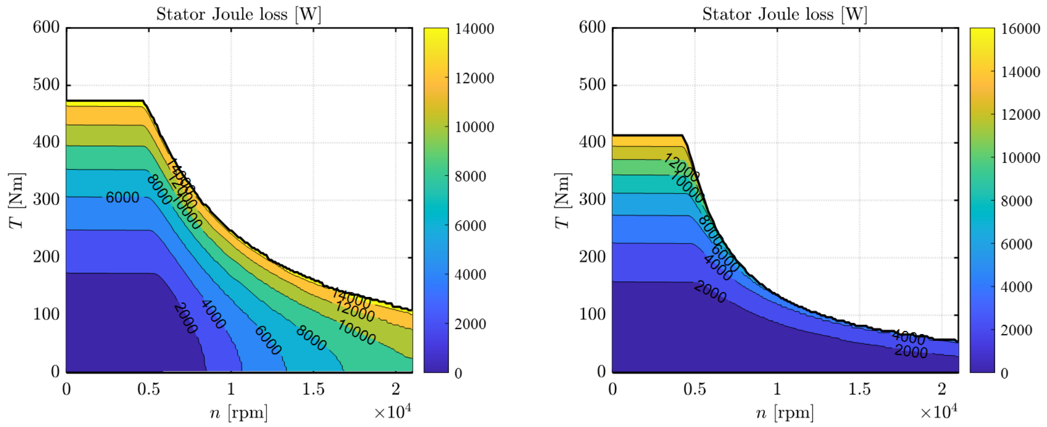

Figure 8.45: Joule Losses maps of the sleeve motor (left) and the ribs motor (right) designed for 21krpm

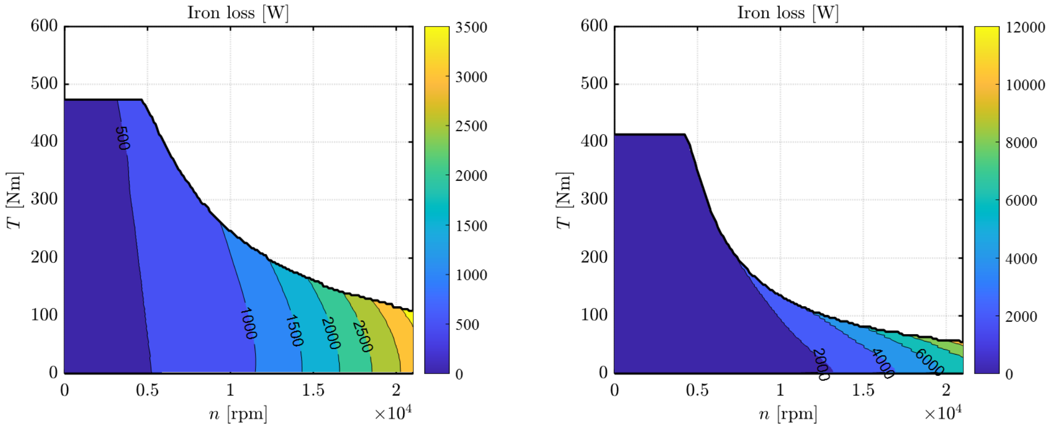

Figure 8.46: Iron Losses maps of the sleeve motor (left) and the ribs motor (right) designed for 21krpm

The trends shown on Power (Figure 8.47), Power Factor (Figure 8.48) and phase current (8.49) are similar to the ones described for lower speeds. The comparison shows how the sleeve motor at 21krpm result way more powerful and capable of better performance compared to the ribs motor.

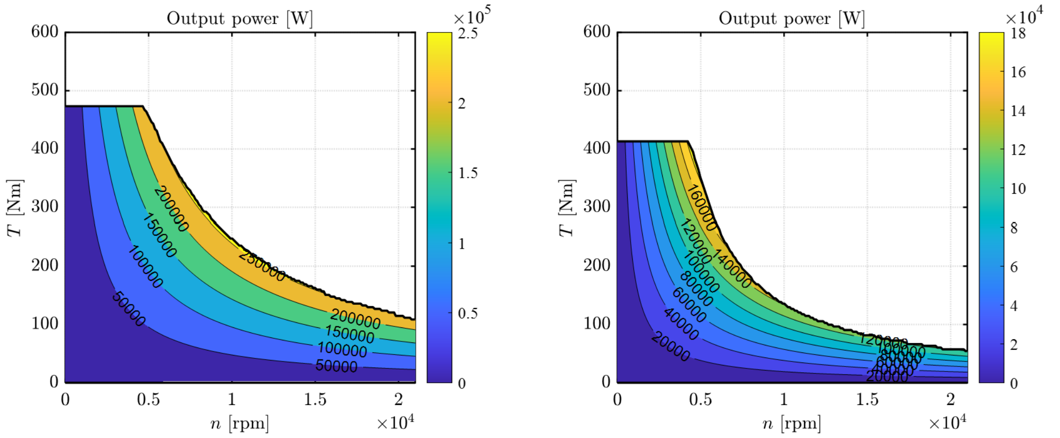

Figure 8.47: Power maps of the sleeve motor (left) and the ribs motor (right) designed for 21krpm

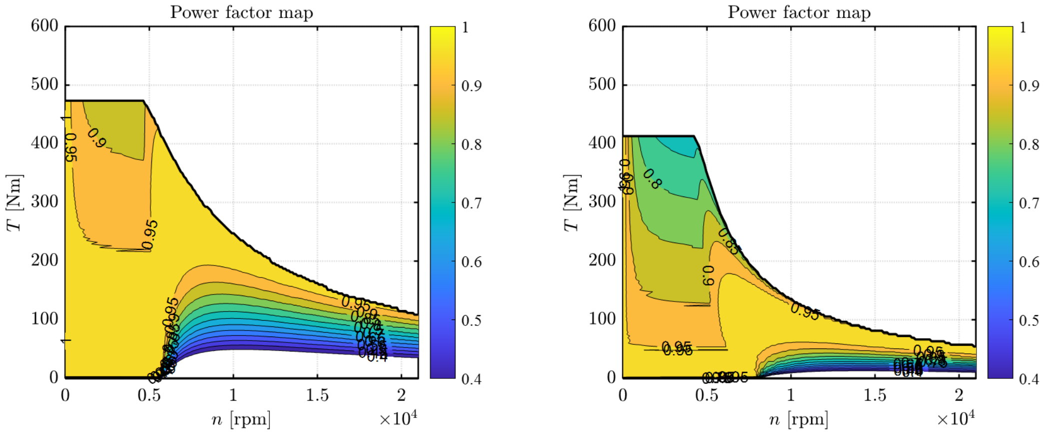

Figure 8.48: Power Factor maps of the sleeve motor (left) and the ribs motor (right) designed for 21krpm

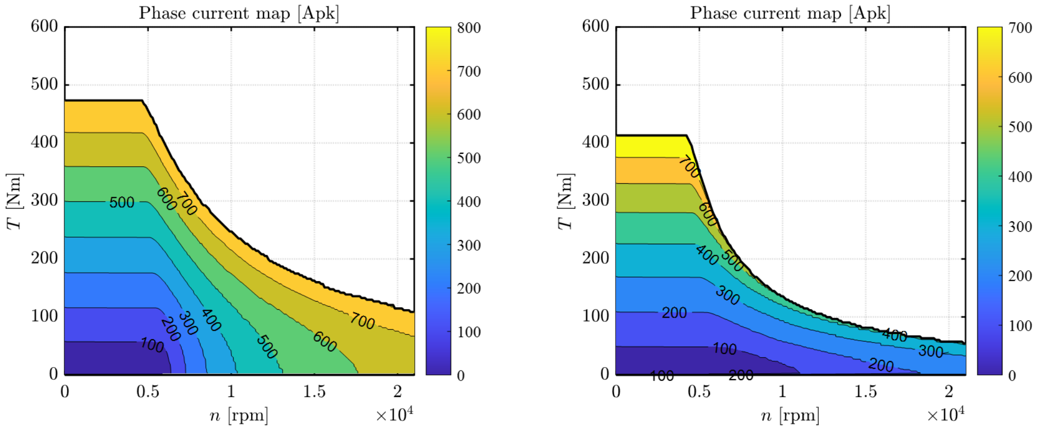

Figure 8.49: Phase Current maps of the sleeve motor (left) and the ribs motor (right) designed for 21krpm

8.5 Summary of the comparison

	Ribs motor			Sleeve motor		
Max. speed [krpm]	**14**	**18**	**21**	**14**	**18**	**21**
Peak Power [kW]	223	208 **(-7.0%)**	188 **(-18.3%)**	266 **(+16.1%)**	266 **(+16.1%)**	263 **(+15.4%)**
Peak Torque [Nm]	476	455 **(-4.5%)**	416 **(-14.6%)**	530 **(+10.2%)**	501 **(+5.0%)**	477 **(+0.1%)**
Power at max. speed [kW]	195	163 **(-20.1%)**	127 **(-53.3%)**	261 **(+25.2%)**	262 **(+25.4%)**	256 **(+23.6%)**
Torque at max. speed [Nm]	133.2	86.2 **(-54.5%)**	57.9 **(-130.1%)**	178 **(+25.2%)**	138.9 **(+4.1%)**	116.2 **(-14.6%)**
Base speed [rpm]	4174	4172 **(0.0%)**	4185 **(+0.3%)**	4227 **(+1.3%)**	4373 **(+4.6%)**	4504 **(+7.3%)**
PM flux linkage [Vs]	0.124	0.112 **(-10.7%)**	0.091 **(-36.3%)**	0.145 **(+14.5%)**	0.135 **(+8.1%)**	0.128 **(+3.1%)**
Saliency ratio	2.68	2.95 **(+9.2%)**	3.57**(+24.9)**	1.94 **(-38.1%)**	1.85 **(-44.9%)**	1.7 **(-57.6%)**
Motor Mass [kg]	34.64	34.86 **(+0.62%)**	34.89 **(+0.7%)**	33.34 **(-3.75%)**	33.34 **(-3.75%)**	32.77 **(-5.39%)**

Table 8.1: Summary table for the motor comparison. The percentage values are referred to the 14krpm motor. In green: benefit. In red: disadvantage.

The Table 8.1 presented reports and summarizes the data extracted from the analyses described in the previous sections. It is immediately noticeable how sleeve motors undoubtedly exhibit higher values in terms of maximum power and maximum torque compared to ribs motors. Additionally, sleeve motors are lighter than ribs motors. This implies that they have higher power density and torque density, confirming the predictions. The use of the sleeve thus provides a significant advantage in automotive applications.

Comparing the saliency ratios, it can be observed that as the speed increases, the two motors exhibit different trends in reluctance torque production. The sleeve motor loses this torque as the sleeve thickness increases, relying more on the torque produced by the magnet flux. Conversely, the ribs motors have higher reluctance torque as the rib thickness increases but unfortunately experience a drastic loss of magnet flux due to the growing flux leakage saturating the ribs with the increase of the maximum achievable speed.

Moreover, as can be observed from the comparison of power and torque curves (Figure (8.50)), motors with the sleeve maintain significant power and torque values at high speeds. This is not the case for motors with ribs, which, as the maximum achievable speed of the motor increases, exhibit a considerable decrease in power and torque at high speeds. For example, high-performance electric vehicles that demand exceptional capabilities, high-speed power is a crucial parameter to continue accelerating even when the vehicle is operating at high speeds.

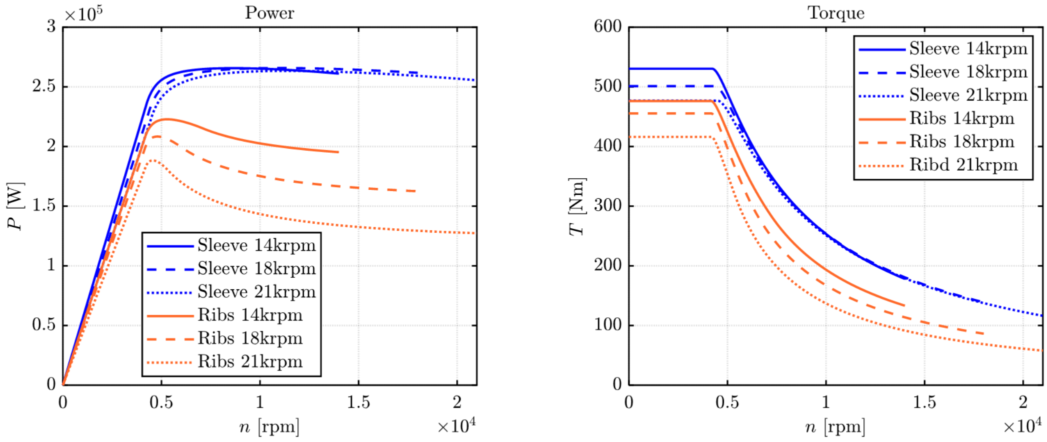

Figure 8.50: Power and Torque operating limits comparison for the 6 designed motors

8.6 Scaling trends for sleeve and ribs over speed

In this concluding section are reported the scaling trends for the crucial parameters examined in the design of the two motor technologies for the maximum achievable speed increase.

For the sleeve motor, the sole parameter under consideration is the sleeve thickness. Concerning the ribs motor, it is noteworthy to report both the tangential and radial ribs.

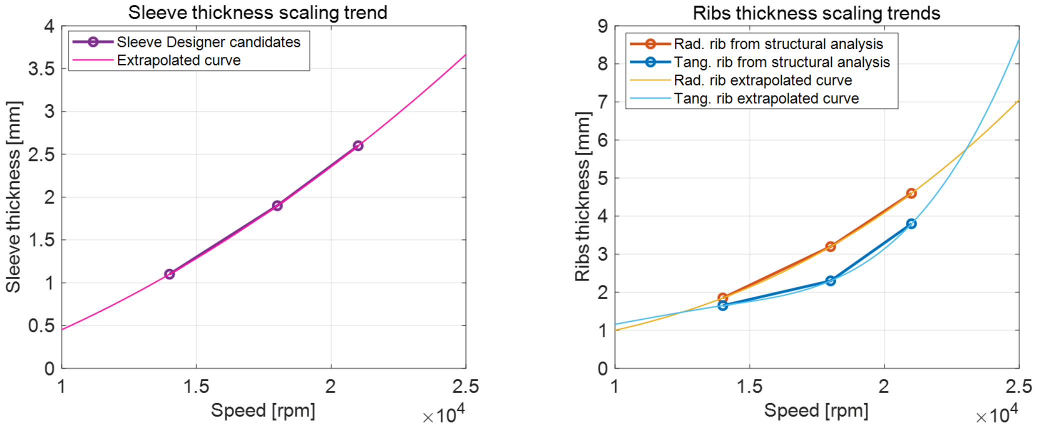

Figure 8.51: Scaling trends for the sleeve thickness (left) and the ribs (right) versus speed

As illustrated in Figure 8.51, the values obtained through the design process are plotted for each scaling trend. Additionally, curves are interpolated within the 14 krpm to 21 krpm range and extrapolated to cover speeds from 10 krpm to 25 krpm.

From the plots, it is evident that both the sleeve thickness and the radial rib thickness show similar trends as the maximum speed for which the motor is designed increases. Both curves exhibit an exponential development. A possible future development of these results could involve creating two analytical functions capable of generalizing the sizing of sleeves and ribs.

Chapter 9

Conclusion

In this final section, conclusions will be based on the comprehensive analysis and investigation conducted on high-speed motors, especially the design and performance of sleeve and ribs motors for automotive applications, as well as the development of the Sleeve Designer Tool.

9.1 Results of this research

Starting from an in-depth investigation into high-speed electric motor types adopted in the automotive industry, two main categories of motors developed by Tesla for the Model 3 and the Model S Plaid were thoroughly examined in this paper. These motors were chosen for their outstanding performance and advanced technological features. Both motors belong to the IPM V-Shape category and were analyzed for their differences, with a particular focus on the application of a carbon sleeve around the rotor in the Model S motor. This sleeve enhances its power density compared to the Model 3 motor, which is a "typical" IPM motor utilizing ribs for structural containment.

The two distinct technologies were thoroughly analyzed, and the design process was investigated. Starting with the motor featuring the carbon sleeve, an analytical model for the design process was presented, implemented, and optimized for use through Matlab. By applying the theories of the analytical model, a pre-design tool for fundamental structural parameters of the motor with the sleeve was developed: the Sleeve Designer.

The final form of the Sleeve Designer, consolidates essential information for designing sleeves that maximize motor performance. By incorporating temperature-dependent effects and applying a safety factor, this tool enables users to explore various sleeve thickness and interference combinations to meet specific speed requirements. Using the newly designed tool, 3 motors capable of sustaining maximum speeds of 14,000, 18,000, and 21,000 rpm, respectively, were designed, providing the fundamental parameters for each motor.

In order to confirm the benefits of using sleeve motors, 3 motors at the same speeds were designed using the rib technology. To control the structural parameters of these designs, an iterative optimization using finite element analysis was adopted. For these three motors as well, fundamental parameters for structural retention were reported, primarily involving the thickness of radial and tangential ribs.

The investigation into ribs motor design added valuable insights to the comprehensive analysis of sleeve and ribs motors for automotive applications. The optimization of ribs parameters for different target speeds demonstrated the importance of understanding the intricate details of motor design to achieve optimal performance.

In the final part of the thesis, the comparison of performance metrics between sleeve and ribs motors revealed distinctive trends and advantages associated with each design. Sleeve motors consistently demonstrate higher values for both maximum power and maximum torque across a range of speeds, showcasing superior performance compared to their ribs counterparts. Moreover, the analysis of high-speed operation emphasized the sustained performance of sleeve motors, maintaining significant power and torque even at elevated speeds. In contrast, ribs motors experience a considerable decrement in power and torque as the maximum achievable speed increases. .
Sleeve motors consistently achieve higher efficiencies, reaching up to 97 %, compared to ribs motors, which exhibit lower efficiency values, particularly at high operating speeds. The identified sources of losses, including iron losses and stator Joule losses, contribute to the overall performance disparity. Notably, the iron losses in ribs motors become pronounced at high speeds, influencing their efficiency negatively. Sleeve motors not only outperform ribs motors in terms of maximum power and torque but also exhibit lower weight. This translates to higher power density and torque density in sleeve motors, aligning with initial predictions.

9.2 Advancement in SyR-e within the Context of this Work

The extensive use of SyR-e in this thesis not only allowed exploring its capabilities but also improving some aspects of the software particularly relevant to the context of the motors investigated in this thesis work.

The parameterization of the sleeve was slightly modified by changing the definition of the air gap in the main tab from magnetic air gap to mechanical air gap. This allows distinct assignment of values to the air gap and sleeve thickness, consequently scaling the rotor as the parameters vary. Additionally, the parameterization of the flux barriers has been enhanced, making it more independent of the sleeve thickness.

Another significant improvement concerned the structural analysis using the PDE Tool in MATLAB. Specifically, the assignment of boundary conditions for the rotor was investigated and improved. The edges of the rotor, when structurally simulated using a single polar step of the motor, are now free to move if subjected to displacement from radial forces. This ensures that the presence of slots at the rotor edges no longer generates asymmetries in the structural analysis as it did previously.

Finally, the Sleeve Designer, the tool created for the preliminary design of sleeve parameters, has been implemented in a provisional version within the Option tab of SyR-e, and a dedicated graphical interface has been created. In addition, several analysis tools using the equivalent model have been further implemented. As a preliminary phase of the tool, with further compatibility work, the Sleeve Designer can be included in the official version of SyR-e in the near future.

9.3 Open points and future developments

- Implement a MODE optimization tool to minimize the rotor flux leakage for a certain speed target maintaining the mechanical stress of the lamination under the maximum Von Mises stress limit.
- Integrate a structural analysis software that allows to simulate the movement of the magnets inside the barrier. This would unlock, for example, the possibility to capture the retaining effect of the holders that keep the magnet in position inside the cavity of the rotor.
- Develop an analytical model to implement multiple barrier layers for the sleeve motor and integrating it into the tool.
- Development of analytical functions to generalize the sizing of sleeves and ribs based on the observed exponential trends.
- Refine the Sleeve Designer tool, in order to include it in the official version of SyR-e.

Bibliography

[1] Roland Irle. «Global EV Sales for 2022». In: *EV-Volumes* (2023). URL: `https://www.ev-volumes.com/` (cit. on pp. 1, 2).

[2] Simone Ferrari. «SyR-e». In: (April 27, 2023). URL: `https://github.com/SyR-e` (cit. on pp. 5, 7).

[3] Simone Ferrari. «syreManual». In: (May 24, 2023). URL: `https://github.com/SyR-e/syre_public/blob/main/Readme/syreManual.pdf` (cit. on p. 6).

[4] Ansys. «Ansys Motor-CAD». In: (). URL: `https://www.ansys.com/products/electronics/ansys-motor-cad` (cit. on p. 13).

[5] Ansys. «Ansys Maxwell». In: (). URL: `https://www.ansys.com/products/electronics/ansys-maxwell` (cit. on p. 13).

[6] Siemens. «Simcenter MagNet». In: (). URL: `https://plm.sw.siemens.com/it-IT/simcenter/electromagnetics-simulation/magnet/` (cit. on p. 13).

[7] Plexim. «PLECS». In: (). URL: `https://www.plexim.com/products/plecs` (cit. on p. 13).

[8] Bulent Sarlioglu, Casey T. Morris, Di Han, and Silong Li. «Benchmarking of electric and hybrid vehicle electric machines, power electronics, and batteries». In: *2015 Intl Aegean Conference on Electrical Machines Power Electronics (ACEMP), 2015 Intl Conference on Optimization of Electrical Electronic Equipment (OPTIM) 2015 Intl Symposium on Advanced Electromechanical Motion Systems (ELECTROMOTION)*. 2015, pp. 519–526. DOI: `10.1109/OPTIM.2015.7426993` (cit. on pp. 14, 17).

[9] David Gerada, Abdeslam Mebarki, Neil L. Brown, Chris Gerada, Andrea Cavagnino, and Aldo Boglietti. «High-Speed Electrical Machines: Technologies, Trends, and Developments». In: *IEEE Transactions on Industrial Electronics* 61.6 (2014), pp. 2946–2959. DOI: `10.1109/TIE.2013.2286777` (cit. on p. 15).

[10] Torsten Epskamp, Benjamin Butz, and Martin Doppelbauer. «Design and analysis of a high-speed induction machine as electric vehicle traction drive». In: *2016 18th European Conference on Power Electronics and Applications (EPE'16 ECCE Europe)*. 2016, pp. 1–10. DOI: `10.1109/EPE.2016.7695691` (cit. on p. 15).

[11] Bomatec. *BMN-52UH_GBD Datasheet*. URL: `https://www.bomatec.com/wp-content/uploads/2021/05/BMN-52UH_GBD.pdf` (cit. on p. 16).

[12] Fangwu Ma, Hongbin Yin, Lulu Wei, Guangdong Tian, and Hui Gao. «Design and Optimization of IPM Motor Considering Flux Weakening Capability and Vibration for Electric Vehicle Applications». In: *Sustainability* 10.5 (2018). ISSN: 2071-1050. DOI: `10.3390/su10051533`. URL: `https://www.mdpi.com/2071-1050/10/5/1533` (cit. on p. 17).

[13] Bloomberg. «What Engineers Found When They Tore Apart Tesla's Model 3». In: (Oct. 2018). URL: `https://www.youtube.com/watch?v=Lj1a8rdX6DU` (cit. on p. 18).

[14] Liangliang Chen and Changsheng Zhu. «Rotor strength analysis for high speed permanent magnet machines». In: *2014 17th International Conference on Electrical Machines and Systems (ICEMS)*. 2014, pp. 65–69. DOI: `10.1109/ICEMS.2014.7013438` (cit. on p. 19).

[15] Robert Abebe, Mauro Di Nardo, David Gerada, Giovanni Lo Calzo, Luca Papini, and Chris Gerada. «High speed drives review: Machines, converters and applications». In: *IECON 2016 - 42nd Annual Conference of the IEEE Industrial Electronics Society*. 2016, pp. 1675–1679. DOI: `10.1109/IECON.2016.7793721` (cit. on p. 20).

[16] Gianvito Gallicchio, Francesco Cupertino, Mauro Di Nardo, Mohammad Reza Ilkhani, and Chris Gerada. «Design Methodologies of High Speed Surface Permanent Magnet Synchronous Machines». In: *2023 IEEE International Electric Machines Drives Conference (IEMDC)*. 2023, pp. 1–7. DOI: `10.1109/IEMDC55163.2023.10238984` (cit. on p. 20).

[17] Josef Binder. «High-speed IPM Motors with Wrapped Rotor». In: *Technical University of Darmstadt* (2022) (cit. on pp. 21, 25, 26).

[18] Jing Ou, Yingzhen Liu, and Martin Doppelbauer. «Comparison Study of a Surface-Mounted PM Rotor and an Interior PM Rotor Made From Amorphous Metal of High-Speed Motors». In: *IEEE Transactions on Industrial Electronics* 68.10 (2021), pp. 9148–9159. DOI: `10.1109/TIE.2020.3026305` (cit. on p. 21).

[19] Steven Peeters. «Tesla Model S PLAID carbon sleeved rotor is impressive tech». In: (). URL: `https://www.youtube.com/watch?app=desktop&v=iFUAJRDYrrQ` (cit. on p. 23).

[20] L. E. Olsen. *,et al., Permanent magnet motor with wrapping.* International Publication Number WO 2021/225902 A1, Nov. 2021 (cit. on p. 22).

[21] Wuqiang Wang, Yong Li, Dajun Huan, Xiaodong Chen, Hongquan Liu, Yanrui Li, and Lisha Li. «Research on Stress Design and Manufacture of the Fiber-Reinforced Composite Sleeve for the Rotor of High-Speed Permanent Magnet Motor». In: *Energies* 15.7 (2022). ISSN: 1996-1073. DOI: `10.3390/en15072467`. URL: `https://www.mdpi.com/1996-1073/15/7/2467` (cit. on pp. 23, 24).

[22] Josef Binder, Mario Silvagni, Simone Ferrari, Björn Deusinger, Andrea Tonoli, and Gianmario Pellegrino. «High-speed IPM Motors with Rotor Sleeve: Structural Design and Performance Evaluation». In: *2023 IEEE Workshop on Electrical Machines Design, Control and Diagnosis (WEMDCD).* 2023, pp. 1–6. DOI: `10.1109/WEMDCD55819.2023.10110939` (cit. on pp. 25, 27, 28, 41).

[23] Symolic Toolbox Matlab. «Symolic Toolbox Matlab». In: (). URL: `https://www.mathworks.com/products/symbolic.html` (cit. on p. 31).

[24] Vepco. «Performance Analysis of the Tesla Model 3 Electric Motor using MotorXP-PM». In: (). URL: `https://motorxp.com/wp-content/uploads/mxp_analysis_TeslaModel3.pdf` (cit. on p. 58).